ABSTRACT

Title of Document: SURFACE CHARACTERIZATION OF VISCOELASTIC MATERIALS THROUGH SPECTRAL INTERMITTENT CONTACT ATOMIC FORCE MICROSCOPY

Jeffrey Charles Williams,
Master of Science, 2012

Directed By: Assistant Professor Santiago Solares
Department of Mechanical Engineering

The ability to recover material properties at the atomic scale has been the ongoing objective of the Atomic Force Microscope (AFM). More specifically, the most popular operation of the probe with this microscope (Intermittent Contact AFM) has not yet been able to resolve material properties of viscoelastic samples. By using the force and position time signals of the AFM and the constitutive equations for linear viscoelasticity, a method is developed by which such material properties are extracted in real-time scanning. A parametric study is then performed by simulating surface and AFM system conditions to understand the limits under which the method can accurately be performed in experiment. Suggestions are made to help experimentalists optimize the method to cater to the range of viscoelastic materials being measured and the results are related to measured material properties in literature. The method is found to be accurate for a wide range of viscoelastic materials.

SURFACE CHARACTERIZATION OF VISCOELASTIC MATERIALS THROUGH SPECTRAL INTERMITTENT CONTACT ATOMIC FORCE MICROSCOPY

By

Jeffrey Charles Williams

Thesis submitted to the Faculty of the Graduate School of the
University of Maryland, College Park, in partial fulfillment
of the requirements for the degree of
Masters of Science
2012

Advisory Committee:
Professor Santiago Solares, Chair
Professor Amr Baz
Professor Sarah Bergbreiter

Dedication

To my parents,

James and Joanne Williams

Acknowledgements

I would like to extend my gratitude to my friends and family who have enabled me with the opportunity to pursue my goals and provided the encouragement and strength to see them come to fruition. Without them, this thesis would not have been possible.

I would also like to thank my advisor Dr. Santiago Solares at the University of Maryland for mentoring me throughout the last three years. He has consistently provided invaluable advice both academically, professionally, and personally for living a good life. He never lost faith in my academic abilities even when I did. I also wish to especially thank my research group: Gaurav Chawla, Alan Wright, Hussein Ezz Eldin, Daniel Ebeling, and Adam Kareem for the many hours they spent teaching and guiding me during my studies. They have never hesitated to assist me when I struggled and the conversations we shared as coworkers and friends are a keystone to the success of this work. I would like to thank the University of Maryland and all of the faculty and staff, who have provided the resources and teachings necessary for me to develop as a person and an engineer over the past five years.

I would like to thank the National Science Foundation and all those involved in the Louis Stokes Alliances for Minority Participation Bridge to the Doctorate (LSAMP-BD) program at the University of Maryland who have made my studies possible. Finally, I thank my fiancé, Hana Cai, for being my inspiration, motivation, constructive criticism, and source of laughter when the end seemed so far. Words are not enough to express how helpful she has been throughout this entire process.

Table of Contents

List of Tables

List of Figures

Chapter 1: Introduction

1.1 Motivation

It has been over 25 years since the invention of the Atomic Force Microscope (AFM) [1] which drastically altered the field of surface science and the capabilities of sub-continuum imaging. The instrument was originally designed as a contact measurement method by which a micron-sized cantilever would deflect under the reaction force applied by the surface atoms and this deflection could in turn be used to measure the position and stiffness of the sample material being scanned. As the need arose to reduce lateral forces from contact scanning, more complex imaging techniques emerged which operated the cantilever in a dynamic oscillatory mode [2-5]. One imaging technique called Intermittent Contact Atomic Force Microscopy (IC-AFM) (commonly referred to as “Tapping Mode” AFM (TM-AFM) [3]) is an operation technique which typically excites the oscillating cantilever at the fundamental resonance frequency with a fixed excitation amplitude and records either the engaged oscillating amplitude or phase shift as feedback parameters during imaging. The term “Tapping Mode” emerges from the nature of the probe oscillation which is intermittently contacting the surface for a brief portion of the trajectory. For the remainder of this thesis, the term IC-AFM will be used to refer to this operation technique.

IC-AFM has become a widely popular method to measure topographies due to its ease of use, its broad range of applications, and its robustness in the imaging environment (water, ambient air, vacuum, etc.). Moreover, because the tip atoms come in contact with the surface atoms during a portion of the oscillation, it is possible to obtain mechanical properties directly from the contact portion of the interaction between the tip and surface. Through a recent adaptation of the AFM, local elastic stiffness and adhesion of surfaces has been acquired [6, 7] and mapped simultaneously with topography. However, acquiring viscoelastic material properties directly from the surface has been an unresolved issue in the AFM community. Viscoelastic refers to a material which possesses both elastic and viscous flow-like characteristics.

The dissipation phenomenon has also been a major topic of discussion among AFM users since the breakthrough of the instrument. Dissipation refers to the energy lost due to non-conservative mechanisms. More specifically, dissipation discussed in this thesis entails energy lost due to rate-dependent viscous damping resulting from the material construct of the surface. As a first step towards identifying dissipation due to viscoelasticity, Tamayo *et. al.* [8] observed a relationship between the phase shift of the oscillation in IC-AFM and the viscosity of the sample. Two years later, a method of quantification and mapping of the total dissipation signal in IC-AFM using the phase shift was accomplished by Cleveland *et. al.* [9]. However, this method was only able to recover the aggregate dissipation, which is a combination of viscoelasticity and other non-conservative interactions. The separation of these forces into the sub-mechanisms that govern the dissipation phenomenon has been at the forefront of AFM imaging topics. Viscoelasticity of the surface has frequently been used in IC-AFM literature to describe dissipation at the nanoscale [8, 10-18], but the contribution it has towards the aggregate dissipation signal and the ability to extract material properties remains unknown. Additionally, the current methods of quantifying dissipation rely on the phase shift and amplitude of the cantilever alone, which does not allow for surface viscoelasticity to be measured explicitly. The issue of viscoelasticity measurability arises because the phase is governed by three main effects (in addition to others): the amplitude set point ratio, the surface topography, and the material properties [19].

The effects of amplitude set point (the ratio of “tapping” amplitude to free oscillation amplitude) has been explored extensively in research, and can be set such that the motion of the cantilever can be approximated as a simple harmonic oscillator where the perturbations that arise from the tapping motion are small and do not invalidate the approximation [20-22]. The effect of sudden changes in topography is also well studied, and can be neglected under proper experimental procedures where the gains of the controller effecting the piezoelectric base are sensitive enough to adjust to features encountered during scanning [8, 12].

Material properties are one of the driving factors that constitute the force experienced between the oscillating probe tip and the sample surface (called the tip-sample interaction force, denoted as F_{ts}). Without knowing F_{ts} during scanning, the phase and amplitude alone are not sufficient to recover the material properties. Furthermore, several authors [23, 24] have claimed that there is not a clear relationship between phase and viscous dissipation and have cautioned against those who have formulated methodologies [19, 25-29] to recover viscoelastic material properties using the phase shift. Regardless, the identification and recovery of surface viscoelasticity into such measurable material properties (stiffness and viscosity) would help decompose the total non-conservative interaction in IC-AFM.

The goal of this thesis is use a recent probe design (called the Torsional Harmonic Cantilever (THC)) developed Sahin *et. al.* [30] to acquire surface viscoelastic properties using an AFM operating in IC-AFM. The tip-sample interaction force (F_{ts}) is acquired during imaging simultaneously with topography, amplitude, and phase using a spectral process developed by Stark *et. al.* [31]. By acquiring the tip-sample interaction force during real time imaging, it is possible to identify surface properties. In order to achieve the goal of quantitatively acquiring viscoelastic material properties at the nanoscale using IC-AFM, this thesis focuses on defining a method by which these properties can be extracted assuming a linear viscoelastic material. The method presented is a first step towards viscoelastic material property extraction in efforts to the expansion of more complex linear and non-linear viscoelastic materials. Using a mechanical model comprised of elastic springs and viscous dashpots (dampers), the surface of a linear viscoelastic material is simulated to interact with the dynamic THC probe. A method is then developed by which the discrete mechanical properties of the viscoelastic surface are extracted from the simulated AFM signal data. The method will be referred to as the Viscoelasticity Extraction Technique for Intermittent Contact AFM (VETICA) throughout this thesis and will be described at length in Chapter 3. AFM operating conditions such as amplitude set point, resonant frequency, and instrument resolution are used as theoretical user controlled variables to determine the extent of the application of VETICA. Such a method would not only help identify the viscoelasticity of a surface, but what overall contribution viscoelasticity has towards the total dissipation experienced.

1.2 Research Objectives

As previously stated, the objective of this thesis is to provide a procedure to recover viscoelastic material properties through Intermittent Contact Atomic Force Microscopy. In Chapter 2, the necessary background information and theory is provided in order to properly understand the VETICA method and ensuing results of the method. Additionally, a literature review is presented and contextualized with regards to the issues and scope of the studies presented here.

In Chapter 3, the research methods of the thesis are discussed. In order to formulate the method to extract material properties from the surface, a model is chosen and implemented computationally to represent a linear viscoelastic surface as a rheological (i.e. mechanical surface flow) model comprised of mechanical elements (elastic springs and viscous dashpots). Similarly, a specialized AFM probe is modeled in a point-mass mechanical form to facilitate numerical computational simulation. In the final portion of the chapter, the material property extraction method (VETICA) emerges by using the interactions of the tip and sample as seen in F_{ts} and constitutive equations of viscoelastic theory.

After method formulation, Chapter 4 begins by presenting select results to show feasibility and validity of the VETICA method. Method implementation characteristics and constraints are discussed. A range of material properties and AFM system parameters are then selected and simulated. The surface and AFM conditions explored in this research are:

- Surface Properties
  - Viscosity
  - Ratio of Stiffness Elements
- AFM Properties
  - Amplitude Set Point
  - Probe Resonant Frequency
  - Penetration Depth
  - Instrument Resolution

The parametric inputs are used to determine controllable variables which AFM users could use to best optimize the accuracy of the method. Furthermore, these studies identify limits and possible future improvements of the method. In closing, Chapter 4 discusses applicability and comparability of the method to relevant materials and imaging speeds in practice.

Chapter 5 summarizes the results of the thesis and remarks on the intellectual contributions of this work as well as the anticipated benefits. Concluding remarks are made and a future outlook section introduces some ideas and preliminary results on the suggested future direction of the work.

Chapter 2: Background

2.1 The Atomic Force Microscope (AFM)

2.1.1 The Instrument

The Atomic Force Microscope (AFM) (Figure 1) was developed by Binnig, Quate, and Gerber in 1986 and revolutionized surface imaging because it offered the capability of recording topographies with atomic resolution [32] while also providing material information about the surface. The instrument is focused around a small cantilever probe (typically hundreds of micrometers in length), which is terminated with a sharp tip. The effective tip radius can range from a few nanometers to several micrometers, depending on the application, and is fabricated in a variety of geometries. The base of the fixed-free cantilever is usually controlled with piezoelectric actuators.

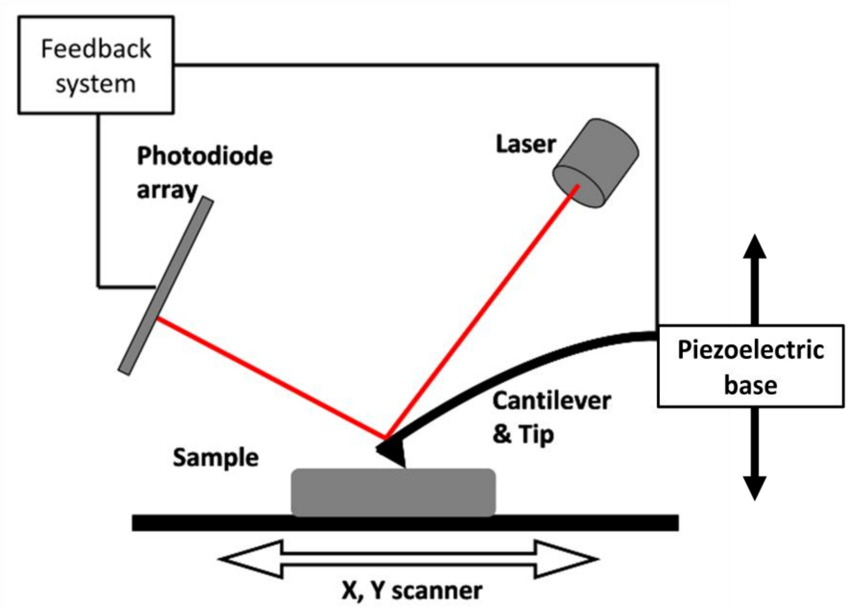

Figure 1. Atomic Force Microscope setup. The distance between cantilever and sample are controlled by a piezoelectric material. The laser is used to measure deflection of the beam by transmitting a voltage from the photodiode to the controller.

In AFM imaging, the instrument uses the tip deflection arising from tip-sample interaction forces between tip atoms on the probe and surface atoms as feedback. A piezoelectric actuator lowers a cantilever probe with a sharp tip attached to the end until it interacts with the atoms on the surface of the sample. The deflection is due to interaction forces between the tip and the sample (F_{ts}) and is acquired by way of a laser beam that is reflected off the end of the cantilever and is then collected on a photodiode array. The position of the reflected laser spot on the photodiode array corresponds to a voltage that is then transmitted to the feedback system, converted to a cantilever deflection through knowledge of the sensitivity of the photodiode array (i.e., V/m), and calculated into a force using a measured nominal stiffness of the cantilever. The position of the laser spot is acquired by a four-quadrant photodiode array capable of measuring flexural motions of the beam (upper and lower halves of the array), as well as torsional rotations of the beam (left and right halves of the array). Utilizing these arrays, Hooke's Law (1) is implemented to find the resulting force:

$$F_{ts} = -kx \tag{1}$$

where k is the nominal stiffness of the beam and x is the measured deflection of the beam from equilibrium. With the AFM, the surface topography can be measured up to a few nanometers in spatial resolution within IC-AFM [33], and others have claimed even higher resolution with other non-contact operating techniques in ultrahigh vacuum [34]. This spatial resolution is far superior to optical microscopes and allows surfaces and material properties to be measured on the atomic scale.

2.1.2 The Tip-Sample Interaction Force (F_{ts})

In dynamic AFM operating modes such as IC-AFM, the tip is constantly either moving toward or away from the surface. Figure 2 displays the configuration of a tip interacting with a surface in dynamic AFM and shows the veritcal distance between key elements of the system [20].

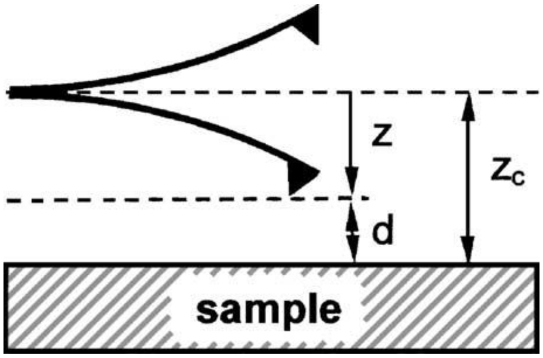

Figure 2. Interaction of cantilever probe and surface during dynamic AFM. *Z* is the amplitude of the oscillating tip. Z_c is the distance between the piezoelectric base of the cantilever and the surface (i.e., the equilibrium position of the tip). *d* is the resulting tip to sample distance. Figure from reference [20].

In IC-AFM, because the tip is coming into contact with the surface, the interaction force between tip and sample fluctuates between two regimes, known as the non-contact and contact regime. The non-contact regime is defined as the period when the overall tip-sample interaction force gradient is negative (i.e., no imparted repulsive forces). The beam operates in non-contact until, as the name implies, contact is made between the tip and sample and repulsive forces are experienced. Figure 3 shows the force-distance curve which results from tip to sample interactions and is used to evaluate the dynamics of the force in IC-AFM through the two interaction regimes. The vertical spatial transition point between these two regimes is denoted as a_0.

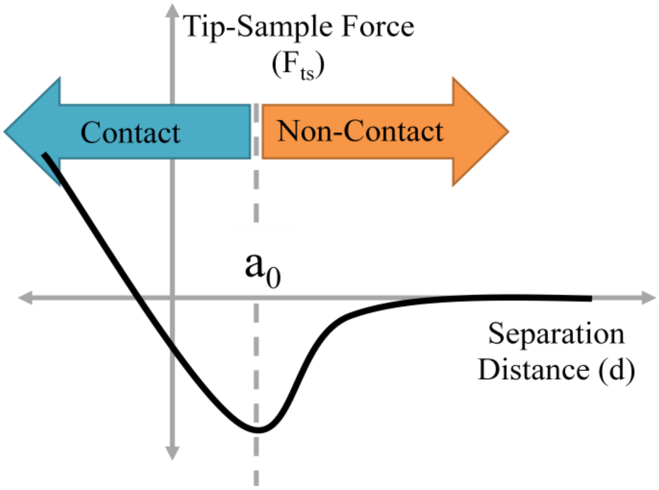

Figure 3. The force versus distance curve that emerges from tip-sample interaction. The orange and blue arrows indicate the non-contact and contact regimes respectively, and a_0 is the distance the transition occurs between contact and non-contact.

The interaction force between atoms on the tip and atoms on the surface contains both long-range attraction and short-range repulsion forces. Short-range forces are usually expressed in the form of contact mechanics equations stemming from Hertzian contact theory. Long-range forces occur over large separation distances of several nanometers and depend on the experimental environment. For example, in ambient air, adhesion forces can be present due to a meniscus of water formed between the tip and surface [35]. Additionally, large influences from long-range forces can result from electrostatic and van der Waals forces that can be modeled as seen in equations (2) and (3) respectively:

$$F_{electrostatic} = -\frac{\pi \epsilon_0 R_{tip} U^2}{d} \qquad (2)$$

where ϵ_0 is the permittivity of free space, R_{tip} is the approximated spherical tip radius, U is the electrical potential difference, and d is the distance between the tip and the sample, and

$$F_{VdW} = -\frac{A_H R_{tip}}{6d^2} \tag{3}$$

where A_H is the Hamaker constant determined by chemical constitution of the interacting bodies, R_{tip} is the spherical tip radius approximation, and *d* is the distance between the tip and the sample. For the scope of this thesis, electrostatic forces are not considered and adhesion forces will be ignored. This simplification is made in order to isolate the effects of viscoelasticity and focus only on the hysteresis created from internal material mechanisms of the surface.

To model short- and long-range forces, many scientists have used the foundations laid by contact mechanics stemming from Hertzian contact. The two most common analytical expressions to represent the interaction force are the Derjaguin-Muller-Toporov (DMT) [36] and Johnson-Kendall-Roberts (JKR) [37] models. The JKR model is useful for describing materials with lower stiffness, high adhesion forces, and large cantilever tip radii [20]. The DMT model is useful for relatively stiffer materials with smaller tip radii and lower adhesion forces and better suited for the materials of interest in this study [20]. Extensive studies on contact mechanic methods and their applications to materials measured with the AFM have been reported and while these models will not be discussed in detail in this thesis, the work of Unertl and Attard *et. al.* should be referred to for additional information [38, 39]. The DMT model is more applicable to the context of this work, and follows the form of equations (4) and (5) respectively:

$$F_{DMT} = \frac{4E^*\sqrt{R_{tip}}}{3}(a_0 - d)^{3/2} \quad \text{for} \quad d \le a_0 \tag{4}$$

And with:
$$\frac{1}{E^*} = \frac{1-{\nu^2}_{tip}}{E_{tip}} + \frac{1-{\nu^2}_{sample}}{E_{sample}} \tag{5}$$

where E* is the effective elastic modulus, R_{tip} is the spherical tip radius approximation, ν is the Poisson's ratio of the material, a_0 is the vertical position at which the forces transition from attractive to repulsive, and d is the distance between the tip and the sample. The total tip-sample interaction force is formulated by summing the short-range DMT repulsive forces and the long-range van der Waals forces into the following formula for F_{ts} (note that the transition from non-contact to contact occurs at a_0):

$$F_{ts} = \frac{4E^*\sqrt{R_{tip}}}{3}(a_0 - d)^{3/2} - \frac{A_H R_{tip}}{6{a_0}^2} \quad \text{for} \quad d \leq a_0 \tag{6}$$

$$F_{ts} = -\frac{A_H R_{tip}}{6d^2} \quad \text{for} \quad d \geq a_0 \tag{7}$$

2.1.3 AFM Methods for Surface Characterization

One of the major advantages of the AFM is the identification and characterization of material composition and its properties. In response to the demand for nanoscale material characterization, several operating techniques were implemented with the instrument to facilitate acquiring information from the sample. Within the widely-used dynamic operation [2] of the cantilever, amplitude modulation [3] and frequency modulation [5] are popular methods because of several benefits such as less sample damage and no "jump-to-contact" associated with dynamically oscillating in the cantilever [20]. Although these methods provide means to extract quantitative information on the total dissipated signal based on the phase of the oscillating cantilever [9, 40], the origins and breakdown of the total dissipated energy has been a topic of interest to the AFM community. Among the factors that contribute the total dissipated energy, the effects of hysteresis caused from surface viscoelasticity remains unanswered. In order to address viscoelasticity several contact mode models have been introduced to extract surface stiffness.

Traditional constant contact static modes such as contact mode (CM-AFM), friction force (FFM) [41, 42] and force modulation (FM-AFM) [43] are commonly implemented to measure the changing surface stiffness as the tip is constantly in contact with the surface and raster scanned. A method recently developed by Sahin *et. al*. [30] uses a specially designed Torsional Harmonic Cantilever (THC) probe operating in IC-AFM to get real time force versus distance curves. The method obtains these results by using a “T-shaped” probe with an off-center tip on a short paddle at the end of a rectangular cantilever to excite a torsional signal from the tip in addition to the flexural signal from the cantilever. This design enables for acquisition of real time force curves during scanning and high spatial resolution mapping of material stiffness (Young’s modulus). The probe implementation method is now commercially available through HarmoniX™ (Bruker AXS, Santa Barbara, CA, USA). Similarly, using the pulsed force mode of AFM [44], a method was recently developed, commercialized, and experimentally verified [6, 7] (Bruker AXS, Santa Barbara, CA, USA) in PeakForce™ Quantitative Nanomechanical Mapping (QNM™) to distinguish adhesion and stiffness from a sample with dissipation with an improved scan speed and force resolution than that of the traditional pulsed force mode. Results of the QNM technique can be seen in Figure 4. Although these methods greatly improve the quantification of sample stiffness in real time, they do not provide information on samples where the surface stiffness varies as a function of time, namely for viscoelastic materials.

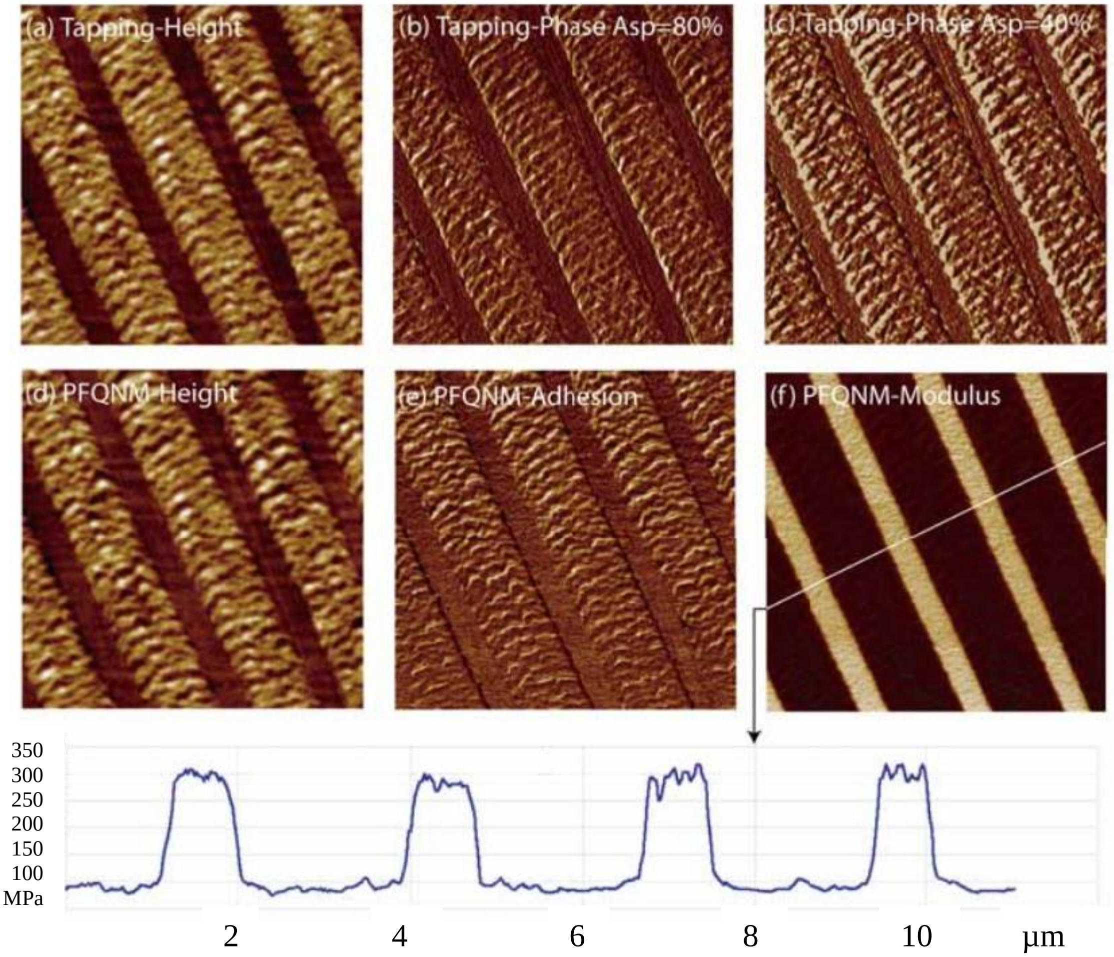

Figure 4. Comparison of Tapping Mode Phase Imaging (a-c) and the Peak Force QNM method (d-f) for a multilayer optical film. (b) and (c) were captured at different amplitude set points (40 and 80% of the free oscillation respectively). (e) shows the adhesion from the sample which resembles the phase images (b-c). (f) is the extracted modulus and a section cut is plotted along the blue line to show the numerical values seen in the contrast. Figure from reference [45].

Recent work by Yuya *et. al.* using atomic force acoustic microscopy (AFAM) [46, 47] lead to the exploration of extracting viscoelastic material property at the nanoscale by using the contact-resonance atomic force microscopy for viscoelasticity (CRAVE) technique [48]. In this technique, the cantilever is deflected on the surface and contact is maintained as AFAM is performed while displacement amplitude and phase shift of the cantilever are measured. Using this technique, the authors have modeled the surface as a two-element linear rheology model with discrete mechanical components (i.e., elastic springs and viscous dashpots) and use Euler-Bernoulli beam theory for the cantilever to find viscoelastic mechanical properties through the frequency response by relating the complex wavenumbers of the characteristic equation to the discrete elements of the surface model [49]. Yuya *et. al.* use the Voigt rheological model configuration (Figure 5) in which a spring is placed in parallel with a dashpot.

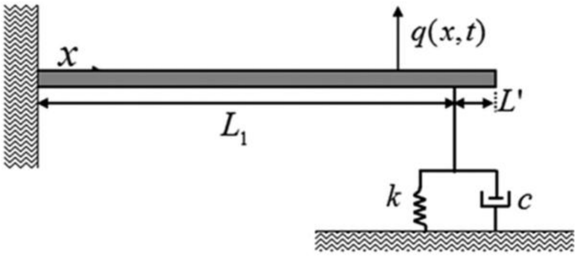

Figure 5. Mechanical model of an AFM cantilever in contact with a viscoelastic surface using the Voigt configuration of spring and dashpot to represent the surface. Figure from reference [50].

The Voigt model is known to give a good representation of the creep compliance of a material, but does not hold for stress relaxation [51]. Due to the inherent nature of the intermittent contact operating mode, a solution is needed which can both recover stress relaxation during the contact period of the oscillation, and also accurately recover the creep compliance of the surface when the cantilever is no longer in contact. Therefore, this thesis proposes a new method where the simulation of the IC-AFM utilizes a mechanical model that can accurately reconstruct creep compliance and stress relaxation responses, in order to recover linear viscoelastic material properties.

2.2 Modes Of Operation

2.2.1 Contact

The original design of the AFM operates in what is known as "contact mode" AFM, where a static tip deflection is used as the feedback control to measure surface topographies. While the deflection is recorded, the tip is raster scanned over the surface and the base is adjusted to compensate for variations in surface features. The interaction force, F_{ts}, is captured in this mode through the use of Hooke's Law. The two major drawbacks of this operating technique are surface damage and a phenomenon known as "jump to contact."

While operating in contact mode, high shear forces due to large changes in feature size can cause the tip to scratch along the surface and damage the surface and tip [52]. In addition to damage, the CM-AFM method can create surface artifacts as a result of stick-slipping of the tip over steep surface changes. Therefore, the CM-AFM mode has a particularly intense degradation of softer materials, such as viscoelastic polymers.

The "jump-to-contact" phenomenon arises in CM-AFM as the tip approaches the surface. The long-range van der Waals forces increase in magnitude with the square of the separation distance as seen in equation (2). As the tip approaches the surface, the attraction force between tip and sample becomes greater than the natural restoring spring force of the cantilever, causing the tip to "jump" to the surface. The jump results in a loss of spatial information and does not capture critical information around the regime transition point a_0. It will be shown in Chapter 3 that the loss of information around the regime transition point leads to difficulty when extracting viscoelastic material properties. Due to the aforementioned drawbacks of the constant contact imaging technique, the CM-AFM mode of operation is not suited for the operating technique investigated in this thesis and is not used in simulation.

2.2.2 Non-Contact

Non-Contact AFM (NC-AFM) is the most popular method for achieving atomic resolution because of the high spatial resolution achieved and the minimal surface damage inflicted as a result of the method. In the operation of the NC-AFM operating technique, the tip oscillates in a dynamic mode and the lowest point on its trajectory approaches near the surface, but never makes contact with the surface. The method typically uses a shift in resonant frequency of the cantilever to measure the topography. Although the NC-AFM method is effective at achieving high-resolution maps of topography, it also possesses some negative drawbacks. First, the operation technique is highly sensitive to temperature, moisture, and other environmental factors. Therefore, it is frequently implemented in a low temperature vacuum. Additionally, because the tip does not make contact with the sample during the oscillation, NC-AFM is not conducive to identifying material properties such as viscoelasticity, which can only be distinguished by entering the contact regime.

2.2.3 Intermittent Contact

Intermittent Contact AFM (IC-AFM) is the method of operation when the tip oscillates in a dynamic mode similar to NC-AFM but is lowered to a point where the bottom portion of the trajectory lightly “taps” on the surface. This “tap” creates a repulsive force for a brief period of time, and can be used to extract material properties such as stiffness, and viscoelasticity. In order to gain comparative information between the free response and the interaction region with the surface, the oscillation amplitudes (e.g., hundreds of nm) in IC-AFM are much larger than the interaction regime (less than ten nm). Within IC-AFM, Frequency Modulation (FM) and Amplitude Modulation (AM) are two primary control methods to utilize the dynamics of the oscillation to capture surface topography.

Frequency Modulation is a control logic where the cantilever is driven at resonance in “self-excitation” where the beam response frequency is appropriately phase shifted, scaled, and used as the excitation signal [53, 54]. This operating technique can be achieved as a result of a characteristic of the simple harmonic oscillator: an oscillation can be driven at resonance when the excitation signal provided is 90 degrees phase shifted from the output. Figure 6A shows the effect of interaction regimes and system damping on the observed variables used to control the AFM in FM. In FM, as the base position of the cantilever is changed and the tip trajectory nears the surface, the shift in the effective resonant frequency of the system is used as the feedback to maintain constant tip-sample distance. A phase-locked loop (PLL) or a self-excitation loop can be used to maintain an excitation signal that is at the current resonant frequency and the shift between actual resonant frequency and the frequency of the free oscillating cantilever is measured. Figure 6B displays the effect that system damping has on the phase shift observed by the oscillating cantilever. The steepness of the phase near resonance decreases as the quality factor (Q) decreases and higher damping is present.

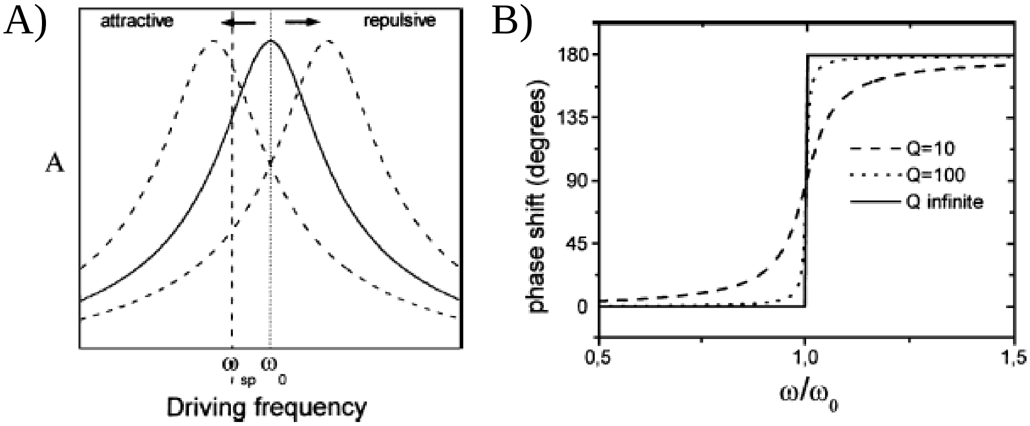

Figure 6. A) Amplitude plot of a harmonic oscillator at natural resonant frequency (solid line), and resulting shift when attractive and repulsive forces interact with the oscillation (dashed). B) Phase plot showing the effects of diminishing quality factor (Q) resulting from increased damping of the system. Figure from reference [20].

An advantage to using FM as the control mechanism is the quick settling time. The settling time in FM is $1/\omega_0$ and is not affected by a change in the damping (quality factor) of the system. This advantage makes FM particularly attractive for use in vacuum where quality factors can reach as high as 50,000 (note that quality factor is dimensionless). Consequently, the FM technique stability suffers when larger perturbations are introduced in the simple harmonic oscillation. Although the quality factor decreases in ambient air, these perturbations can still occur in IC-AFM when the tip-sample interaction during contact alters the sinusoidal trajectory. Another drawback is the complexity of the control logic, which requires measurement of the phase shift, excitation frequency, cantilever amplitude, and in the case of constant amplitude (CA), the excitation amplitude [53]. While the FM control logic is useful for operating in vacuum, the operating environment of interest is within ambient air (much lower quality factor) and a simpler and more stable control logic called Amplitude Modulation is presented below.

Amplitude Modulation (AM) is a control logic where unlike FM, the oscillating cantilever uses only the engaged amplitude of the oscillation as feedback. The amplitude is set at a fixed “set point ratio,” which is the ratio of the engaged amplitude with the surface to the free oscillation amplitude of the cantilever far from the influences of surface forces. The engaged amplitude differs from the free amplitude due to fluctuations in resonant frequency of the cantilever when forces interact with the tip. As a consequence of different cantilever resonant frequency, amplitudes decrease when the beam is not excited at resonance and this decrease in amplitude is measured as the engaged amplitude. AM-AFM is the most popular method to operate the cantilever in IC-AFM [20] because of its robustness and ease of implementation in many AFM applications. The simulated AFM system used in this thesis operates in AM IC-AFM because of the aforementioned benefits, simplicity, and the reasons discussed in the following section.

2.3 The Force Reconstruction

The quantitative acquisition of F_{ts} in dynamic AFM has been a heavily researched topic which continuously evolves as new imaging techniques are developed. As previously stated for the static contact case, F_{ts} for contact is approximated by the Hookean spring law because the tip and surface remain in contact. However, in dynamic AFM (including IC-AFM) the interaction force is not as easily quantitatively expressed and must be derived based on the physical relationships of the particular control logic implemented. The application of the control logics Amplitude and Frequency Modulation (AM and FM, respectively) are discussed to detail the progress made towards recovering F_{ts} using these two imaging modes and concludes by selecting a force reconstruction method suited for the needs of the VETICA method.

The work for recovering F_{ts} in FM-AFM was pioneered by the work of Albrecht *et. al.* [5], Giessibl [55], and Durig [56, 57] where the force can be reconstructed for the tip-sample interaction in the limiting cases of either very small or very large oscillation amplitudes with regards to the range of interested interactions. Implementing these methods, the work by Hölscher *et. al.* [58] and Albers *et. al.* [59] implements volumetric scanning where the force is acquired in three directions (planar surface x-y and the vertical distance z). Recent work by Sader and Jarvis [60-63] develop a force reconstruction technique in FM-AFM for arbitrary amplitudes where the relationship between frequency shift and force is inverted in the Laplace domain and substituted with fractional derivatives to recover the force. The Sader method, like those previously developed, is capable of acquiring the force in three directions during scanning. In experiment, the forces are acquired in three dimensions by raster scanning many planes at fixed heights above the surface and using the recorded frequency shift (and appropriate method) to convert it to a force. These planes of force data are then superimposed to obtain a volumetric force in three dimensions. In all cases of the aforementioned force curve acquisition methods in FM-AFM, the scan times become quite long (e.g., it may take hours or days to process one image because of the very high Quality Factors) and image drift correction schemes must be implemented that may lose image information [59]. For this reason, we look at the methods provided for Amplitude Modulation.

Previously, the Amplitude Modulation (AM-AFM) force reconstruction was derived by O'Shea *et. al.* [64] for small amplitudes and later expanded for the inclusion of larger amplitudes by Hölscher *et. al.* [65]. For arbitrary oscillation amplitudes, Lee and Jhe [66] obtained results (however not in closed form) and Hu and Raman [67] developed a method using Chebyshev polynomials, and although effective, requires as many as 40 terms to apporoximate the force and no mention of inclusion of non-conservative forces is given. Katan *et. al.* [68] derived a model based on the Sader method for amplitude modulation, however the experimental validation did not extensively investigate the ability to recover non-conservative forces and the effectiveness in IC-AFM were not explored. Another method for AM-AFM exists called the Spectral Inversion Method from Stark *et. al.* [31, 69] where the use of the higher harmonics resulting from excitations of the tip-sample contact in IC-AFM were used to calculate a direct interaction force from the position data in the frequency domain using the transfer function of a simple damped harmonic oscillator. The major benefit of the Spectral Inversion Method is it does not rely on *a priori* knowledge of the system and can acquire the F_{ts} in three dimensions much faster than the other presented methods. Therefore, the Spectral Inversion Method will be the choice of method for force reconstruction used in this thesis.

The Spectral Inversion Method is intended to take a temporal dynamic AFM signal and invert it in the frequency spectrum to resolve a force signal back in the time domain. This method has the capability of acquiring a force signal in real-time scanning, which previous force extraction techniques could not achieve. Additionally, the Spectral Inversion Method is quicker than previous methods and allows for rapid scans of surface topographies and accompanying force curves. The implications of acquiring a real-time force could open the possibility of real-time acquisition and mapping of material properties at the nanoscale.

The Spectral Inversion Method, like dynamic AFM, works under the assumption that the motion of the cantilever can be approximated as a simple harmonic oscillator with viscous damping from the environment. Using F_{ts} as the feedback parameter, the tapping oscillation can be represented as a linear mechanical system in state space with two driving external forces: one from the driving piezoelectric base (F_{drive}), and one from F_{ts} [69]. F_{drive} follows the sinusoidal form of $A\cos(\omega t - \varphi)$, where A is the amplitude, φ is the phase lag between the input and recorded signal, and ω is the drive frequency, usually set to the fundamental resonant frequency of the cantilever. Being a linear system, equation (8) can be related to the input displacement to output total force through a known transfer function (G).

$$F_{in} = Z_{out}/G \tag{8}$$

where $F_{in} = F_{ts} + F_{drive}$, Z_{out} is the position of the tip, and G is the transfer function for the simple damped harmonic oscillator. Recent developments in probe design allows the two contributing forces in F_{in} to be decoupled allowing for direct calculation of F_{ts}.

2.4 AFM Cantilever Dynamics

2.4.1 Standard Rectangular Cantilever

A complete description of the dynamics of the AFM cantilever probe is essential to understanding both the experimental and simulated modeling systems of dynamic

AFM imaging techniques. The following overview of the dynamics is presented as the theory applies to a rectangular cantilever oscillating in the fixed-free setup (as seen in Figure 7), and more details can be found in references [35, 67, 70-72].

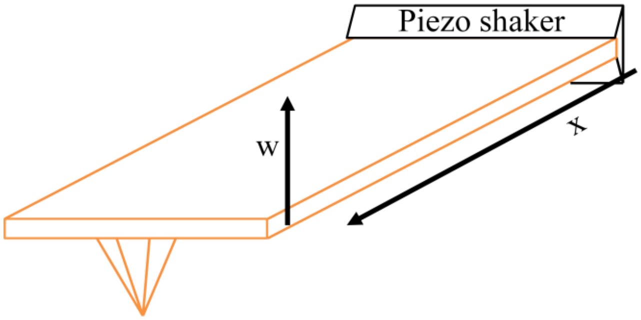

Figure 7. Standard rectangular cantilever fixed-free setup with the fixed end attached to the piezo shaker where *w* is the displacement of the beam, *x* is the position along the beam along the axial direction.

Euler-Bernoulli beam theory allows the rectangular beam to have the following governing equation of motion along the longitudinal axis of the beam:

$$F(x,t) = EI\frac{\partial^4 w(x,t)}{\partial x^4} + \mu\frac{\partial^2 w(x,t)}{\partial t^2} + c\frac{\partial w(x,t)}{\partial t} \qquad (9)$$

where w is the displacement of the beam, x is the position along the beam along the axial direction, t is the time, E is the Young's modulus, I is the second moment of inertia, μ is a mass per unit length, c is a viscous damping coefficient, and F is the external applied load on the beam and contains both F_{ts} and F_{drive}. In IC-AFM, the tip-sample force has a non-linear form and can make the partial differential equation in the beam equation difficult to analytically compute. However, for most applications of dynamic AFM, only the first eigenmode is considered to be excited, and the effects of higher eigenmodes are considered to be negligible under careful selection of experimental conditions. As a result, the beam theory equation for the cantilever is often approximated using a point-mass model where the oscillatory behavior is still accurately captured.

The point-mass equation of motion for the AFM standard cantilever beam in the general form, is as follows:

$$m\ddot{z} + c\dot{z} + kz = F(t) \tag{10}$$

where m is the mass, c is the viscous damping coefficient, k is the nominal stiffness of the cantilever, z is the position of the tip (the over dots refer to differentiation with respect to time), and *F(t)* is the sum of externally applied loads on the beam. This system is a simple harmonic oscillator with damping and is for only the first eigenmode of the cantilever. The nominal stiffness of the beam depends on the geometry, boundary conditions, and material properties of the beam, and for the single rectangular cantilever is:

$$k = \frac{3EI}{L^3} \tag{11}$$

where E is the Young's modulus, I is the second moment of inertia, and L is the length of the beam. The viscous damping coefficient c is related to characteristics of the vibrating system, and if given by:

$$c = \frac{m\omega_n}{Q} \tag{12}$$

where m is the mass, ω_n is the resonant frequency of the beam, and Q is the quality factor. For the purposes of this work, the point mass model has been studied extensively and found to be a good approximation to describe and model the cantilever probe and surface interactions in IC-AFM because the excitation of the higher flexural eigenmodes is expected to exhibit Fourier components that are roughly three orders of magnitude lower than the response of the fundamental eigenmode [73]. Although the point mass model gives a reasonable model to use for computation simulations, the issue of decoupling the external applied load F(t) is not accomplished with the current design. The next section will introduce a recently designed probe that can separate the cumulative interaction force, enhance the higher harmonics of the interaction to facilitate the real time force extraction method resulting from the Spectral Inversion Method.

2.4.2 Dual Oscillator – Torsional Harmonic Cantilever (THC)

With the development of the Spectral Inversion Method, a new probe design emerged that could capture and enhance the higher harmonics of the tip-sample interaction that could also use a part of the probe as a sensor to measure and decouple the tip-sample interaction force and the driving force from the piezo shaker. The Torsional Harmonic Cantilever (THC) probe [30, 74] (Figure 8) is a specialized cantilever with a short (~50µm) paddle attached to the end of a longer (~300µm) flexural rectangular cantilever forming a "T-shape." The tip is then offset from the axis along the length of the beam on a paddle by several microns (~15µm) and while the piezoelectric actuator at the fixed base excites the flexural oscillations of the beam, only the tip-sample interaction forces excite the torsional oscillations of the paddle. This concept is under the assumption that the paddle is perfectly balance and no torsional vibrations are induced as a result of flexural motions. The response of the THC is captured using the four-quadrant photodiode (Figure 9), as like other methods in AFM. The motion of the torsional oscillations are detected on the four-quadrant photodiode array by subtracting the intensities measured on its left and right half, and should not be influenced by the flexural motions of the cantilever caused by laser spot movement on the photodiode vertically. Because the paddle has a shorter moment arm than the cantilever, it yields higher deflection bending angles under the influence of the tip-sample force and therefore torsional oscillations are detected with more sensitivity. Additionally, careful consideration must be made when selecting the torsional stiffness of the beam, because too high a stiffness would yield low bending angles. The benefit of this increased sensitivity to the photo detector is that large paddle amplitudes are not required to measure deflection precisely.

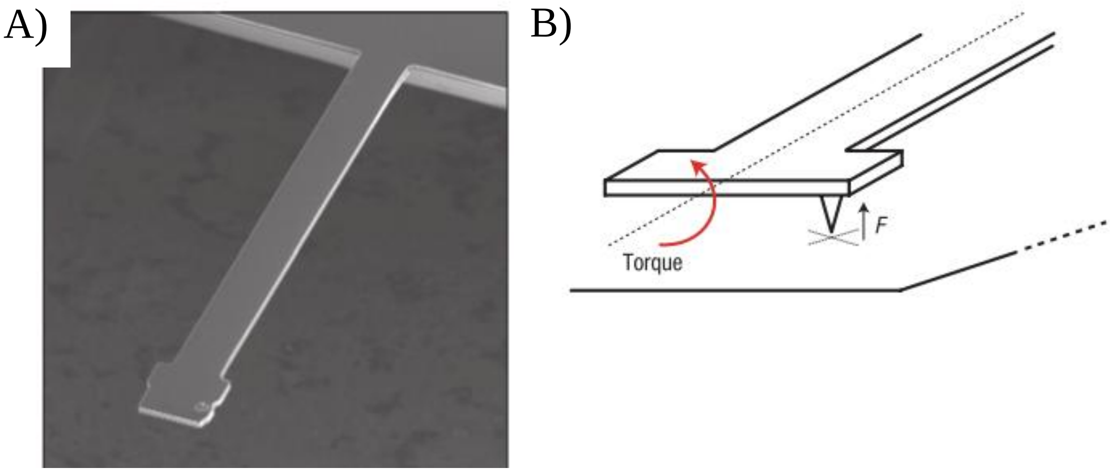

Figure 8. (A) A scanning electron micrograph of the Torsional Harmonic Cantilever (THC). (B) The THC design with offset tip. Torque is generated on the paddle due to moment created about the neutral axis along the flexural cantilever. Figure from reference [30].

The THC's main attribute is that the torsional oscillations of the paddle are at a much higher frequency than that of the flexural oscillation of the cantilever. This feature is expected because beam theory predicts that torsional modes of a rectangular beam are typically located at higher frequencies. The offset tip enhances the amplitudes of these higher torsional frequencies, and in turn, enhances the amplitudes of the higher harmonics of the flexural seen in Figure 10. Therefore, if the THC can capture amplitudes of higher harmonics, then resulting forces acquired via the Spectral Inversion Method are more accurate.

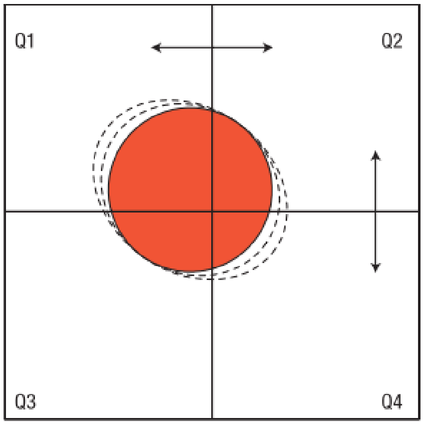

Figure 9. The laser spot on photodiode for the Torsional Harmonic Cantilever. The horizontal movements (Q1 to Q2 and Q3 to Q4) result from torsional excitations by the surface on the paddle and vertical movements (Q1 to Q3 and Q2 to Q4 result from flexural motions of the cantilever excited by the piezoelectric shaker base. Figure is from reference [30].

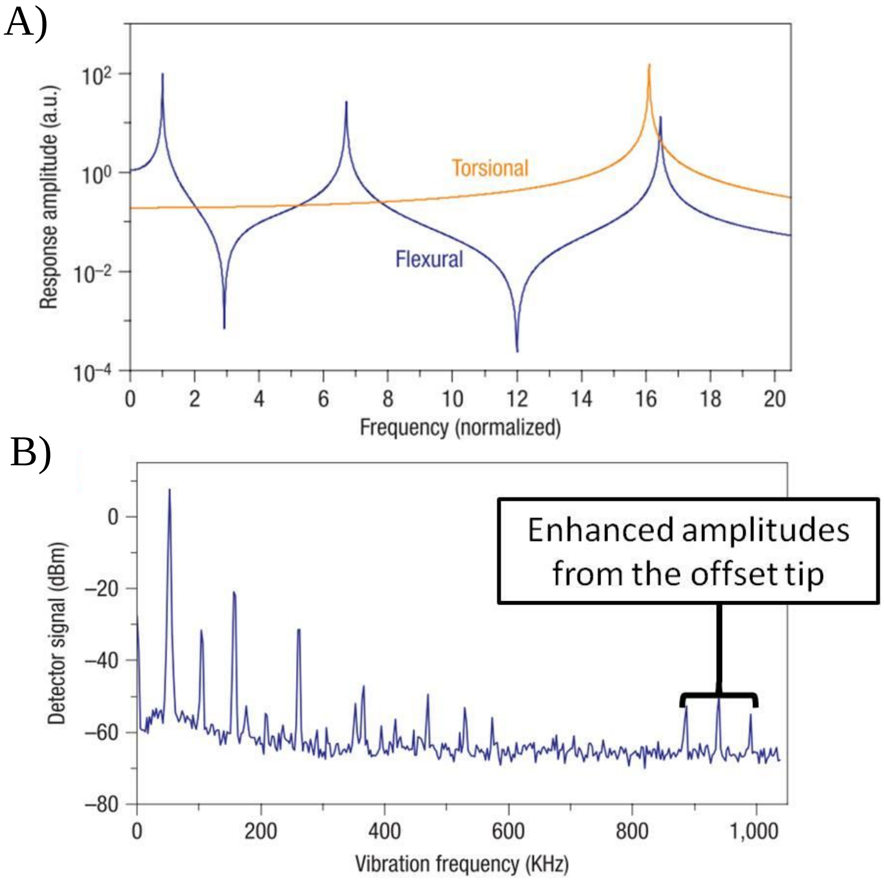

Figure 10. A) Response Amplitudes of the flexural and torsional modes of the THC probe. B) Signal amplitudes recorded for the flexural motion. The higher amplitudes peaks marks are from the torsional oscillation enhanced by the offset tip design. Figure is from reference [30].

Solares and Hölscher [75, 76] performed numerical studies where systems of the THC were modeled and analyzed for liquid, air, and vacuum environments. The first mechanical system developed to study the features of the THC was modeled as a coupled dual oscillator and named the Linear Dual-Spring-Mass (LDSM) model [75, 77] and is illustrated in Figure 11a. Although this model is able to reproduce certain features of the THC interaction, the inherent coupling of the masses does not accurately represent the THC, which is closer to that of a decoupled perfectly balanced dual oscillator.

In response, Solares *et. al.* introduced the Torsional Harmonic Cantilever (THC) representation of the probe (Figure 11b), where the mass of the paddle and tip no longer influenced the cantilever vibrations. Although the cross-talk between the two oscillators is certainly thought to exist [30], it is likely that the system behaves closer to the THC representation and will continue to approach the ideal “no contamination” scenario as improvements to probe manufacturing capabilities become available.

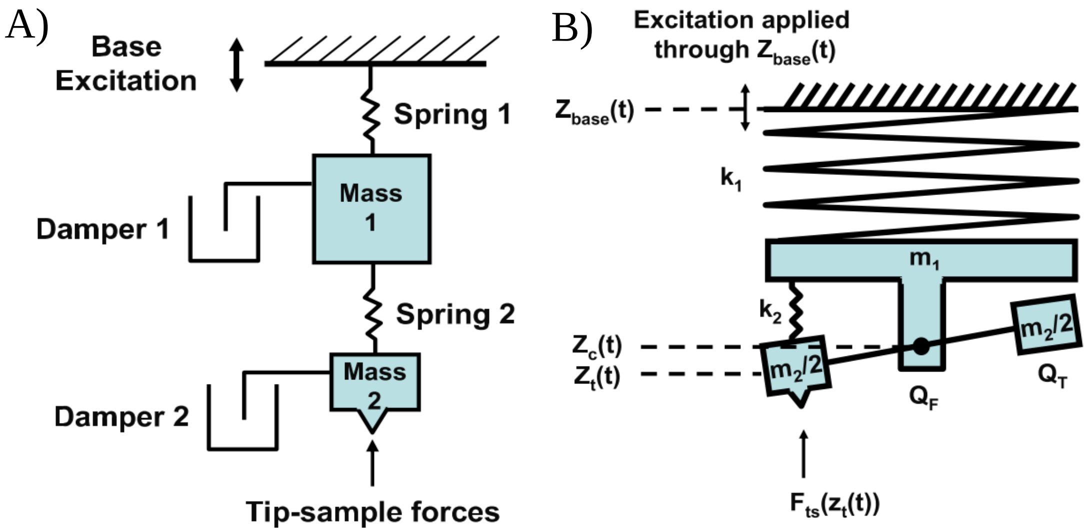

Figure 11. A) Linear Dual-Spring-Mass (LDSM) mechanical representation. *Mass 1* and *Mass 2* are the flexural cantilever and torsional paddle and tip, respectively. B) The Torsional Harmonic Cantilever (THC) mechanical system. m_1 and m_2 are the flexural cantilever and torsional paddle and tip, respectively. Z_{base}, Z_c, and Z_t are the vertical positions of the piezo base, flexural cantilever, and paddle/tip, respectively. k_1 and k_2 are the nominal stiffness of the cantilever and paddle, and Q_F and Q_T are the quality factors associated with the cantilever and tip. The inertial forces in *Mass 2* of the LDSM are transferred into the *Mass 1* through coupled motion, whereas the motion of m_2 is decoupled from that of m_1 in the THC model. Figure is taken from reference [75].

In order to model the THC probe in computational simulation, the following equations of motion are formed for the decoupled dual oscillator (THC) mechanical model:

Flexural:
$$(m_1+m_2)\frac{d^2z_c(t)}{dt^2} = -k_1[z_c(t)-z_{base}(t)] \\ -(m_1+m_2)\frac{2\pi\nu_1}{Q_F}\frac{dz_c(t)}{dt} + F_{ts}[z_t(t)] + F_{drive} \tag{13}$$

Torsional:
$$m_2\frac{d^2z_c(t)}{dt^2} = -k_2[z_t(t)-z_c(t)] - m_2\frac{2\pi\nu_2}{Q_T}\frac{d[z_t(t)-z_c(t)]}{dt} \\ + F_{ts}[z_t(t)] \tag{14}$$

where m_1 and m_2 are the masses of the flexural cantilever and torsional paddle and tip, respectively. z_{base}, z_c, and z_t are the vertical positions of the piezo base, free end of the flexural cantilever, and tip position on the paddle, respectively in time t. ν_1 and ν_2 are the fundamental natural frequencies of the cantilever and tip, k_1 and k_2 are the nominal stiffness of the cantilever and paddle, and Q_F and Q_T are the quality factors associated with the flexural cantilever and torsional paddle. $F_{ts}[z_t(t)]$ is the tip-sample interaction force which couples the two equations through force and acts as the driving force for the paddle/tip excitations. z_{base} is determined by F_{drive}, which is the sinusoidal driving force of the form $A_d cos(\omega t - \varphi)$ for the cantilever where A_d is the driving amplitude, φ is the phase lag, and ω is the drive frequency, usually set to fundamental resonant frequency of the cantilever.

The introduction of a constraint equation, $z_p = z_t - z_c$, reduces the reference frames in the equations of motion by one and removes the influence of z_c on the vibrations in z_t. The resulting equation of motion after introducing the constraint equation is as follows:

Flexural:

$$\begin{aligned}(m_1 + m_2)\frac{d^2 z_c(t)}{dt^2} &= -k_1[z_c(t) - z_{base}(t)] \\ &-(m_1 + m_2)\frac{2\pi\nu_1}{Q_F}\frac{dz_c(t)}{dt} + F_{ts}\left[z_p(t) + z_c(t)\right] + F_{drive}\end{aligned} \tag{15}$$

Torsional:

$$\begin{aligned}m_2\frac{d^2 z_c(t)}{dt^2} &= -k_2\left[z_p(t)\right] - m_2\frac{2\pi\nu_2}{Q_T}\frac{dz_p(t)}{dt} \\ &+ F_{ts}\left[z_p(t) + z_c(t)\right]\end{aligned} \tag{16}$$

Utilizing the decoupled vibrations from the reformed equations of motion between the tip and cantilever, the paddle/tip ensemble can be used as a sensor to determine F_{ts} via the Spectral Inversion Method. In order to form the necessary transfer function, an ideal damped harmonic oscillator has the transfer function of the form:

$$T(\omega) = \frac{\omega_2^2/k_2}{\omega_2^2 - \omega^2 + i\omega\omega_2/Q_T} \tag{17}$$

where ω_2, k_2, and Q_T are the natural frequency, nominal spring stiffness, and quality factor of the torsional paddle, respectively. ω is the frequency variable which produces the value for the transfer function $T(\omega)$. If Spectral Inversion Method is applied, the Fourier Transform of the position of the tip can be taken as an "input" in the frequency domain, and use the transfer function to obtain the tip-sample interaction force as the "output" in the frequency domain as follows:

$$T(\omega) = \frac{Output}{Input} \tag{18}$$

$$T(\omega) = \frac{F_{ts}(\omega)}{z_t(\omega)} \tag{19}$$

$$F_{ts}(\omega) = T(\omega)\left(z_p(\omega) + z_c(\omega)\right) \tag{20}$$

Equation (20) gives the equation for the tip-sample interaction force using the paddle equation of motion for the THC mechanical model from (16) and the Spectral Inversion Method from equation (8). In order to use the transfer function, Fourier transforms of $F_{ts}(\omega) = \mathcal{F}\{F_{ts}(t)\}$ and $z_p(\omega) + z_c(\omega) = \mathcal{F}\{z_p(t) + z_c(t)\}$ are used to take the time signals and transform them into the frequency spectrum.

As previously stated, the THC has been commercialized and has successfully measured elastic stiffness of several materials of interest including DNA/RNA [78], and proves to be promising for characterization of a range of soft materials from biological to polymer. Although there are limitations on how many higher harmonics the tip can currently attain to accurately reconstruct the force signal [76] using the spectrum technique, the possibility of acquiring the force in real time leads the way to a method for characterizing viscoelastic surfaces.

2.5 Viscoelasticity

2.5.1 Theory

Viscoelasticity is a long-studied branch of material science that revolutionized the world of polymer physics. A large set of fabricated materials are considered viscoelastic, and play a large role in the development of polymer, biological, and biomimic (replicates biology) technologies. Additionally, most biological tissue and single cell organisms are viscoelastic, and advancements in the material sciences of those areas could yield profound impacts in the medical field.

In engineering, viscoelasticity is most commonly related to the intensive properties of the material like modulus, stress, and strain. Intensive properties are scale invariant properties which do not depend on the size of the system or geometrical boundary conditions. Although, viscoelasticity is found almost always to be a non-linear process in nature, the use of a theoretical linear representation offers a good starting point to understanding the effects of viscoelastic materials [79, 80]. Therefore, the following material presented will be with regards to linear viscoelastic theory of materials.

The experimentation of viscoelastic materials strives to define observable phenomenological effects as material constants that can be compared and analyzed with other materials. In order to observe the time dependent stiffness feature present in viscoelastic materials, the two most common experimental techniques for measuring viscoelasticity are uniaxial stress relaxation, creep, and in some cases, sinusoidal loading.

The first experimental technique for measuring viscoelasticity is stress relaxation. Stress relaxation is the observed effect on the output stress of a viscoelastic material while a strain is applied in a given period of time. In the simplest form, the stress relaxation of instantaneous strain which is held constant for all time can be seen in Figure 12. The basic form of the equation for the time dependent stiffness in stress relaxation is as follows:

$$E_{rel}(t) = \frac{\sigma(t)}{\varepsilon_0} \tag{21}$$

where $\sigma(t)$ is the observed stress as a function of time, ε_0 in this case is a static strain held constant for all time, and $E_{rel}(t)$ is the time dependent modulus. For stress relaxation, the aggregate modulus of the material softens and the normal stress decreases as time goes on. The key for reconstructing the stress relaxation is choosing an appropriate representation for $E_{rel}(t)$. In the system in Figure 12, a model known as a Standard Linear Solid (SLS) is used to represent a linear viscoelastic material. This model will be more explicitly defined at the end of this chapter.

For a short time, the stress is a sum of what is known as the “glassy” modulus E_g and an equilibrium “rubbery” modulus E_r. Over a period of time, the combined moduli decreases as the glassy modulus converges to zero and only the rubbery modulus remains while strain is held constant. The term “glassy” refers to the component of the viscoelastic stiffness before any relaxation has occurred. The term “rubbery” refers to the component of the viscoelastic material where the stiffness has softened post relaxation.

The characteristic relaxation time at which the stress is equal to ${}^{1}/_{e}$ of the original stress is denoted as τ_r and called the Relaxation Time Constant. In reality, the input strain is not an instantaneous step function as seen in Figure 12, but rather a ramp function of constant strain rate, or an arbitrary loading history, which can make stress relaxation difficult to interpret.

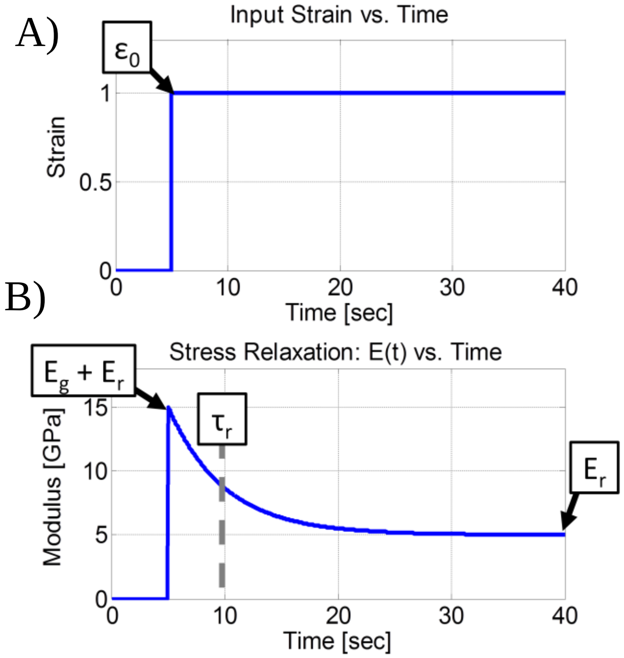

Figure 12. A) Input strain versus time for stress relaxation of a linear viscoelastic material. B) The time dependent relaxation modulus of a viscoelastic material. The system has a glassy modulus (E_g) of 10 GPa, a rubbery modulus of 5 GPa, and a relaxation time of 5 seconds. The strain is a unit step function which is ε_0 at 5 seconds.

The second experimental technique for measuring viscoelasticity is creep. Creep, like stress relaxation, is an observed phenomenological effect where the stress is now the input recorded in the experiment, and strain is recorded as the output (Figure 13). Similar to the relaxation modulus, the creep compliance function is the ratio of strain to stress and is shown below:

$$C_{crp}(t) = \frac{\varepsilon(t)}{\sigma_0} \tag{22}$$

where $\varepsilon(t)$ is the observed strain as a function of time, σ_0 in this case is a static stress held constant for all time, and $C_{crp}(t)$ is the creep compliance of the material. Figure 13 presents a linear viscoelastic case where the strain begins at an initial "glassy" compliance value C_g, and over time arrives at a "rubbery" equilibrium value of C_r. Creep also has a characteristic time called the Retardation Time Constant, denoted as τ_c. Additionally, the input stress does not behave in the instantaneous step manner as shown in the example, but in a manner like the strain rate history of stress relaxation. Although it is true that the stress relaxation and creep tests are related by $E_g = 1/C_g$ and $E_r = 1/C_r$, the characteristic times vary, and in particular, the stress relaxation approaches equilibrium more quickly than the creep ($\tau_r < \tau_c$) [80].

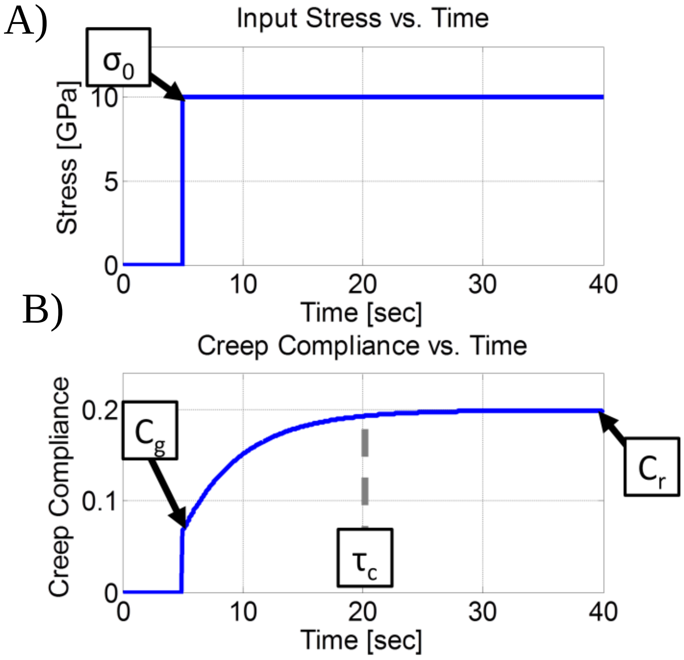

Figure 13. A) Input stress versus time for creep compliance of a linear viscoelastic material. B) The time dependent creep compliance of a viscoelastic material. The system has a glassy compliance (C_g) of 0.067, a rubbery compliance of 0.2, and a relaxation time of 15 seconds. The strain is a unit step function which is σ_0 at 5 seconds. The creep data shown here is the same system as that of Figure 12.

The third experimental technique for measuring viscoelasticity involves using a sinusoidal input of stress to record a steady state sinusoidal output of strain. In order for the information of this technique to be accurate, the probe of the testing apparatus must be in contact with the sample the entire time. The phase difference between the steady state strain oscillations and the input stress oscillations can then be used to separate the modulus into real and imaginary components. This complex modulus is a composite value where the real part is a measurement of conservative interactions and the imaginary component is a measurement of dissipative interactions. The terms storage and loss moduli are used to describe these conservative and dissipative subdivisions of the complex modulus. In AFM, the force modulation technique implements this style of testing and can collect the two conservative and dissipative moduli for single point analysis [43]. Additional work by Yuya *et. al.* used the complex wavenumbers of the amplitude and phase plots in conjecture with Contact Resonance AFM (CR-AFM) to also extract these moduli. In their study, a reference material was used for comparison and demonstrated this method on polymethyl methacrylate (PMMA) films [50]. Additional tests were conducted on polypropylene and polystyrene samples by Killgore *et. al.*, and the method was extended to line raster scanning using the dual AC resonance tracking (DART) method [81].

Although the recent methods utilizing this testing technique are useful for extracting viscoelastic information, they still do not fully characterize the surface. Moreover, the sinusoidal loading testing technique for viscoelastic materials is not applicable to IC-AFM where the surface is not always in contact with the probe. The extraction of viscoelastic materials of an AFM operating in IC-AFM require the combined theory of stress relaxation and creep, which will be fully addressed in the VETICA method of Chapter 3.

Several analytical models have been derived for linear viscoelasticity to extract the material properties using the stress relaxation/creep in AFM. The viscoelastic responses of materials are modeled in the form of rheological models using springs and viscous dashpots to represent the elements that comprise a viscoelastic material. These linear Hookean springs have the following stress-strain relationship:

$$\sigma_s(t) = k\varepsilon_s(t) \tag{23}$$

where the spring k is analogous to the Young's Modulus and the strain $\varepsilon_s(t)$ and stress $\sigma_s(t)$ are analogous to the displacement and force of the spring, respectively.

The Newtonian dashpots, which are rate dependent non-conservative elements displaying a fluid-like nature, have the following relationship to stress and strain rate:

$$\sigma_d(t) = c\dot{\varepsilon}_d(t) \tag{24}$$

where the dashpot c is analogous to the viscosity of the material while the strain rate $\dot{\varepsilon}_d(t)$ and stress $\sigma_d(t)$ are analogous to the velocity and force of the dashpot, respectively. Using a combination of these discrete linear elements, one can formulate models by which both the elastic and viscous nature of viscoelastic materials can be described.

2.5.2 The Maxwell Model

The Maxwell model is a basic two-element rheological model for viscoelasticity comprised of an elastic spring (k_m) and a viscous dashpot (c) and is displayed in Figure 14.

Figure 14. Maxwell Configuration.

When elements are connected in series, the stress remains constant, while stress varies across each element. The following equations formulate the constitutive equation for the Maxwell model:

$$\sigma = \sigma_s = \sigma_d \tag{25}$$

$$\varepsilon = \varepsilon_s + \varepsilon_d \tag{26}$$

Using the equations from (23) and (24):

$$\dot{\varepsilon} = \dot{\varepsilon}_d + \dot{\varepsilon}_s = \frac{\sigma}{c} + \frac{\dot{\sigma}}{k} \tag{27}$$

Rearranging and multiplying through by k and setting $\tau = c/k$:

$$k\dot{\varepsilon} = \dot{\sigma} + \frac{1}{\tau}\sigma \tag{28}$$

Equation (28) is the constitutive equation for the Maxwell model relating stress to strain where there is now the characteristic relaxation time τ which depends on the mechanical elements of the system and is physically the time it takes the system to relax to $1/_e$ of its original value. The Maxwell model is a good representation of a viscoelastic material under stress relaxation tests, but does not retain accuracy for creep [51]. Because of this inaccuracy, this thesis cannot solve for viscoelastic materials using only the Maxwell model.

2.5.3 The Kelvin-Voigt Model

The Kelvin-Voigt model is a complimentary two-element rheological model to the Maxwell. Instead of placing the spring and dashpot in series, they are now arranged in a parallel configuration as seen in Figure 15.

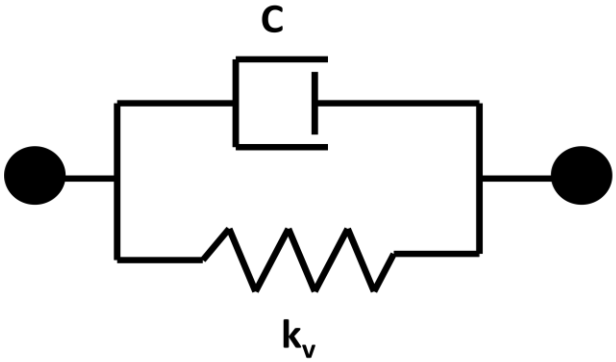

Figure 15. Kelvin-Voigt configuration.

Elements in parallel exhibit an opposite behavior to elements in series where the strain now remains constant while stress varies across the elements. In the following equations, the constitutive equation for the Kelvin-Voigt model is derived:

$$\sigma = \sigma_s + \sigma_d \tag{29}$$

$$\varepsilon = \varepsilon_s = \varepsilon_d \tag{30}$$

Using the equations from (23) and (24):

$$\sigma = c\dot{\varepsilon} + k\varepsilon \tag{31}$$

The Kelvin-Voigt model is capable of recovering the creep compliance of a material, but stress relaxation recovery suffers in accuracy [51]. In the case of IC-AFM, both creep and stress relaxation occur within a single tap due to the contact to non-contact nature. Therefore, a third model will be used where the benefits of the Maxwell and Kelvin-Voigt models are combined.

2.5.4 The Standard Linear Solid (SLS)

In this work, the Standard Linear Solid (SLS) rheological model containing three mechanical elements is implemented to represent a linear viscoelastic material surface (Figure 16). The model is a combination of the Maxwell and Kelvin-Voigt model where a Maxwell element is connected in parallel to a second spring. This configuration is also known as a Zener model. The SLS model provides the simplest form of a linear viscoelastic approximation which can reproduce both stress relaxation and creep compliance. This model will conserve computational expenses and act as the initial step towards defining a more complex model capable of capturing the full non-linearity of viscoelasticity. In the SLS configuration (Figure 16), the values for the instantaneous and equilibrium stiffness of the surface are given as:

$$K_{glassy} = k_0 + k_{inf} \tag{32}$$

$$K_{rubbery} = k_{inf} \tag{33}$$

The term k_0 refers to the spring, which deforms with the same viscous stress experienced by the dashpot in the Maxwell arm. The term k_{inf} refers to the spring in parallel with the Maxwell arm, which still exhibits a restoring force even as time approaches infinity, and k_0 has relaxed. The viscous time-dependent dashpot element, c_d, introduces viscous damping to the model.

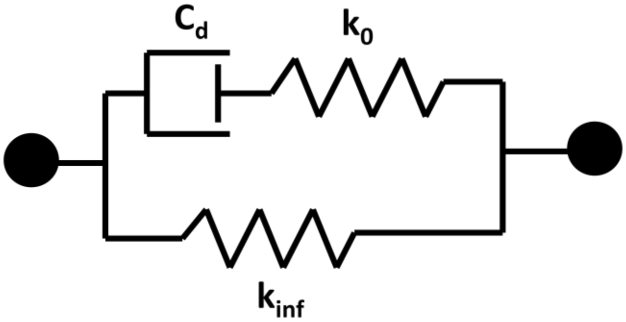

Figure 16. Standard Linear Solid (SLS) configuration comprised of an elastic stiffness (k_{inf}) in parallel with a Maxwell element (c_d and k_0).

The SLS also possesses a mechanically equivalent configuration to that of Figure 16 where a Kelvin-Voigt model is placed in series with an elastic spring. Appendix A shows the relationship between these two configurations. For the purposes of this study, the Zener configuration in Figure 16 will be implemented into the numerical simulations.

The constitutive equations for the SLS follow a derivation similar to that of the Kelvin-Voigt and Maxwell models and is as follows:

$$\sigma_{total} = \sigma_m + \sigma_{k\,inf} \tag{34}$$

$$\dot{\sigma}_{total} = \dot{\sigma}_m + \dot{\sigma}_{k\,inf} \tag{35}$$

And:

$$\varepsilon_{total} = \varepsilon_m = \varepsilon_{k\,inf} \tag{36}$$

$$k_{total} = \sigma_{total}/\varepsilon_{total} \tag{37}$$

In this case, index "m" stands for the Maxwell model and k_{inf} is the unrelaxed elastic spring. Inserting the constitutive equations for the Maxwell model and the elastic spring in equations (28) and (23) into (35):

$$\dot{\sigma} = k_0\dot{\varepsilon} - \frac{k_0}{c_d}\sigma_m + k_{inf}\dot{\varepsilon} \tag{38}$$

Substituting in $\sigma_m = \sigma - \sigma_{k\,inf}$ and rearranging for $\dot{\varepsilon}$:

$$\dot{\sigma} = k_0\dot{\varepsilon} - \frac{k_0}{c_d}\left(\sigma - \sigma_{k\,inf}\right) + k_{inf}\dot{\varepsilon} \tag{39}$$

$$\dot{\sigma} = k_0\dot{\varepsilon} - \frac{k_0}{c_d}\left(\sigma - k_{inf}\varepsilon\right) + k_{inf}\dot{\varepsilon} \tag{40}$$

$$\dot{\varepsilon} = \left(k_0 + k_{inf}\right)^{-1}\left(\dot{\sigma} + \frac{k_0}{c_d}\sigma - \frac{k_0 k_{inf}}{c_d}\varepsilon\right) \tag{41}$$

And substituting $\tau = c_d/k_0$:

$$\dot{\varepsilon} = \left(k_0 + k_{inf}\right)^{-1}\left(\dot{\sigma} + \frac{1}{\tau}\sigma - \frac{k_{inf}}{\tau}\varepsilon\right) \tag{42}$$

This equation (42) is for the constitutive equation of the SLS which relates the stress and strain to the three mechanical elements. As previously stated, additional and more complex models using springs and dashpots are possible but the SLS is the simplest form that can recover stress relaxation and creep and is sufficient for the scope of this work on linear viscoelasticity. The constitutive equations for viscoelasticity using the mechanical models are ordinary time-differential equations that can be solved using a popular method known as the “correspondence principle” [80]. The general concept of the correspondence principle is taking the time-dependent differential equation from the constitutive elasticity equations, transforming them into the Laplace domain, solving for the output, and inverting the expressions back to the time domain. Applying the correspondence principle to the constitutive equation yields the following expressions for the stress relaxation and creep compliance with a constant applied stain and stress, respectively (42):

$$E_{rel}(t) = K_r + \left(K_g - K_r\right)\exp\left(\frac{-t}{\tau_r}\right) \tag{43}$$

where: $K_r = k_{inf}, K_g = k_{inf} + k_0$, and $\tau_r \equiv \frac{c_d}{k_0}$

$$C_{crp}(t) = C_g + (C_r - C_g)\left(1 - \exp\left(\frac{-t}{\tau_c}\right)\right) \tag{44}$$

where: $C_g = \frac{1}{k_{inf}+k_0}, C_r = \frac{1}{k_{inf}}$, and $\tau_c = \tau_r \frac{k_{inf}+k_0}{k_{inf}} = \frac{c_d(k_{inf}+k_0)}{k_0 k_{inf}}$

where subscripts *r* and *g* denote rubbery and glassy modulus, respectively. The next section will discuss the applications of these solutions to the differential equation as found in literature.

2.5.5 Current Work with the SLS in AFM

The most common method to apply the SLS solutions for stress relaxation and creep compliance are done so in integral form using what is known as the "Boltzman Superposition Principle" [82]. In this principle, each loading step makes an contribution to a cumulative loading history. In other words, the relaxation or creep depends on the history of the loading. In order to solve this, a convolution integral is created which convolves the input load, with the relaxation/compliance function. The following section explains the case for stress relaxation which can be applied to creep.

Consider a stress $\sigma_1(t)$ at a time t due to the application of a small applied strain $\Delta\varepsilon_1$ at an earlier time ζ_1 before *t*. Using the relaxation equation from (21) it can be shown that:

$$\sigma_1(t) = E_{rel}(t - \zeta_1)\Delta\varepsilon_1 \tag{45}$$

For another stress at a second loading time:

$$\sigma_2(t) = E_{rel}(t - \zeta_2)\Delta\varepsilon_2 \tag{46}$$

For a linear viscoelastic material, the superposition of the two stresses is:

$$\sigma(t) = \sigma_1(t) + \sigma_2(t) = E_{rel}(t - \zeta_1)\Delta\varepsilon_1 + E_{rel}(t - \zeta_2)\Delta\varepsilon_2 \qquad (47)$$

As the number of loading increments increases in a given time interval, a continuous (integral) form of the loading history arrives:

$$\sigma(t) = \sum_j \sigma_j(t) = \sum_j E_{rel}(t - \zeta_j)\Delta\varepsilon_j \qquad (48)$$

$$\sigma(t) = \int_{-\infty}^{t} E_{rel}(t - \zeta)d\varepsilon = \int_{-\infty}^{t} E_{rel}(t - \zeta)\frac{d\varepsilon(\zeta)}{d\zeta}d\zeta \qquad (49)$$

The final integral is what is known as the Boltzman Superposition Principle. In literature, Lee and Radok [83] and Ting [84] formulated a theory of viscoelastic indentation of a half space by a spherical indenter using the Boltzman Superposition Principle. Lee and Radok were able to solve for a case with monotonically increasing contact radius of a spherical indenter and Ting was able to expand this theory to arbitrary indenter profiles. The problem arises from the convolution equation because a monotonically increasing contact radius implies that IC-AFM, where the tip indents and then retracts in an oscillation cycle, is not suited for the theory. In implementation, a group led by Cheng *et. al.* developed an analytical method to extract the three elements of the SLS in viscoelastic spherical indentation using the Boltzman Superposition Principle and functional equations [85, 86]. Although the work yielded successful results for stress relaxation and creep tests, the tests were based on constant contact and knowledge of the requirement to record the entire relaxation/creep process – neither of which are possible in IC-AFM.

Specifically to AFM, Attard discusses the applicability and consequences of contact models such as Hertz, DMT, and JKR with regards to modeling viscoelastic indentation with a spherical tip [23, 39, 87-89]. As a result, the Hertzian geometrical consideration of spherical indentation from the tip will be neglected in this thesis by translating the linear viscoelastic relationships of intensive material measurements of the SLS (Elastic stiffness [Pa] and dynamic viscosity [Pa·s]) to extensive properties of the body which already take into account material, geometrical shape, and boundary conditions (stiffness [N/m] and damping [kg/s]). The stress [Pa] and strain [m/m] will be converted to force [N] and displacement [m] to make the results more comparable to AFM signal information. Although this translation may seem like an over-simplification of the system, it is essential in understanding the characteristics of viscoelasticity and creating an ideal scenario under which the VETICA method can explore feasibility. Through using extensive properties, this study is not limited to a particular tip geometry or scale size, making the results and conclusions presented relevant to the physics of the surface composition and not the contact mechanics problem. The equivalent approximations of conversions from results back to intensive properties will be discussed in Chapter 4.

Therefore the proposed method in this thesis shall include the implementation of the Standard Linear Solid and represent the linearly viscoelastic interaction between tip in sample in terms of extensive properties such as springs in dashpots to formulate the VETICA method, which is outlined in detail in Chapter 3, and extract material properties.

Chapter 3: Research Methods and Procedures

This chapter details the research methods of the work. The first two sections discuss the computational modeling for the THC and SLS interaction, and the final section discusses the process of VETICA in order to extract viscoelastic material properties.

3.1 Modeling the THC

The AFM operating in IC-AFM and utilizing the THC as a probe is modeled in the C coding language and post-processed using MATLAB (The Mathworks Inc.). The following section discusses the numerical integration of the THC equations of motion, the implementation of a feedback Proportional Integral Derivative (PID) controller, and the representation of the tip-sample interaction force F_{ts}.

3.1.1 Integrating the Equations of Motion of the THC

As previously discussed in Chapter 2, the THC can be represented as a point-mass model consisting of two masses (flexural cantilever, and tip/paddle) with subsequent spring constants, environmental damping, and quality factors. Using the recent work by Solares and Hölscher [76], this thesis elects to use the decoupled THC configuration of the mechanical representation of the system and integrate the equations of motion found in equations (15) and (16). The integration is performed using the Verlet integration algorithm [90], giving a local error to the fourth order on the position and a second order error on the velocity. The definition of the algorithm can be found in Appendix B. The code outputs a position, velocity and acceleration for the cantilever and paddle/tip for each time step. The time step for all the simulations presented here are 0.025 ns and the print time for position and velocity range from 0.125ns to 8ns. The period for the oscillation of the highest resonant frequency (1.5 MHz for the paddle) simulated is 667 ns, which is approximately 26.7x10^4 times greater than the print step. Figure 17 shows the steady state oscillations of the cantilever and paddle using the Verlet algorithm. The time scale does not begin at zero because the data is taken from a simulation after steady state has been reached. Figure 18 shows the simulated transition from transient to steady state oscillations of IC-AFM to demonstrate that steady state is achieved fairly quickly in the air environment (i.e., paddle Q = 1000, cantilever Q = 100). In order to adjust the base of the cantilever to changes in topography and achieve the steady state amplitude set point ratio, a PID controller must be implemented.

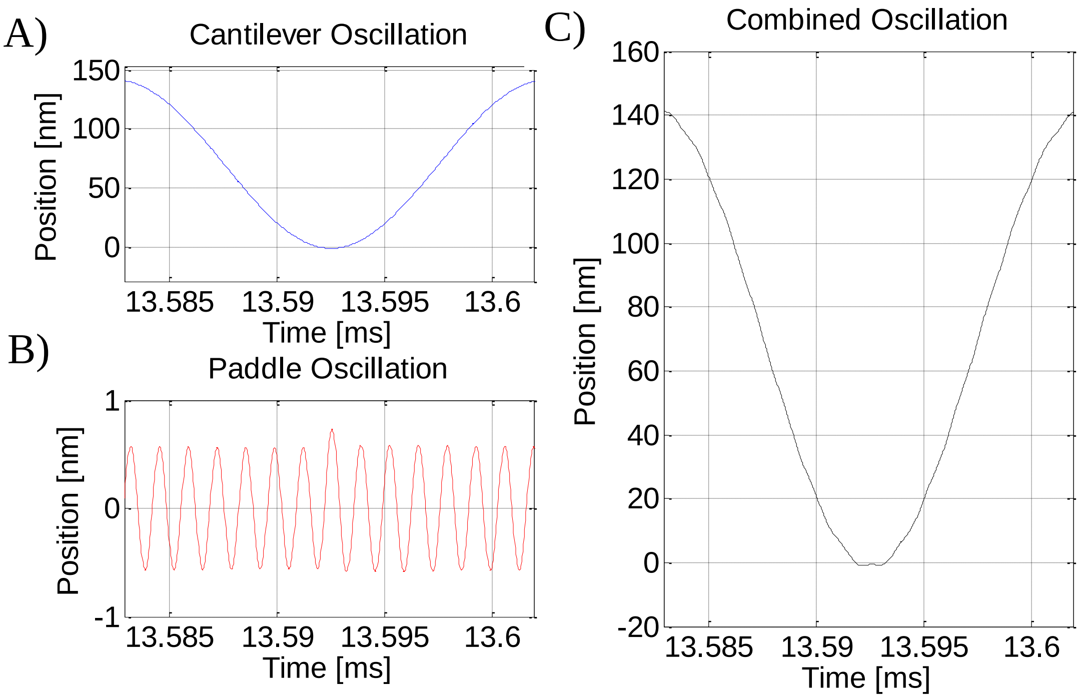

Figure 17. A) The simulated oscillation of only the flexural cantilever using the Verlet algorithm. B) The simulated oscillation of only the high frequency torsional paddle/tip, note the higher excitation peak when contact occurs. C) The combined cantilever and paddle trajectory.

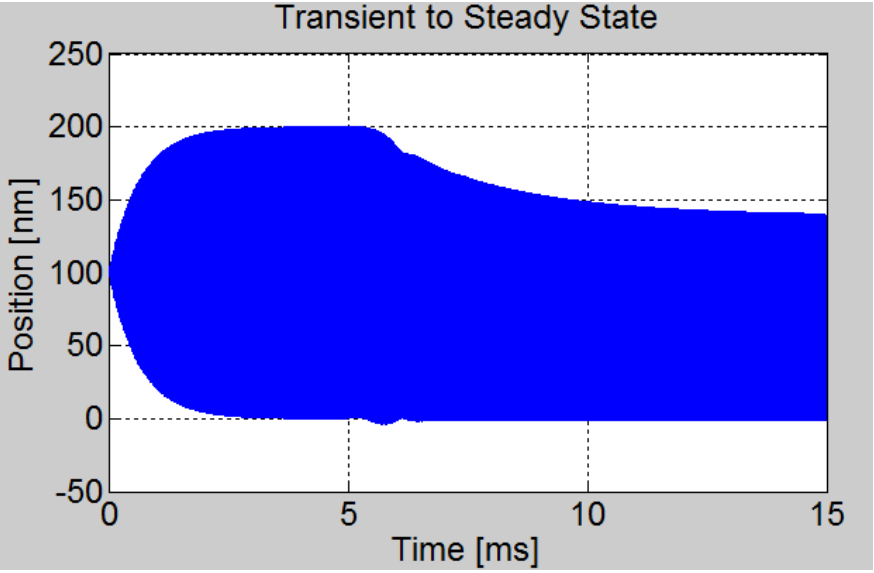

Figure 18. Oscillations of the THC probe over time showing the transient to steady state process. First, the cantilever is oscillated at resonance at an initial base distance of 100 nm with a free amplitude of 100nm. At ~5ms, the base is lowered by the PI controller until a steady state amplitude based on a set point of 70% (or 70nm) is achieved at ~15ms.

3.1.2 Implementing the PID controller

The PID controller in code uses a logic in which errors based on the current and previous running amplitudes, the feedback of the amplitude set point, and the gain constants are used to correct the base position. For the integral (I) part of the controller correction, the difference between the amplitude set point and the previous ten running amplitudes are used in conjunction with an appropriate gain to correct the signal. The proportional (P) part of the controller correction is implemented by multiplying the difference between the current running amplitude and the amplitude set point by an appropriate gain. The gains are carefully chosen so that a steady state tapping interaction occurs quickly and before the steady state data is collected, and responsive enough to adjust to surface height changes. The derivative (D) portion of the controller is not used in the code because the transients in IC-AFM behave in an unpredictable manner due to the complexities of the tapping process. The derivative portion of a PID is known to slow the transient response and amplify noise, thereby increasing the negative effects [91]. Figure 19 displays a pseudocode describing the correction process of the PI controller for each iteration of the integration.

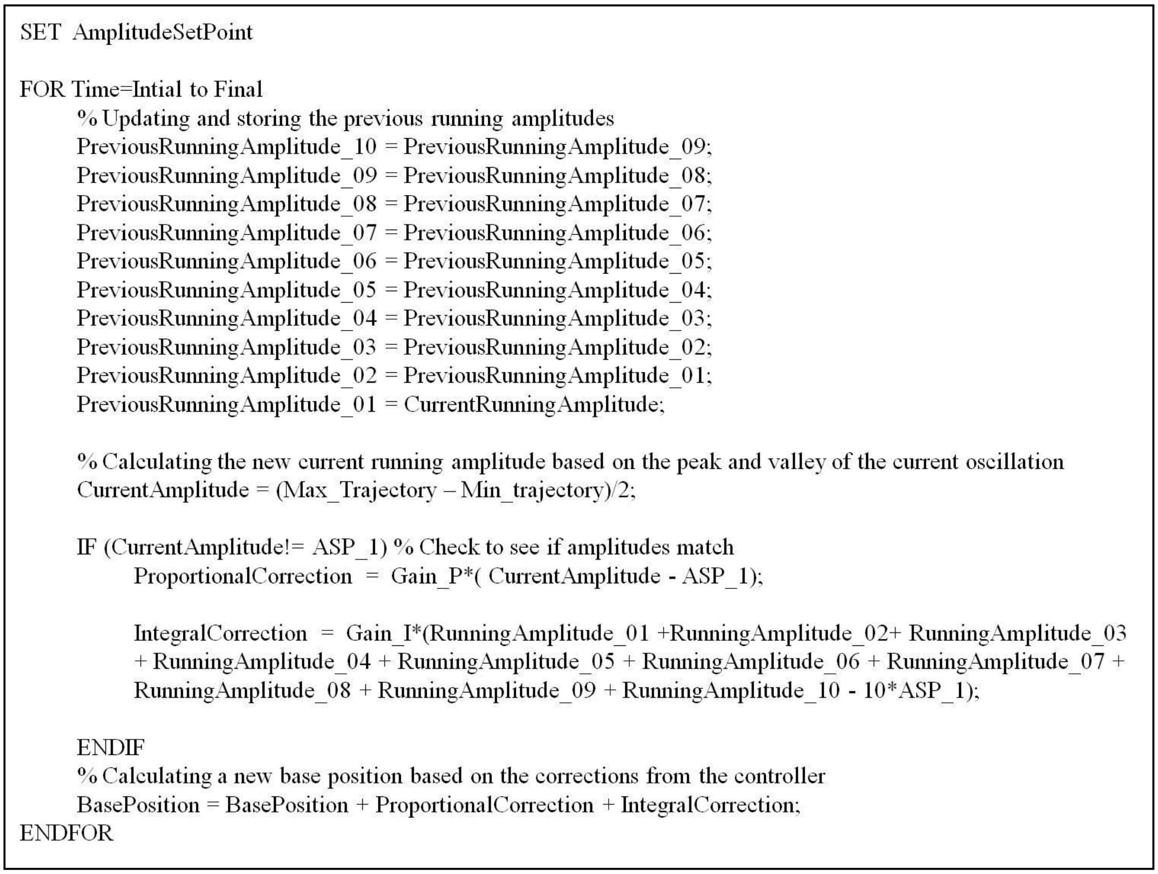

```
SET  AmplitudeSetPoint

FOR Time=Intial to Final
        % Updating and storing the previous running amplitudes
        PreviousRunningAmplitude_10 = PreviousRunningAmplitude_09;
        PreviousRunningAmplitude_09 = PreviousRunningAmplitude_08;
        PreviousRunningAmplitude_08 = PreviousRunningAmplitude_07;
        PreviousRunningAmplitude_07 = PreviousRunningAmplitude_06;
        PreviousRunningAmplitude_06 = PreviousRunningAmplitude_05;
        PreviousRunningAmplitude_05 = PreviousRunningAmplitude_04;
        PreviousRunningAmplitude_04 = PreviousRunningAmplitude_03;
        PreviousRunningAmplitude_03 = PreviousRunningAmplitude_02;
        PreviousRunningAmplitude_02 = PreviousRunningAmplitude_01;
        PreviousRunningAmplitude_01 = CurrentRunningAmplitude;

        % Calculating the new current running amplitude based on the peak and valley of the current oscillation
        CurrentAmplitude = (Max_Trajectory – Min_trajectory)/2;

        IF (CurrentAmplitude!= ASP_1) % Check to see if amplitudes match
                ProportionalCorrection  =  Gain_P*( CurrentAmplitude - ASP_1);

                IntegralCorrection  =  Gain_I*(RunningAmplitude_01 +RunningAmplitude_02+ RunningAmplitude_03
                + RunningAmplitude_04 + RunningAmplitude_05 + RunningAmplitude_06 + RunningAmplitude_07 +
                RunningAmplitude_08 + RunningAmplitude_09 + RunningAmplitude_10 - 10*ASP_1);

        ENDIF
        % Calculating a new base position based on the corrections from the controller
        BasePosition = BasePosition + ProportionalCorrection + IntegralCorrection;
ENDFOR
```

Figure 19. Pseudocode for PID controller logic. The FOR loop represents the time iterative stepping of the integration. The IF loop calculates the correction from a PI controller; the derivative is not used in this control scheme.

3.1.3 Representing the Force

The tip-sample interaction force emerges from long-range van der Waals attraction forces between the tip of the THC and sample and short-range repulsive forces that are caused by the resistance of the material to deform. In the case of the SLS, this resistance is quantified in the form of mechanical springs, with a viscous dashpot providing a fluid-like flow response to simulate viscoelasticity. A diagram of the interaction between the THC and SLS is displayed in Figure 20.

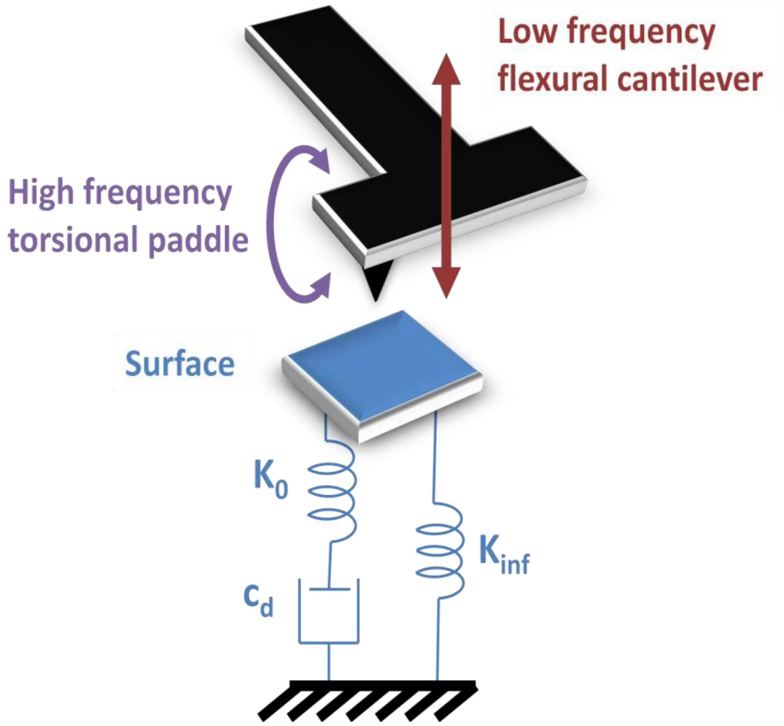

Figure 20. The THC probe interaction with the surface simulated as an SLS. The high frequency paddle acts as the sensor to detect the interaction force F_{ts} while the low frequency cantilever is driven by the piezo base (not pictured).

In addition to the restoring spring force of the cantilever and the viscous damping force from the ambient environment acting on the tip, the long range force of van der Waals from equation (3) also acts as the interaction force between tip and sample when not in contact. As stated before in Chapter 2, a value of a_0 above the surface is used to denote the vertical distant at which there is a transition from non-contact to contact regime. Although the main excitation for the paddle is provided by the surface stiffness, the van der Waals force will lightly drive the paddle as the tip approaches the surface. This light excitation is shown in Figure 21. For the typical dynamic operation in IC-AFM, the taps are sufficiently hard enough such that the van der

Waals forces influence on the paddle are negligible compared to the repulsive forces exerted by the surface.

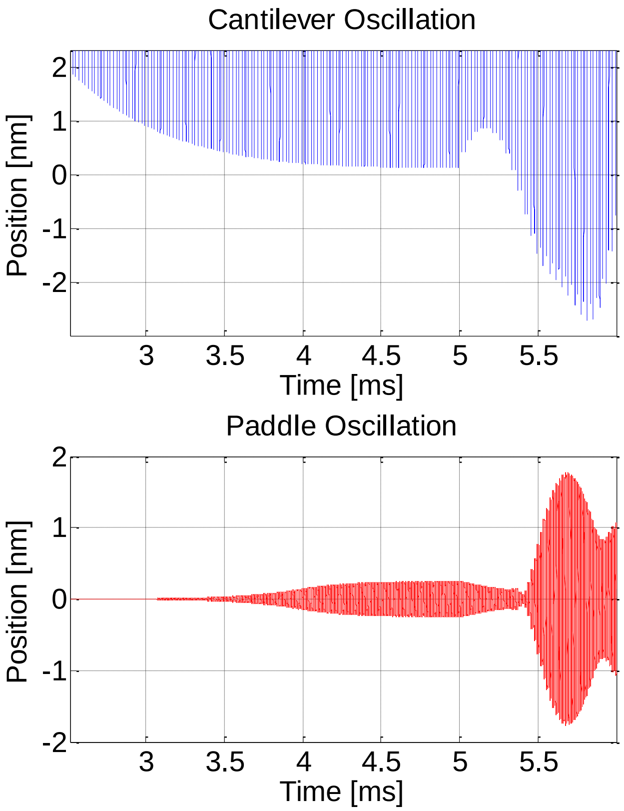

Figure 21. Excitation of the paddle from non-contact van der Waals forces. Far from the surface while the cantilever oscillations (A) are greater than 1nm away, the paddle amplitude is nearly zero. As the base is lowered and the oscillations approach the surface (up until 5ms), the non-contact forces acting on the paddle cause the light vibrations seen. The “tapping” transient begins at 5ms.

3.2 Modeling the SLS

The surface for the simulations is represented by a linear viscoelastic mechanical model with three discrete elements: two elastic springs, and a single viscous dashpot. The methods for simulating the Standard Linear Solid (SLS) are detailed below. The governing equations of motion for the non-contact and contact cases are presented and notes on simulation features are given in the following sections.

3.2.1 Equations of Motion of the SLS

The numerical integration of the SLS requires a set of coordinates to measure the position of the surface in simulation. The SLS is considered a “one and a half” degree of freedom system [92] because both the surface and the dashpot have spatial coordinates (X and X_d) as seen in Figure 22, but only the surface contains the mass of the material. The coordinates are chosen as “X” for the surface to differentiate them from the “Z” coordinates which relates to the probe. This feature of the model does not allow for the equations of motion for the SLS to be expressed simply in state space, as is possible with integer valued degree of freedom systems. Nevertheless, the equations that govern the coordinates can be found by using Hooke’s Law for the spring force relationship and the damping force which is linearly proportional to the velocity of the dashpot.

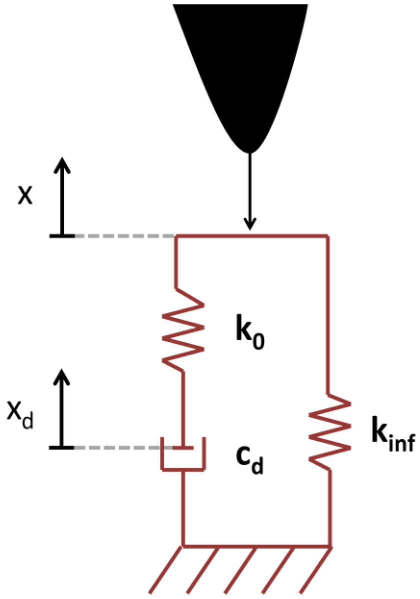

Figure 22. Spatial coordinates for the SLS surface. X is the coordinate of the actual surface, which depends on equilibrium force between tip and sample. X_d measures the position of the dashpot and consequently dashpot velocity, which governs the viscous force experienced by the surface.

The Hookean spring force and viscous damping force can be expressed as follows for the SLS coordinates:

$$F_H = -k_{inf}X - k_0(X - X_d) \tag{50}$$

$$F_c = -c_d\dot{X}_d \tag{51}$$

where F_H is the Hookean spring force on the model, and F_c is the damping force. Due to the configuration of the SLS being a Maxwell element in parallel with a single spring element, F_H is the linear combination of the forces experienced in each element. Using these constitutive equations for force of the SLS, the force experienced by the surface can be divided into two regimes: the contact and non-contact.

3.2.2 Representing the Force: Contact Regime

For the contact regime, the tip (z_t) is assumed to be at the same spatial coordinate as the surface (X). This assumption implies that the tip position is computed as the surface position and then used as the "input" to the SLS equations of motion and the resulting repulsion force is calculated as the "output." Figure 23 displays the interaction forces of the SLS configuration during the contact regime. The forces for the components of the Maxwell element (F_{m1} and F_{m2}) are in series and therefore are equal in magnitude and direction.

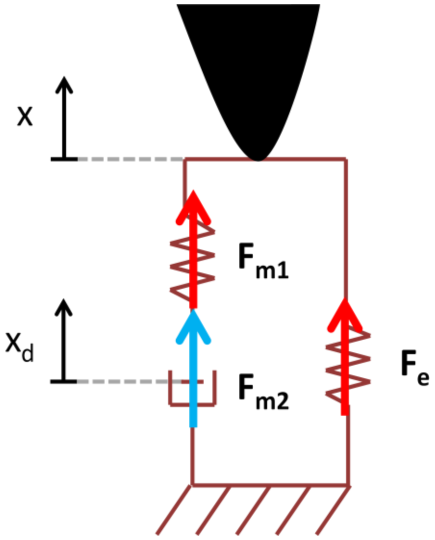

Figure 23. Tip and SLS in contact regime of the tapping oscillation. The red arrows indicate forces experienced by the elastic and Maxwell springs. The blue arrow indicates the force experienced by the dashpot component of the Maxwell element. The direction of the arrows is under the assumption that the tip is pushing in the negative *X* direction and the velocity of the dashpot is also in the negative X_d direction. F_{m1} and F_{m2} are equal in magnitude and direction but not necessarily equal in magnitude to F_e.

In simulation the following steps (a. – g.) are followed to solve for the coordinates, interaction forces, and F_{ts} in the SLS during the contact regime (when $z_{tip} < X + a_0$):

a. Current *X* position: $$X = z_{tip} \quad (52)$$

b. F_e calculation: $$F_e = -k_{inf}X \quad (53)$$

c. F_{m2} calculation: $$F_{m1} = F_{m2} = -k_0(X - X_{d\_previous}) \quad (54)$$

d. X_d velocity: $$\dot{X}_d = -\frac{F_{m2}}{c_d} \quad (55)$$

e. Current X_d position: $$X_d = X_{d\_previous} + \dot{X}_d \Delta t \quad (56)$$

f. F_{VdW} calculation: $$F_{VdW} = -\frac{A_H R_{tip}}{6{a_0}^2} \quad (57)$$

g. F_{ts} imparted on the tip: $$F_{ts} = Fe + Fm2 + F_{VdW} \quad (58)$$

In order to make the system physically realistic, certain constraints must be enforced in the contact regime. The first constraint is that the dashpot coordinate (X_d) must not surpass the tip/surface position along the same direction of motion. This case could occur if the dashpot is small, thus amplifying the dashpot velocity and larger displacement jumps over the time step. Physically it is not possible for the dashpot coordinate to surpass the surface position because the dashpot is always relaxing to an equilibrium position where the k_0 spring exhibits zero force. Hence, surpassing the surface position in the direction of motion would imply a non-zero force would be equilibrium for the model.

A second constraint of the simulation is an assumption that the tip and sample do not separate during the approach of the contact regime. That is, the definition of a "tap" is one contact, and one separation of the tip and surface. This assumption is valid so long as the paddle amplitudes are relatively small when compared with the cantilever amplitudes. The high frequency paddle usually experiences several oscillations during the contact with the surface. If the paddle amplitude is sufficiently large compared to the flexural, the tip could contact and separate from the surface more than once within a single tap. In reality, this scenario is highly unlikely because the natural operating amplitudes of the THC probe are largely restricted by geometry and the paddle is on the order of twenty times shorter than the cantilever [30]. Additionally, this assumption and constraint is placed in the computations to increase robustness.

3.2.3 Representing the Force: Non–Contact Regime

Within the non-contact regime, tip and surface are no longer sharing the same spatial coordinate and the surface is free to relax back to the initial equilibrium position. The internal force from the equilibrium spring (k_{inf}) restoring the material is the "input" and the position of the surface is the "output." Figure 24 displays the SLS internal force configuration during non-contact.

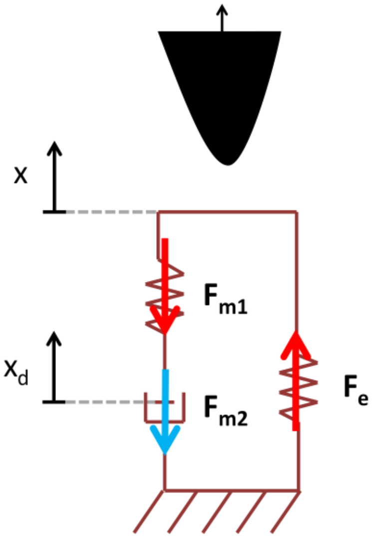

Figure 24. Tip and SLS in non-contact regime of the tapping oscillation. The arrows and variables are the same as Figure 23 except that now F_{m1} and F_{m2} are equal in magnitude and opposite in direction to F_e.

The coordinates of the SLS during non-contact are calculated via the force balance between the two elements in the following steps (h. – n.).

h. F_{VdW} calculation:
$$\mathrm{F_{VdW}} = -\frac{A_H R_{tip}}{6d^2} \tag{59}$$

i. F_e calculation:
$$F_e = -k_{inf} X_{previous} - \mathrm{F_{VdW}} \tag{60}$$

j. F_m calculation:
$$F_{m1} = F_{m2} = -F_e \tag{61}$$

k. X_d velocity:
$$\dot{X}_d = -\frac{F_{m2}}{c_d} \tag{62}$$

l. Current X_d position: $$X_d = X_{d\_previous} + \dot{X}_d \Delta t \tag{63}$$

m. Current X position: $$X = \frac{k_{inf}}{k_{inf} + k_0} X_d \tag{64}$$

n. F_{ts} imparted on the tip: $$F_{ts} = F_{VdW} \tag{65}$$

The force returned to the tip is only the long range van der Waals forces resulting from a tip-sample separation of d. In order to calculate the new position of the surface (X), the change in surface position (ΔX) must be calculated. Appendix C outlines the derivation for acquiring ΔX, and subsequently equation (64), from the force balance of the two sides of the SLS.

Similar to the contact regime, the simulation of the SLS in the non-contact regime has some constraints in place to make the computation more physically accurate. Like the contact regime, the dashpot is prevented from surpassing the surface position during the creep back to the equilibrium position. It should be noted that the effects of van der Waals forces are imparted on the surface, pulling it up towards the tip and effecting the position of the tip and dashpot. Van der Waals forces do not need to be considered for the surface during contact because the surface position is driven by the cantilever position and the F_{ts} experienced by the tip already includes F_{VdW}.

3.3 Viscoelasticity Extraction Technique for Intermittent Contact AFM (VETICA)

The method presented in this section is titled the Viscoelasticity Extraction Technique for Intermittent Contact AFM (VETICA) and is a process by which the dynamics and features of the measurable AFM data are used to approximate the material properties of the surface. In order to formulate any theory, certain assumptions must be made about the AFM system and surface.

The first assumption of the VETICA method is that the surface behaves like a linear viscoelastic material modeled as an SLS in the Zener configuration described in Chapter 2. This assumption is made because the values produced from the VETICA method will equate to the constants of k_{inf}, k_0 and c_d of that particular configuration of the SLS model. As previously stated, in nature few materials are simple enough to be described as linearly viscoelastic, however this method still provides a novel approach which serves as a first step to extracting viscoelastic properties in IC-AFM.

The second assumption of the VETICA method is an AFM imaging condition that requires that the probe oscillations and taps occur at the same horizontal position of the surface. This assumption means that the tip is not raster scanned across the surface, but rather that all taps occur at the same location. This assumption is critical for measuring and recovering the viscous information about the material. Chapter 4 will discuss the effect of the VETICA method on scan times of acquiring a full 256x256 pixel AFM image.

In order to visualize the tapping motion at one point, Figure 25 displays the diagram of the tip trajectory and surface profile versus time. Initially the surface is undeformed at a position of Z_1 and after separation at position Z'_1 and at time t_1 from the tap, it begins to creep back to the equilibrium zero position Z_1. However, before the surface can reach this point, the cantilever returns to the surface and the next sequential tap contacts the partially restored surface. This happens at position Z_2 and time t_2.

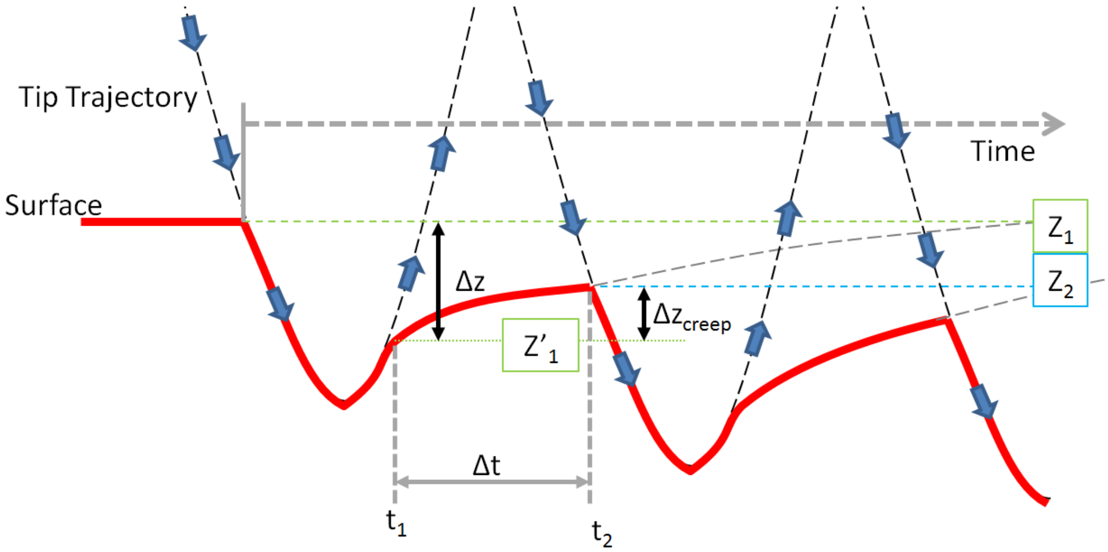

Figure 25. Diagram of the tip trajectory and surface profile versus time during sequential taps. Z_1 is the initial zero of the surface before any taps have occurred. Z'_1 and t_1 are the position and time, respectively, at which separation from the first tap occurs. Z_2 and t_2 are the position and time, respectively, at which the next consecutive tap makes contact.

The process shown in Figure 25 occurs for each sequential tap and over time the surface continues to deform until the restoring spring force from k_{inf} is large enough to restore the surface to a position where the current tap contact position is at the same position as the previous tap contact position (i.e. $Z_i = Z_{i-1}$). When this deformation is reached, the regime will be referred to as the "steady state zero reference equilibrium." Figure 26 displays the tip oscillation and the surface profile versus time from before the initial tap to the steady state zero reference equilibrium regime. The oscillating cantilever is lowered by the base at a constant rate using the PI controller until tap commences. The controller then adjusts the base of the cantilever to maintain a constant amplitude and the surface partially recovers the taps. After a period of time, the steady state zero reference equilibrium regime is reached and indicated on the figure. The VETICA method is not restricted to the taps occurring during the steady state zero reference equilibrium, but all data presented here is taken from that range because it showed the least instability.

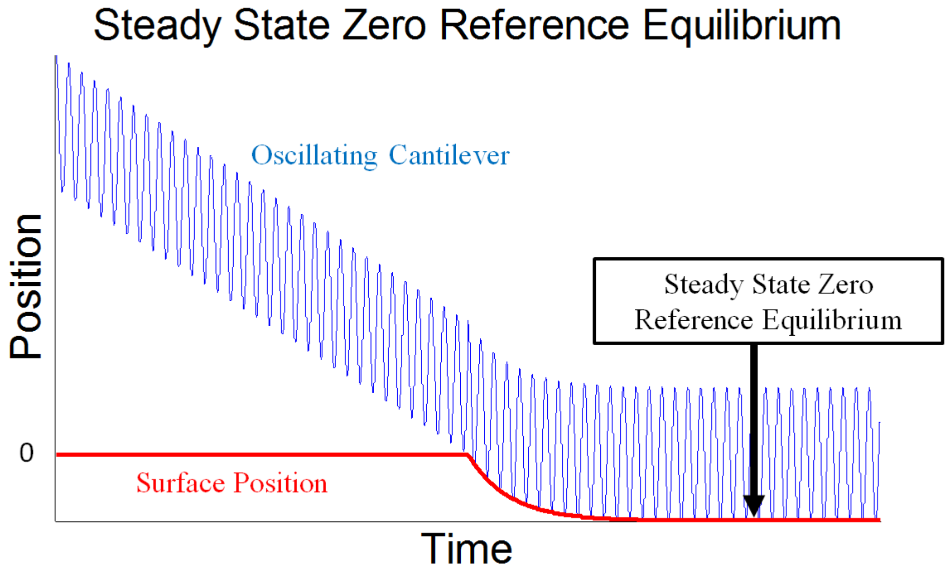

Figure 26. Diagram showing the "Steady State Zero Reference Equilibrium" that occurs as the sample deforms further from its original true zero position.

The ensuing description of the VETICA model will begin by discussing the VETICA sub-process, which will be referred to as Stage 1. Stage 1a is the non-contact regime of the oscillation where the SLS is creeping (equation (43)) due to the internal restoring force of k_{inf}. Stage 1b transitions to the contact regime where the stress relaxation equation (44) applies. Within Stage 1, variables are acquired from AFM signal data which are the characteristic material constants retardation time constant (τ_c) and the glassy stiffness (K_g). The second sub-process of VETICA (Stage 2) implements a non-linear least-squares fitting technique in MATLAB to solve for the three SLS material properties (k_{inf}, k_0, and c_d) using the Stage 1 variables: the tip penetration position given by z_{tip}, and F_{ts} data acquired from the Spectral Inversion Method. Figure 27 shows the flow chart from a broad perspective of the VETICA method.

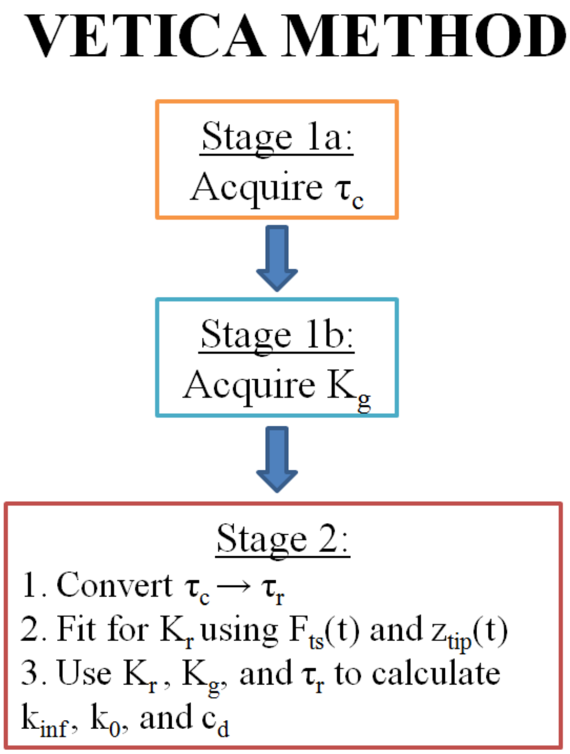

Figure 27. Flow chart of the VETICA method. Stage 1 is the extraction of material constants τ_c and K_g from the tip position, interaction force, and time signal of the AFM. Stage 2 is the recovery of the SLS mechanical elements k_{inf}, k_0, and c_d.

3.3.1 Acquiring the Retardation Time Constant τ_c (Stage 1a)

Stage 1 involves examining the dynamics of the THC in IC-AFM during the non-contact regime of the oscillation. The first Stage 1 variable is the characteristic time constant for creep τ_c known as the Retardation Time. As previously stated, the characteristic time is the time it takes for the deformation to creep to 1/e of the original indentation depth or in the form of an equation:

$$Z(@t = \tau_c) = Z_0 e^{\left(-\frac{\tau_c}{\tau_c}\right)} = \frac{Z_0}{e} \qquad (66)$$

where *Z(t)* is the position of the surface during creep and Z_0 is the initial indentation depth. The difference between this value and the initial indentation can be expressed as:

$$\Delta Z(@t=\tau_c)=Z_0-Z(@t=\tau_c)=Z_0\left(1-\frac{1}{e}\right) \qquad (67)$$

where ΔZ is the change in indentation between time t = 0 and t = τ_c.

Although previously presented in the viscoelastic theory section within Chapter 2, the solution for creep compliance function using the correspondence principle will be stated once more for ease of reference throughout this section:

$$C_{crp}(t)=C_g+\left(C_r-C_g\right)\left(1-e^{\frac{-t}{\tau_c}}\right) \qquad (68)$$

where: $C_g=\frac{1}{k_{inf}+k_0}$, $C_r=\frac{1}{k_{inf}}$, and $\tau_c=\tau_r\frac{k_{inf}+k_0}{k_{inf}}=\frac{c_d(k_{inf}+k_0)}{k_0k_{inf}}$

where the underscores r and g denote rubbery and glassy modulus, respectively.

As previously mentioned, this solution for the creep compliance is under the assumption of constant load, which is not exactly the case in the actual numerical creep. Nevertheless, this equation provides a good enough solution because the times during creep are significantly shorter and only the initial portion of the creep relaxation curve is used to extract the retardation time.

In order to solve for the Retardation Time, the variables in Figure 25 are used along with the definition of the Retardation Time in equations (66) and (67) to form the following derivation to extract τ_c.

From Figure 25:

$$\Delta t=t_2-t_1 \qquad (69)$$

$$\Delta z=Z_1-Z_1' \qquad (70)$$

$$\Delta z_{creep}=Z_2-Z_1' \qquad (71)$$

If the surface moves Δz_{creep} during a time interval of Δt and using equation (67):

$$\Delta z_{creep} = \Delta z\left(1 - e^{\frac{-\Delta t}{\tau_c}}\right) \tag{72}$$

Solving for τ_c yields:

$$\tau_c = -\frac{\Delta t}{ln\left(1 - \frac{\Delta z_{creep}}{\Delta z}\right)} \tag{73}$$

The expression in equation (73) now allows the Retardation Time to be calculated if only the three positions Z_1, Z_1', and Z_2 are known along with the time lapse between taps Δt.

The question then arises, how does one know the positions of the surface at those instances in time? The answer comes by examining the force versus distance curve at the point of transition between contact and non-contact, a_0. According to Figure 3, the transition occurs at the distance where the minimum attractive force is measured. This minimum is used as the indicator of where the surface is located. If it is assumed that the tip makes (and conversely breaks) contact at these minimum force "wells," then the position of the surface (Z_1' and Z_2) can be approximated as the tip position measured at these times (t_1 and t_2) along the trajectory. The only remaining measureable variable to be determined is absolute zero reference for the surface. This variable can be approximated by measuring the position of the tip at the very first minimum force well encountered as the cantilever base is lowered to make initial contact with the surface.

Therefore, using the position, force, and time data output by the AFM, the Retardation Time (τ_c) can be calculated for surface creep between taps. The critical parameter in determining these distances is the position and time at which the force is in the minimum well (a_0) at the transition point between interaction regimes.

3.3.2 Acquiring the Total Sample Compliance/Stiffness (Stage 1b)

The next step in the VETICA method is acquiring the glassy stiffness of the system. In this part of the method, focus is shifted from the non-contact regime to the contact regime. As a result, the stress relaxation of the glassy stiffness is defined as the inverse of the glassy compliance given in (68):

$$K_g = \frac{1}{C_g} = k_{inf} + k_0 \tag{74}$$

From the theory of linear viscoelasticity, the glassy stiffness is equated as the initial stiffness before any relaxation occurs. In the physical sense, this stiffness is the initial slope of the force versus distance curve after contact is made between tip and sample. Using a basic dimensional analysis approach, the slope of this curve would yield a stiffness with units [Force/distance] (giving [N/m], the expected unit for spring constants).

The sensitivity of this part of the VETICA method emerges from the number of data points used to calculate the slope. Too few data points may not be sufficient enough to fit a linear line, but too many points could result in a convolution of the glassy stiffness with a partially relaxed stiffness. More specifically, the convolution of the glassy and relaxed stiffness would become more severe as viscosity decreases and dissipation increases.

3.3.3 SLS Parameter Extraction and Optimization (Stage 2)

The second phase of the VETICA method is called Stage 2 where the variables that are extracted from this stage of the process are the three material properties that constitute the SLS. Stage 2 involves using a least-squares, non-linear data-fitting optimization tool in MATLAB employing the predefined function `lsqnonlin` using the default trust-region-reflective optimization algorithm [93, 94]. The optimization tool operates by taking two known signals, input and output, and uses the input to compute a second output from a user defined function. The second output is compared to the known output and a minimization is made based on the residuals between the two signals. In the case of the VETICA method, the input signal is the position data of the tip within the contact region of the oscillation and F_{ts} and the resulting relaxation force are the known and optimized outputs respectively, from which the SLS conditions are extracted. The relaxation force is calculated by first compiling the stress relaxation function which can be re-written from equation (43) as:

$$E_{rel}(t) = K_r + \left(K_g - K_r\right) \exp\left(\frac{-t}{\tau_r}\right) \tag{75}$$

where: $K_r = k_{inf}, K_g = k_{inf} + k_0$, and $\tau_r \equiv \frac{c_d}{k_0}$

From Stage 1a and Stage 1b, the variables τ_c and K_g are extracted from the signal data. The Retardation Time (τ_c) can be converted to the Relaxation Time (τ_r) of the stress relaxation equation in the following way:

$$\tau_r = \tau_c \frac{k_{inf}}{k_{inf} + k_0} = \tau_c \frac{K_r}{K_g} \tag{76}$$

In order to convert the Retardation to a Relaxation time, one unknown variable remains that must be solved for: the rubbery modulus of the fully relaxed material (K_r). To acquire this final characteristic material constant, the lsqnonlin function in MATLAB for non-linear fitting takes equation (76) and extracts a value for K_r by minimizing the residual vector between F_{ts} and the following:

$$F_{SLS}(t) = E_{rel}(t)z_{tip}(t) = \left(K_r + \left(K_g - K_r\right)\exp\left(\frac{-t}{\tau_r}\right)\right)z_{tip}(t) \qquad (77)$$

Or, expressed in terms of known characteristic material constants up until this point:

$$F_{SLS}(t) = \left(K_r + \left(K_g - K_r\right)\exp\left(\frac{-tK_g}{\tau_c K_r}\right)\right)z_{tip}(t) \qquad (78)$$

where F_{SLS} is the calculated force from the defined E_{rel} function with one unknown K_r, and z_{tip} is the position of the tip during contact, which is assumed to be equal to the position of the surface during stress relaxation. As a result of the correspondence principle, z_{tip} must be fitted with an analytical expression that can be inverted from the Laplace domain. The optimization problem then follows the form:

$$\min_{t} \|f(t)\|_2^2 \qquad (79)$$

where: $$f(t) = F_{ts}(t) - F_{SLS}(t) \qquad (80)$$

$f(t)$ is a vector of the force residuals for all points acquired in time *t* during the contact portion of the tap. The main constraints governing the accuracy of the optimization are the initial guess of K_r and the upper and lower bounds for the unknown variable K_r. The upper and lower bounds are not expected to be sensitive for the range of equilibrium stiffness, and results on the sensitivity of the initial guess are presented in Chapter 4.

The final step of the VETICA method is to convert the characteristic material constants τ_r, K_g, and K_r to the material properties c_d, k_0, and k_{inf} of the linear viscoelastic SLS model. The characteristic constants can be converted to the properties in the following forms:

$$\boldsymbol{k_{inf} = K_r} \qquad (81)$$

$$K_g = k_{inf} + k_0 \rightarrow \boldsymbol{k_0 = K_g - k_{inf}} \tag{82}$$

$$\tau_r = \frac{c_d}{k_0} \rightarrow \boldsymbol{c_d = \tau_r k_0} \tag{83}$$

By acquiring the three discrete elements of the SLS, the VETICA method has displayed a means to extract material properties of a surface being scanned in IC-AFM under the assumption that the surface is linear viscoelastic. The following chapter analyzes features of the method, the accuracy of the method, and the extent to which the model can be used to recover material properties.

Chapter 4: Results and Analysis

4.1 Recapitulation of Objectives

The objectives of this thesis are to formulate and develop a method to extract linear viscoelastic material properties in IC-AFM using AFM signal data. This chapter consists of results obtained using the THC and SLS simulation techniques discussed in the previous chapters. The VETICA method is then implemented for a series of parametric simulations and the extent under which the model retains accuracy is discussed. Table 1 displays the parameters and ranges of the surface and AFM system explored in conducting the parametric study. Finally, the chapter concludes by relating the extracted extensive material properties of the SLS (stiffness and damping) to intensive "real sample" material properties such as moduli and viscosity.

Table 1. Set of Surface and AFM and THC Probe parameters used to evaluate the VETICA method.

Surface Properties	Ranges Simulated	Units
Dashpot Value (c_d)	$1\text{x}10^{-5}$ - $1\text{x}10^{3}$	[kg/s]
Stiffness Ratio (k_0:k_{inf})	1:8 - 32:1	[N/A]
AFM and THC Properties		
Amplitude Set point	25 - 80	[% of Free Oscillation Amplitude]
Free Amplitude	100	[nm]
Probe Stiffness (k_1/k_2)	1-10/ 70 - 700	[N/m]
Resonant Frequency (ω_{n1}/ ω_{n2})	10 - 100/ 150 - 1500	[kHz]
Instrument Print Step Resolution (PS)	0.125 - 8	[ns]

4.2 THC and SLS Implementation

4.2.1 Tip-Sample Interaction

The tip-sample interaction is the combination of two interacting dynamics between the numerically computed THC and the SLS. After THC and SLS are integrated using the methods presented Chapter 3, the resulting tip sample interaction force versus tip to sample distance can be seen in Figure 28.

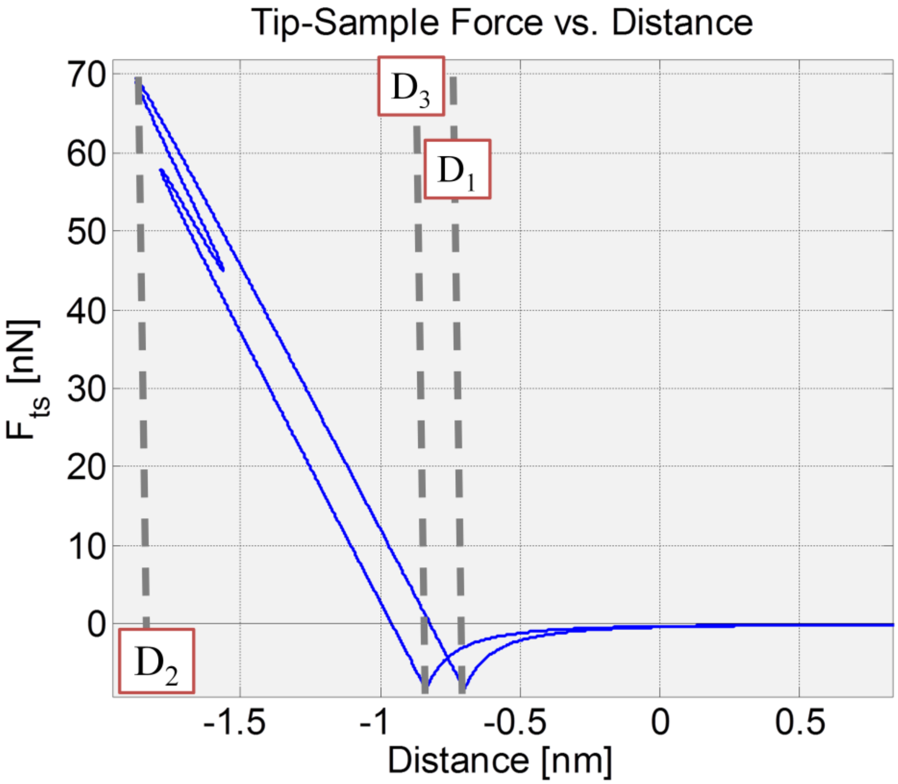

Figure 28. Tip-sample interaction force F_{ts} versus distance between tip and sample. D_1 is the distance at which contact occurs and penetration begins, D_2 is distance at which the peak force is achieved and retract begins, and D_3 distance at which separation occurs. The contact and separation appears to occur "below" the surface because the force curve is taken in the "Steady State Zero Reference Equilibrium" regime (see Figure 26). The system simulated to produce this force curve has ω_{n1} = 50 kHz, ω_{n2} = 750 kHz, k_1 = 10 N/m, k_2 = 700 N/m, $A_{setpoint}$ = 70 nm, Print Step (PS) = 0. 5 ns, k_{inf} = 4 [N/m], k_0 = 64 [N/m], and c_d = 5x10^{-4} [kg/s].

As is expected the governing equations (58) and (65) for the force, F_{ts} is near zero far from the surface and begins to become more negative as the tip approaches the surface and van der Waals forces increase. At distance D_1, the tip enters the repulsive regime and continues penetration until D_2. The tip then begins to retract until it breaks free from the surface at D_3. In this example, the hysteresis that occurs from surface viscoelasticity causes a shift in the minimum F_{ts} transition point a_0 which is why $D_1 \neq D_2$ (i.e., the surface is not at the same position when contact and separation occur). In order to identify the contributions of viscoelastic hysteresis to the dissipation, one must consider a method to calculate the dissipation.

Quantitatively, the dissipation experienced per oscillation cycle (E_{diss}) is the area inside of the force curve loop and, in this particular example, is equal to approximately 45.9 eV. Due to the dissipation is the area contained in the loop of the curve, the number and intensity within a force curve of these "multi-peaks" should be investigated to determine their influence on dissipation experienced per oscillation cycle. The term "multi-peak" is introduced to describe the two force maxima observed in the force curve of the THC.

The following analysis discusses the possibility of increasing the number of these multi-peaks observed in a single tap. If F_{ts} is large enough to excite the paddle with sufficient amplitude, multiple oscillations will occur while remaining in contact with the surface. Although the number of peaks should increase with larger multiples of separation between the resonant frequencies of the paddle and cantilever, the increase of resonant frequency yields tradeoffs of increased paddle stiffness and/or a decrease in the paddle mass which do not allow for these peaks to be present. In a case where mass is held constant, increasing the resonant frequency of the paddle would yield a stiffer paddle proportional by a power of two ($k = m\omega_n^2$), and in turn, smaller amplitudes. If another case were considered where the stiffness of the paddle is held constant, the mass would be proportional to the resonant frequency by a power of one half. In both cases it would be expected that the peaks would decrease and vanish as the resonant frequency increases. The F_{ts} versus distance of two described scenarios are presented in Figure 29. Furthermore, by increasing the distance between paddle and cantilever resonant frequency, the higher harmonic amplitudes that are enhanced by the torsional excitation would also decrease and might not be measureable above the noise floor.

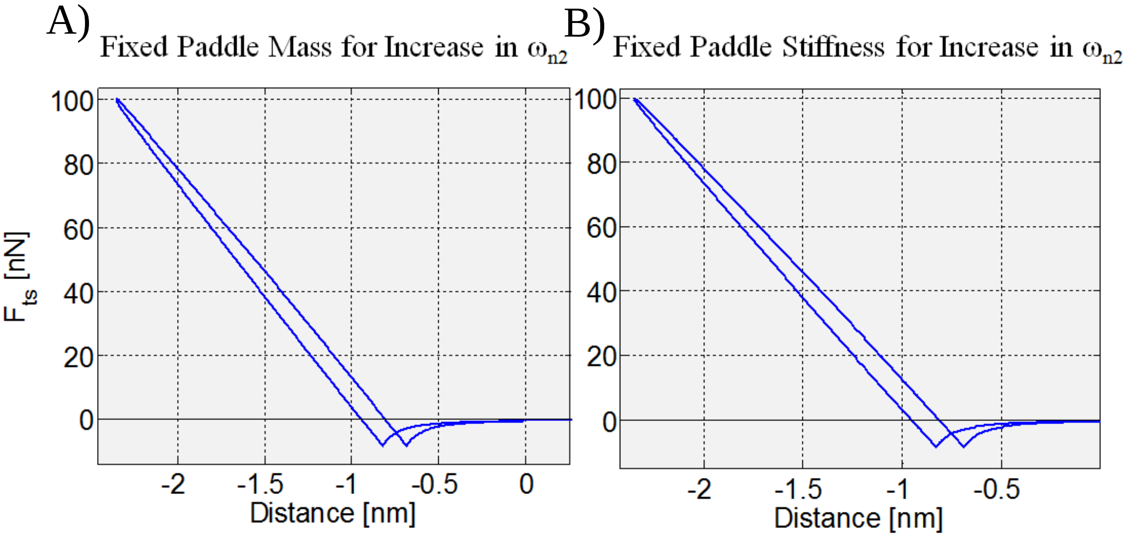

Figure 29. System of Figure 28 except resonant frequency of the paddle ω_{n2} = 1500 kHz (2x more). A) The mass of the paddle is held constant as ω_{n2} increases and as paddle stiffness increases to k_2 = 2800 N/m (from 700 N/m). B) The stiffness of the paddle is held constant as ω_{n2} increases and as paddle mass decreases to m_2 = 0.31 ng (from 1.24 ng). E_{diss} for A) and B) are approximately 61.4 and 59.2 eV, respectively.

Notice that in both force curves, the double peak from Figure 28 has been replaced by a single peak for the following reasons: 1) in Figure 29A, the amplitude of paddle has decreased due to high stiffness (and less sensitivity), and 2) in Figure

29B the decrease in mass of the paddle causes a decrease in the kinetic energy of the mass and prevents it from penetrating the surface. Regardless of how the paddle effect on the force curve attenuates during the contact interaction, in both cases the dissipated energy increased from the case where the "double tap" was observed with a lower resonant frequency paddle in Figure 28.

Regarding the intensity of the peaks, the dynamics of the paddle is the influential factor in determining how prominent the peaks appear in the curve. The most logical way to enhance the effects of the paddle trajectory is to vary the nominal spring stiffness. The stiffness of the paddle will affect the sensitivity of the paddle to F_{ts} and how easily it can deflect the surface multiple times within a tap. Figure 30 displays the effects of varying paddle stiffness on energy dissipated per cycle while holding all other system parameters the same as in Figure 28. All force curves from the data in Figure 30 qualitatively displayed the multi-peak features seen in Figure 28.

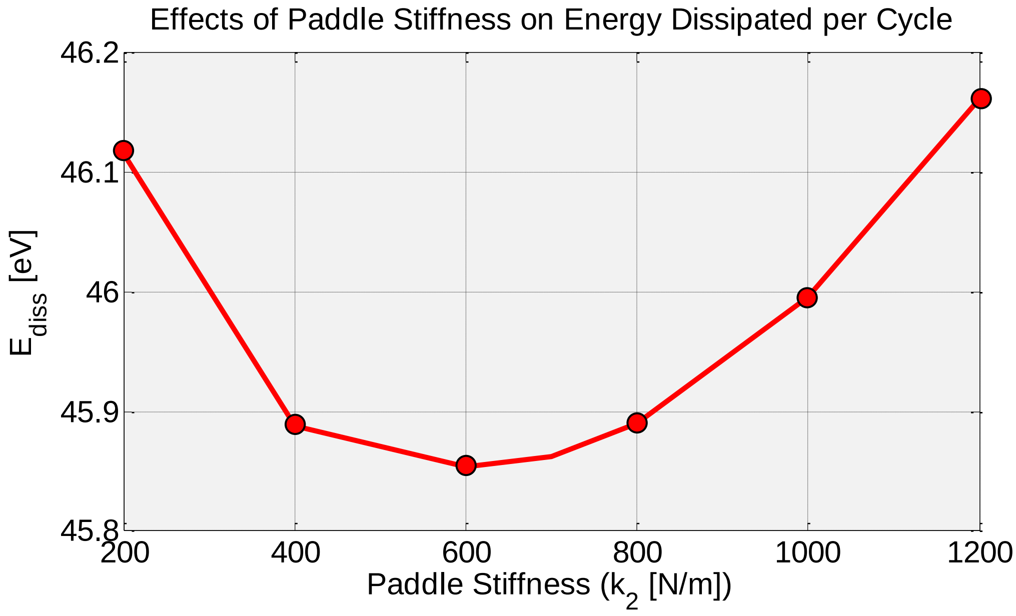

Figure 30. The effect of paddle stiffness on energy dissipated per cycle. The system is the same as that of Figure 28 with the exception that the paddle stiffness, k_2, is varied from 200-1200 [N/m].

It is clear from Figure 30 that the dissipated energy reaches a minimum value at 600 N/m. When the nature of spring stiffness is considered, this observation will become clearer. If the spring is very soft (in the case of 200 N/m), it will not have the potential energy necessary to cause large deformation to the surface during a tap and the system will converge to a single peak. Conversely, if the tip is too stiff (in the case of 1200 N/m), the tip-sample force F_{ts} may not be large enough, based on the overall depth of penetration governed by the flexural cantilever, to excite the paddle where it can oscillate at a large amplitude. Again, the system would converge to a single peak where more dissipation is observed. Moreover, because the response of the paddle is governed by the Fourier spectrum of F_{ts}, which is coupled in the cantilever dynamics with the flexural cantilever, the effect of the higher harmonics of the cantilever will also affect the amplitude of the paddle, and therefore the intensity of the multi-peak in the force curve. All the same, the conclusion is that there is a range of paddle stiffness in which the dissipation exhibited from the surface is attenuated. This observation is a critical consideration for users of the THC where dissipation is usually attributed to a phase shift in the signal. This observation is not unique to the THC, but rather any multifrequency AFM application where these multi-taps possibly occur. In conclusion on the effects of the THC and SLS on the tip-sample interaction, the dissipated energy per cycle can vary and contains a minimum with the variation of paddle stiffness, and this energy dissipation can increase with higher resonant frequency paddles.

4.2.2 Inclusion of van der Waals forces

While in the creep phase of the tapping motion, the SLS is subject to a van der Waals force pulling it towards the surface. Although van der Waals force does effect the position of the SLS near the contact and separation transition points of the tapping motion (Figure 31), the magnitude is not strong enough to effect a noticeable position change in the surface which would yield inaccurate VETICA results (Hamaker constant = $0.2\text{x}10^{-18}$ J for all simulations).

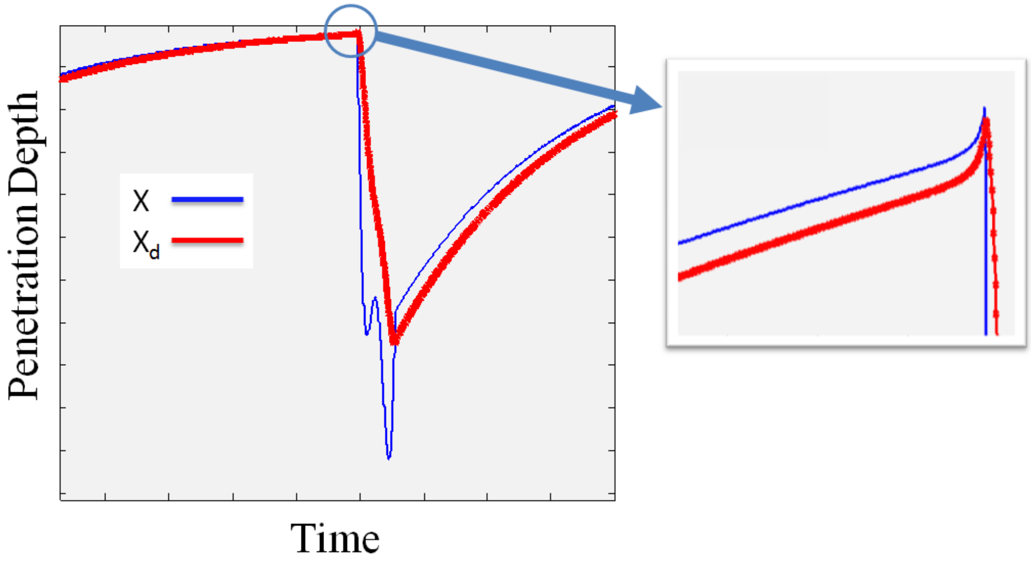

Figure 31. The effect of van der Waals force on SLS position where the blue line is the position of the surface *X* and the red line is dashpot coordinate X_d.

The negligible change in SLS position in reaction to applied van der Waals force is due to two main factors: 1) the choice of stiffness chosen for the SLS spring k_{inf} and k_0 cause a resistive spring force which is relatively much larger than the contributions of van der Waals (e.g., tens to hundreds of nN from the surface spring force compared to less than 10 nN peak force from van der Waals) and 2) the van der Waals force approaches larger magnitudes for only a short period of time due to the high velocity of the incoming and departing tip near the transition point (e.g., approximately 1 cm/s near the transition point). In summary, van der Waals is included to act on the surface for the sake of physical consistency, but has little effect on the accuracy of the VETICA method because of high sample stiffness and high velocities near the transition point.

4.3 VETICA Analysis

The remainder of the results for this thesis will be analyzing the VETICA method. The first part of the results will be detailing the VETICA process through a comprehensive example problem from Stage 1 to Stage 2. A parametric examination of the method is presented where surface characteristics of the SLS and AFM system controllable parameters are analyzed to determine the range of materials under which the VETICA method is accurate and which controllable features of the AFM can be used to shift and manipulate this range. Results are then presented to relate the VETICA method to current experimental concerns and an approximation is made to determine which known viscoelastic materials the VETICA method could be applied to extract material properties.

4.3.1 Acquiring the Retardation Time Constant τ_c (Stage 1a)

From the earlier presentation of the VETICA process, the initial step called Stage 1a involves examining the transition points of the non-contact regime of the IC-AFM interaction. Figure 32 shows how the contact and separation transition points from the tip-sample interaction force (F_{ts}) are used to find the approximated surface position. The time t_0 corresponds to a minimum in F_{ts} where the transition between interaction regimes occurs. That same time also corresponds to a tip position (denoted as a_0 earlier), which is assumed to be coinciding with the surface position at t_0.

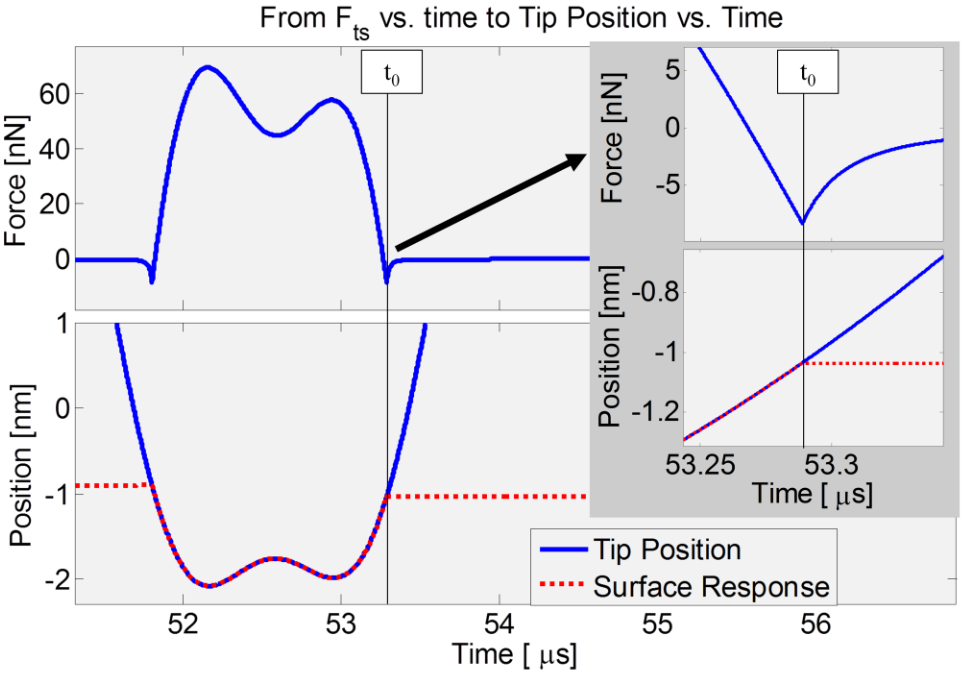

Figure 32. The conversion from tip-sample interaction force (F_{ts}) in the time domain to tip trajectory in the time domain. At t_0, the transition from contact to non-contact regime occurs and the tip position at the time is assumed to be the surface position. Results are for a system with ω_{n1} = 50 kHz, ω_{n2} = 750 kHz, k_1 = 10 N/m, k_2 = 700 N/m, $A_{setpoint}$ = 70 nm, PS = 0.125 ns, k_{inf} = 4 N/m, k_0 = 128 N/m, and c_d = 4x10^{-4} kg/s.

Using the approach of acquiring the position demonstrated in Figure 32, the initial and final positions and times of the surface creep are found by using the separation point of one tap as the initial, and the contact of the next future tap as the final. Figure 33 shows the surface creeps between taps for a simulation and marks the times and positions for the two points necessary to compute Δz_{creep} found in equation (73). The system configuration used to simulate the results in Figure 33 will be used as the example for the remaining steps of the VETICA process presented in this section. The initial zero reference contact point for all the simulations (Z_1 from equation (70)) is the original transition point before any taps have occurred where:

$$Z_1 = a_{01} = 0.2 \text{ nm} \tag{84}$$

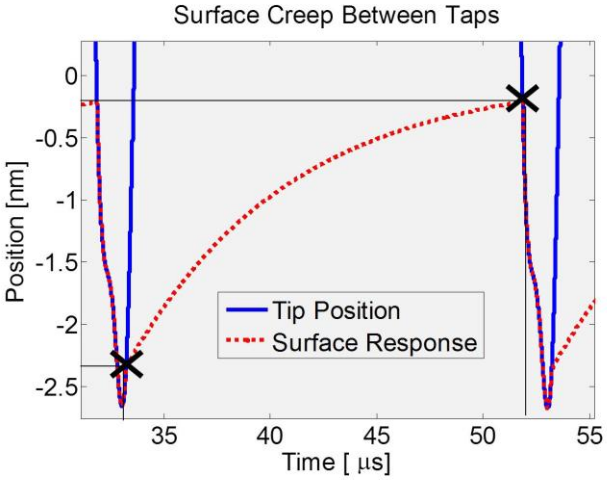

Figure 33. Surface Creep in the non-contact period between taps. The blue line is the position of the tip, the red dashed line is the surface positions, and the black x's show the transition points where contact and non-contact occur. Results are for a system with ω_{n1} = 50 kHz, ω_{n2} = 750 kHz, k_1 = 10 N/m, k_2 = 700 N/m, $A_{setpoint}$ = 70 nm, PS = 0.125 ns, k_{inf} = 4 [N/m], and k_0 = 128 [N/m], and c_d = 3x10^{-5} kg/s.

In order to validate that the surface data from the simulated SLS would provide the theoretical compliance τ_c given from equation (68), a curve fit using the analytical exponential form of τ_c from equation (66) is used to fit the creep data and is shown in Figure 34.

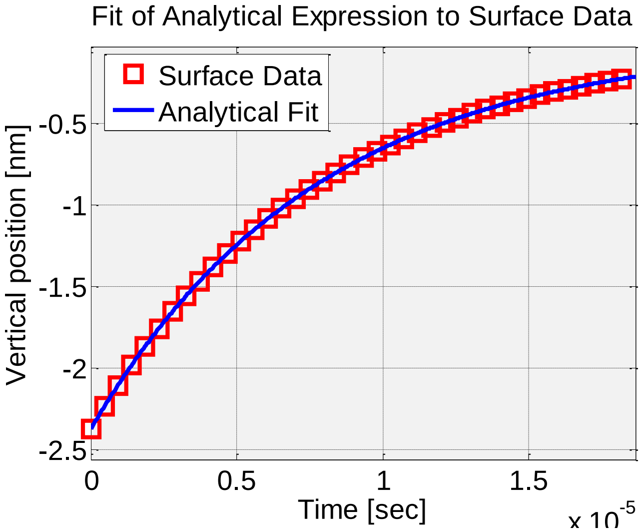

Figure 34. Analytical fit (blue line) of creep response to surface data (red squares). System is the same one used in Figure 33.

The analytical fit function follows the form of:

$$\beta e^{-t/\tau_{c\,fit}} \tag{85}$$

and the fitted values for the example are:

$$\beta = -2.375$$

and

$$\tau_{c\,fit} = 7.7334 \times 10^{-6}$$

with the goodness-of-fit (gof) values of RMSE = $1.0679\text{x}10^{-13}$ and R^2 =1. The analytical fit gave accurate results with as few as 10 points and could recover the retardation time constant with fewer than 10 ns of creep versus. time data. This fit accuracy demonstrates that the specific solution to the differential equation of the SLS where stress is considered a unit step function is a valid approximation. The values and errors of the theoretical and analytical fit VETICA method retardation time constants for the given example can be seen in Table 2.

Table 2. Table of fitted and VETICA results of τ_c for system in Figure 33.

τ_c Theory	τ_c Analytical Fit	τ_c Analytical Fit Error [%]	τ_c VETICA	τ_c VETICA Error [%]
7.7344E-06	7.7334E-06	0.01	7.6152E-06	1.54

The error for the retardation time increases significantly from the analytical fit to the result of the VETICA method. This increase in error is due to the consequence that the VETICA method does not actually know the position of the surface but instead approximates it based on the tip position. The low error from the VETICA method demonstrates the ability to use AFM position, force, and time data to extract the retardation time.

4.3.2 Acquiring the Glassy Stiffness (Stage 1b)

Stage 1b of the VETICA process involves acquiring the glassy stiffness K_g from the stress relaxation portion of the oscillation during contact. This variable is extracted by calculating the initial slope (force/distance) of the F_{ts} versus tip position curve and the fit is shown in Figure 35.

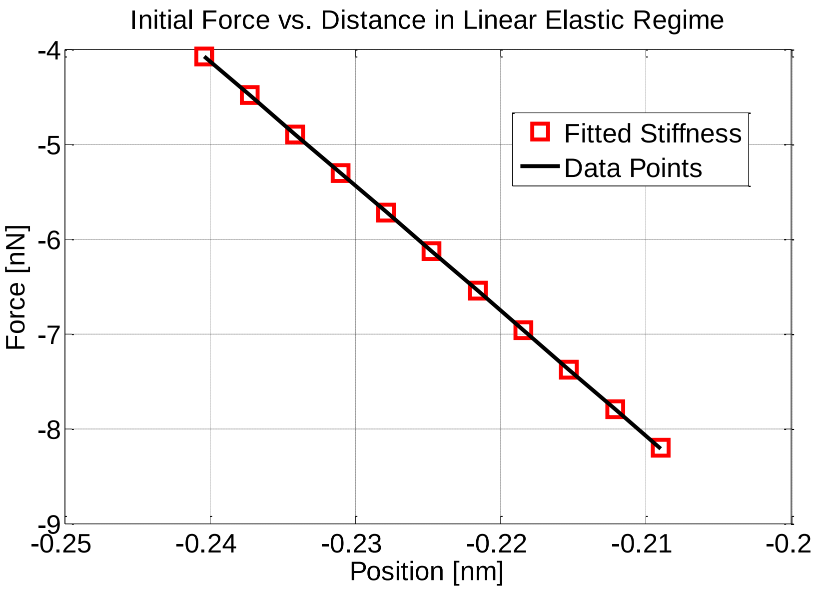

Figure 35. Initial force versus distance curve for determining K_g.

The analytical fit function follows the form of:

$$\alpha z + \gamma \tag{86}$$

and the fitted values for the example are:

$$\alpha = 131.79$$

and

$$\gamma = -35.752$$

with fitting values of RMSE = 2.51 x10^{-3} and R^2 =1. In order to determine the effects of the fit technique, the number of points taken after contact to perform the fit is explored in Figure 36. Although the fit becomes more accurate as more points are taken, when dissipation is present, the slope of the line begins to decrease as contact time increases. For this reason, it is ideal in the VETICA method to take fewer points after the force curve in order to get the initial slope to prevent inaccuracies. For the rest of the simulations presented in this thesis, ten points after contact are taken from the force curve to compute K_g. This selection of points provided consistently accurate values of K_g across all simulation conditions.

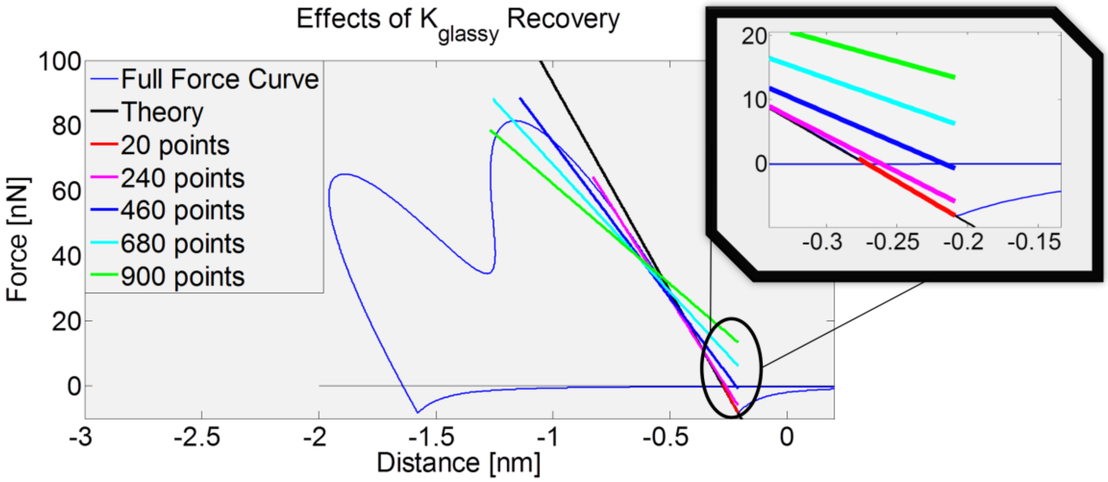

Figure 36. The relationship between the number of points used in K_g recovery technique. The colored lines are the linear fit applied for various lengths of data points used.

Table 3 shows the VETICA results for fitting the glassy stiffness using the current example conditions. The table shows that the resulting fit from the initial force curve is very accurate. The fit is taken during the "Steady State Zero Reference

Equilibrium" regime (see Figure 26) where the sample has not equilibrated back to original undeformed position and the k_0 spring in particular is exhibiting a negative balancing force to the elastic spring in creep just before contact. The stiffness transitions between non-contact and contact regimes could cause the small error in the Table 3. Additionally, the number of points could also be the cause of the error as previously investigated. In summary, the extracted value of K_g in this example shows that the VETICA method Stage 1b can collect the glassy stiffness with minimal error using the initial slope of the force curve.

Table 3. Table of Fitted and VETICA results of K_g for system in Figure 33.

K_g Theory	K_g VETICA	K_g VETICA Error [%]
132.00	131.79	0.16

4.3.3 Acquiring the SLS Parameters (Stage 2)

Stage 2 of the VETICA method is implemented to conclude the example demonstrating the feasibility of the method. The first part of the process requires that the tip position data during the contact regime be fit with an analytical expression. The expression must be capable of being transformed to the Laplace domain in order to utilize the correspondence principle used to calculate the stress relaxation function.

Figure 37 displays the tip trajectory data of the example and initial fits using polynomials and summation series of sine functions which possess the following analytical forms, respectively:

$$z_{poly}(t) = p_0 + p_1 t + \cdots + p_n t^n \tag{87}$$

where n is the order of the polynomial fit, and:

$$z_{sum\ sines}(t) = \sum_{i=1}^{n} a_i \sin(b_i t + c_i) \qquad (88)$$

where n is the order of the sum of sines fit. These two types of functions were chosen because they easily capture the sinusoidal feature of the tip trajectory during contact. A third- and fourth-order polynomial and a first- and third-order sum of sine functions were tested and higher order functions of both are found to be the best approximation for the surface.

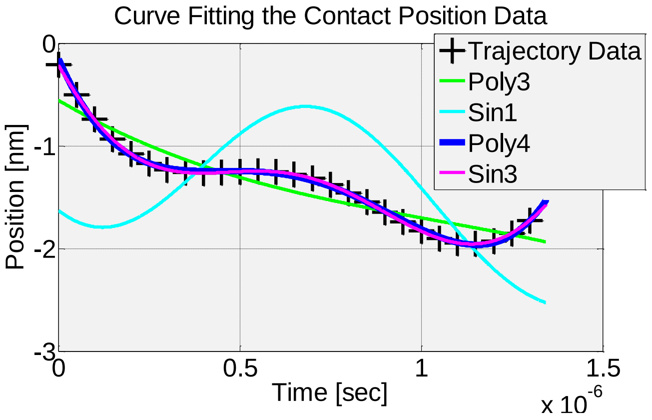

Figure 37. Fitting the THC trajectory data during the contact regime of the tap. The tip trajectory (black crosses) is fit using a third (green) and fourth (blue) order polynomial as well as a first (cyan) and third (magenta) order summation of sine function.

Although these fits appear to be sufficiently accurate, the precision of the position detector on AFM is known to be sub-nanometer. As a result, the residuals of the fit to actual position data are displayed in Figure 38 for even higher order fits than that of Figure 37.

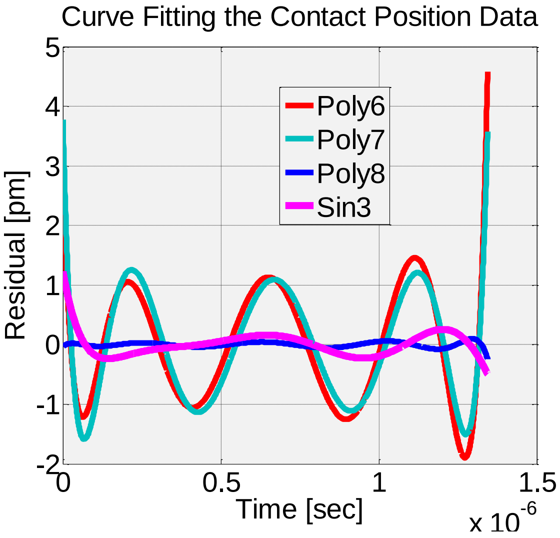

Figure 38. Residuals of higher order fits techniques. The first three fits are polynomial fits of sixth, seventh, and eighth-order (red, green, blue) respectively and the fourth fit is the third-order sin function (magenta) fit for all the data. Note the residual distances are in picometers.

From the residuals of higher order fits, the third order sine function gives a better fit than all polynomial fits less than the eighth-order. The accuracy of the sine wave is expected as the cantilever and tip are known to follow sinusoidal trajectories. Therefore, the third-order sum of sine function is chosen as the analytical fit for the indentation data of the surface in all simulations.

The second part of Stage 2 minimizes the residual between the AFM signal data of known F_{ts} and an analytical force (F_{SLS}) using the non-linear fitting tool in MATLAB to acquire K_r. As previously stated, the initial guess stage of the fitting method must be evaluated for sensitivity. In order to visualize the implication of the initial guess on the analytical F_{SLS}, Figure 39 shows the effects of the initial guess for the rubbery stiffness (K_r) on F_{SLS} before the VETICA optimization occurs.

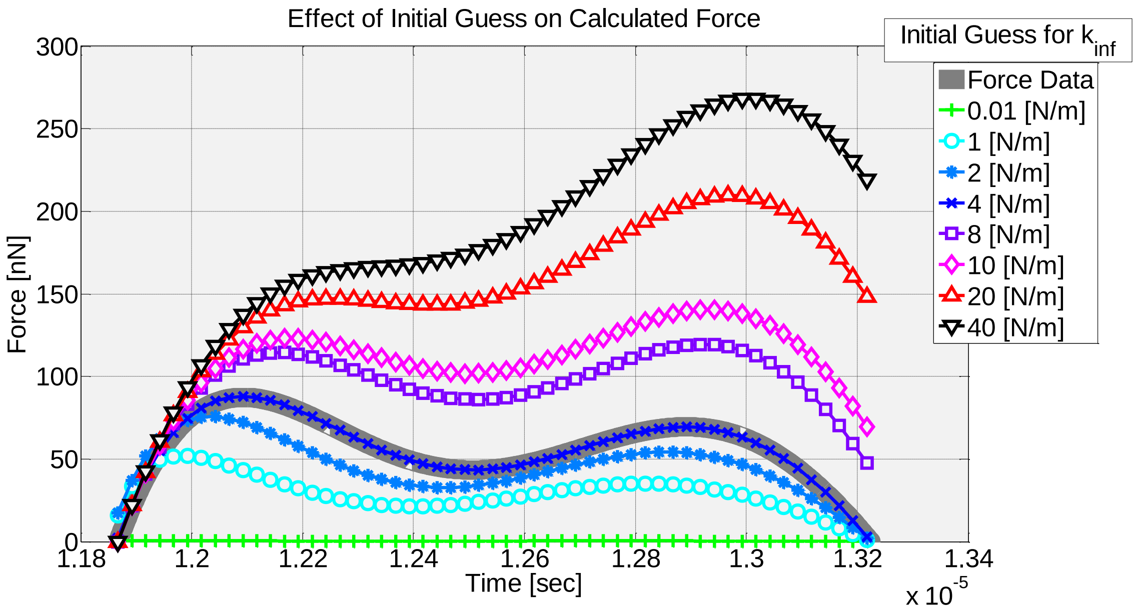

Figure 39. The effect of initial guess on the analytical tip-sample interaction force (F_{SLS}) before optimization. VETICA only requires that the rubbery stiffness (K_r) have an initial guess, hence the analytical force F_{SLS} resulting from changes in K_r are plotted in the various colors and markers.

The data from Figure 39 shows that in addition to the magnitude of the force being affected by the initial guess, the shape of the curve can also generally become distorted as the one side of the curve (right) has a more sensitive response to the initial guess. The sensitivity of the force to changes in initial K_r becomes more severe as time increases because the initial guess not only affects the aggregate stiffness of the material, but also the time constant which alters the exponential coefficient of the stress relaxation equation.

The final F_{SLS} curves are super-positioned over F_{ts} (Figure 40A) in order to understand the resulting effects of the initial guess. Additionally, the root-mean-square error (RMSE) of the residuals between F_{ts} and F_{SLS} are recorded and plotted along iteration number of the optimization tool. In this test, the bounds for initial guess span a range of ten orders of magnitude centered around the actual K_g value to test the sensitivity of the method.

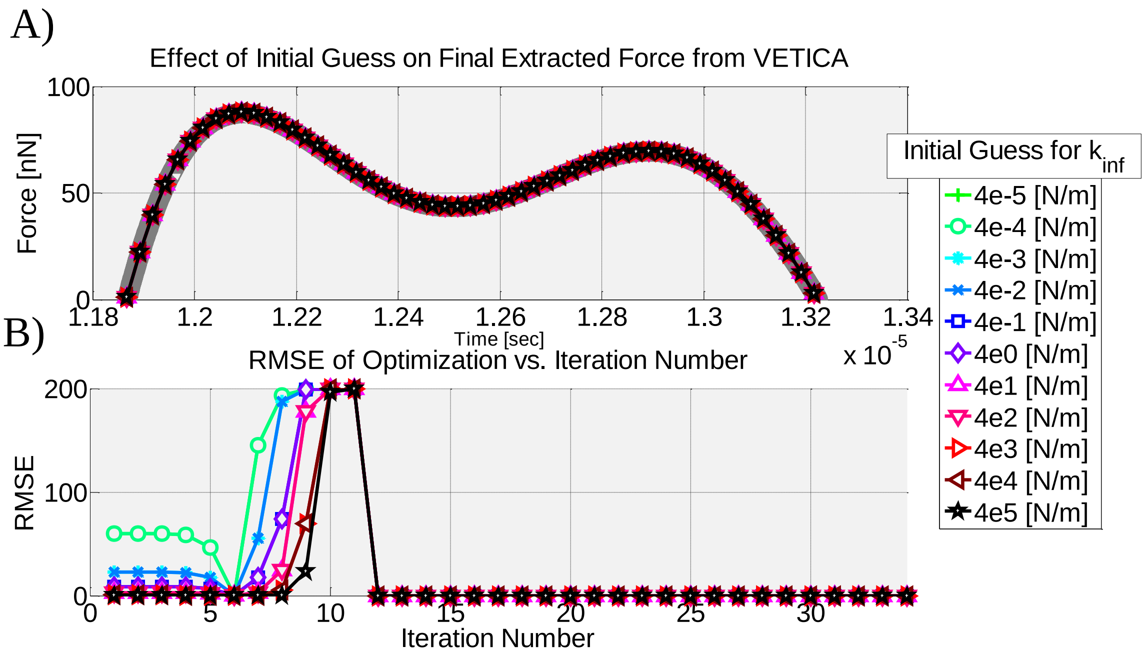

Figure 40. A) Tip-sample interaction force (F_{ts}) after the least-squares non-linear fit optimization function is applied. The legend denotes the initial guesses for k_{inf}. B) The root-mean-square error (RMSE) for the optimization function versus iteration count of the optimization.

In all cases, the optimization converges to a small RMSE and fits to the original F_{ts} data within 15 iterations regardless of initial guess. These results confirm the robustness of the tool in fitting the analytical expression of F_{SLS} to the known AFM signal F_{ts}. Once K_r is calculated, the final part of the VETICA process is converting the characteristic constants of the material to the material properties of the discrete elements.

The final step of the VETICA process is taking the extracted τ_c, K_g, and K_r, and converting them to the material properties of the elements that form the SLS. Table 4 displays the material properties of the SLS extracted through the VETICA process of the example.

Table 4. VETICA results for system in Figure 33.

	SLS Parameters		
	k_0	k_{inf}	c_d
Theory [N/m]	128	4	3.0E-05
VETICA [N/m]	127.91	4.0869	2.99 E-05
Error [%]	0.07	2.17	0.01

Although the average error among SLS parameters for the example problem is small, the errors from the VETICA method show that the material spring stiffness k_0 and k_{inf} do not display the same amount error from the extraction technique. There are several reasons for this difference in error: 1) the ratio of the spring stiffness affects the sensitivity of the relaxation time calculated during contact and therefore loses accuracy on the weaker spring during optimization or 2) the optimization algorithm has difficulty predicting the unknown variable K_r and therefore k_{inf}. The former will be addressed later in this chapter, and latter reason will not be investigated because it is beyond the scope of this work.

In summary, the three material properties are calculated with a low average error in the example presented in this section and it is therefore clear that the VETICA method is capable of extracting linear viscoelastic material properties with low error under the assumption that the surface behaves like a Standard Linear Solid. The assumptions of the VETICA method are sufficient as long as the AFM has high precision for the F_{ts}, tip position and time signals. The next section of the thesis will explore the conditions of both the SLS and AFM which influence the extent under which the VETICA method can be applied.

4.4 Surface Properties

As previously displayed, the VETICA method can be used to extract viscoelastic material properties with little error. However, in order to fully understand the implications of the method, a parametric study across both characteristics of the SLS surface and the AFM must be performed. The method can be placed into context for experimentalists and act as a starting guide for understanding how to manipulate the AFM to best extract surface material properties. The following section will perform a parametric study on the surface properties that affect the accuracy of the VETICA method. Additionally, a parametric study of the surface properties of the SLS will give some insight into the contributions the dissipation from viscoelasticity has on the overall dissipation signal. The two major factors of the surface that influence the dissipation signal are the dashpot (c_d) and the ratio of the elastic springs (k_0:k_{inf}).

The influence of the dashpot is somewhat intuitive because the dashpot is directly related to the relaxation time constant and therefore the exponential term for the time dependent stiffness (E_{rel}). In other words, if the surface is able to relax quicker over the same period of time, then a corresponding larger change in the force, and therefore larger dissipation loop, will be observed. In the case of the stiffness ratio, the influence comes not from the time it takes the stiffness to relax from glassy to rubbery, but rather the change in overall magnitude difference from glassy to rubbery, which corresponds to a larger force difference from initial contact to separation. Figure 41 displays the average dissipated energy per oscillation cycle for the AFM-SLS interactions while the x- and y-axes vary the dashpot and ratio of stiffness. The color map represents the average dissipated power to give a concept of the magnitude, and can be compared to measured dissipative samples in experiment.

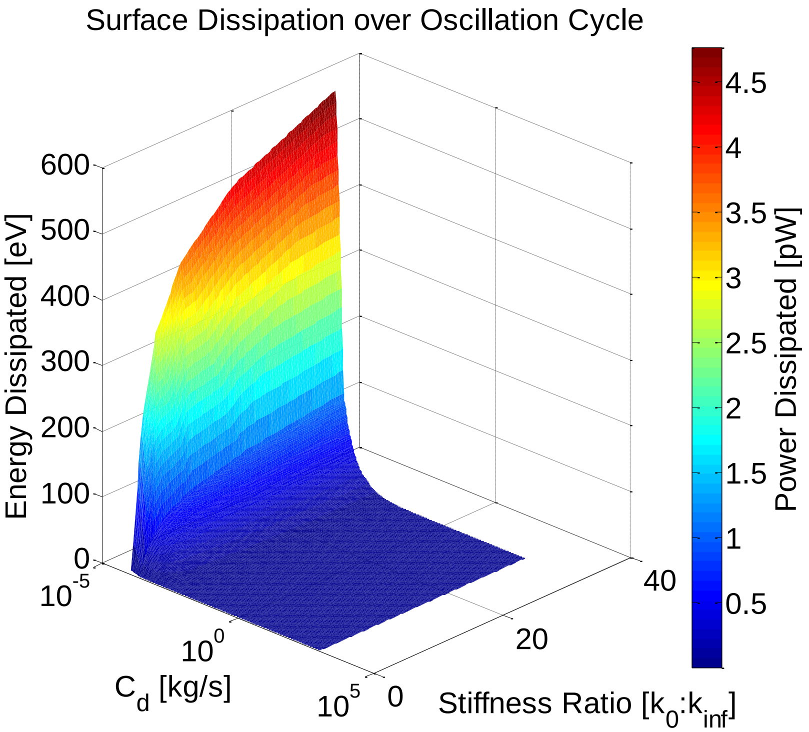

Figure 41. Average dissipation over one oscillation cycle of the THC. The x-y plane comprised of c_d and Stiffness Ratio k_0:k_{inf} are the independent variables that affect the amount of surface viscoelasticity. Energy is plotted along the z-axis and the color represents power (units shown are for comparison).

From Figure 41, it is clear that the dissipated energy is proportional to the ratio of stiffness and inversely proportional to the dashpot. However, at higher dashpot values, the dissipation change from changes in stiffness ratio is no longer observed. Furthermore, the dissipated energy shows a decaying exponential relationship with increase in dashpot, and shows a concave down exponential relationship with an increase in stiffness ratio. To understand the effects of these surface properties, a close examination of the time-dependent stiffness portion of equation (78) can be rewritten in terms of material properties as:

$$K_{total}(t) = k_{inf} + k_0 \exp\left(\frac{-tk_0}{c_d}\right) \tag{89}$$

where $K_{total}(t)$ is the term $E_{rel}(t)$ rewritten in terms of the materials properties of the SLS.

The exponential decay of dissipation with increases in dashpot damping arises because the increase in dashpot value decreases the effect of the exponential factor of equation (89) and relaxation takes a longer time to occur. For the stiffness ratio, the increase in k_0 leading to the increased intensity of the exponential factor of equation (89). Additionally, as $k_0 \gg k_{inf}$ the steepness of the initial slope of the stress relaxation curve (see Figure 12) increases, leading to larger drops in surface stiffness for a give time of contact. As a result, the increase in stiffness ratio (k_0:k_{inf}) leads to greater dissipation in the force versus distance curve.

In summary, both the dashpot value and the ratio of the stiffness can lead to dissipative effects seen in the force curve. While this seems logical from the SLS configuration and governing equations, often AFM surface hysteresis is generalized and attributed to increased viscosity. Therefore, for a linear viscoelastic representation, surface hysteresis is not exclusively linked to viscosity, but the ratio of the internal stiffness could also be an influential factor. In order to make conclusive statements regarding the influence of surface parameters on the VETICA method, the independent driving factors, dashpot and stiffness ratio, are evaluated more completely.

4.4.1 The Effect of Dashpot

The dashpot is one of the most logical sources of viscoelastic dissipation because it is one of the controls for the "effective viscosity" of the SLS surface. As previously stated in Chapter 2, while the value for the dashpot increases, the viscosity component of the surface increases and relaxation/compliance times increase because the surface is resisting relaxation/creep. This section will evaluate the effect the dashpot has on the VETICA method. More specifically, this evaluation will investigate the ranges of damping that the VETICA method is more effective and offer insight into the causes and possible responses for the observed inaccuracies. In all simulations, the dashpot (c_d) was tested on an eight order of magnitude range from $1\text{x}10^{-5}$ to $1\text{x}10^{3}$ kg/s. This specific range of c_d is chosen because the lower extremes compute relaxation times where the surface has the ability to completely creep back to the original position between taps and the upper extremes compute relaxation times where the surface creep is not measurable with current AFM resolution. To show the sensitivity of surface creep to varying values of c_d, Figure 42 displays both a linear and logarithmic distance scale for the creep of the SLS where the dashpot is changed from $4\text{x}10^{-5}$ to $6\text{x}10^{-3}$ kg/s. In all curves, the data was taken at steady state zero reference equilibrium and then normalized to end at a position equal to zero for comparison.

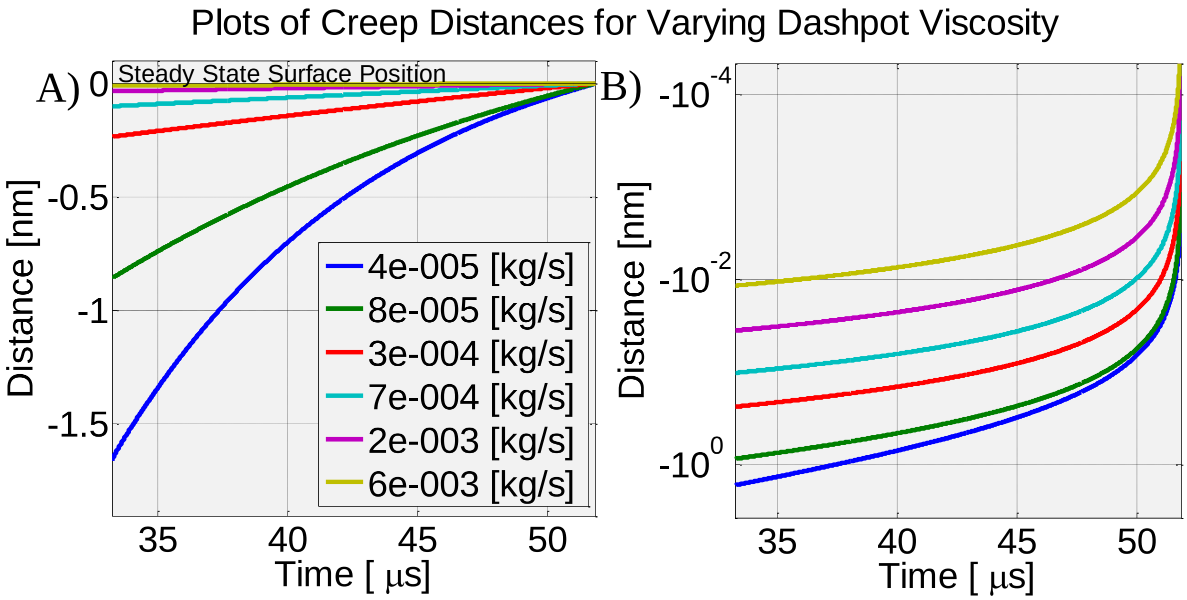

Figure 42. Effect of dashpot (c_d) on creep distances. All curves are recorded in steady state tapping and the steady state zero reference equilibrium positions are normalized to true zero for comparison. A) The linear plot of creep during non-contact phase of tap. B) The logarithmic scale for the distance axis in A).

Although Figure 42 does not encompass the full range of values used in the simulation, the creep distance depended on c_d demonstrates the necessary spatial resolution of the AFM necessary to record creep between taps. In Figure 42B, the creep distances for the highest dashpot value (c_d = 6x10^{-3} kg/s) are on the order of tens of picometers – therefore the upper range of the dashpot values analyzed will be far beyond current AFM spatial resolution limits in IC-AFM. Nevertheless, the data for those values will used in this thesis in order to predict future capabilities of the instrument.

To understand the extent under which the VETICA method is accurate with respect to changing dashpot value, the error of each variable is calculated. Figure 43 displays the ability of the VETICA method to recover the Stage 1 variables (τ_c and K_g) while varying the dashpot value.

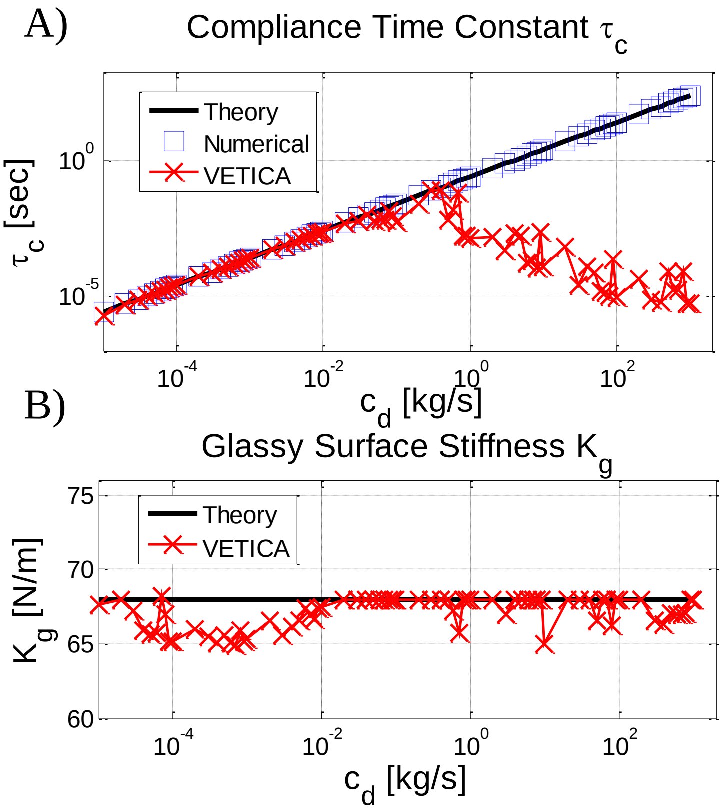

Figure 43. The VETICA method fit for the Stage 1 variables (τ_c and K_g) while adjusting dashpot value. A) The retardation time constant (τ_c) for creep compliance of the surface. The theoretical (black line) values, numerical (blue squares) and VETICA (red x's) results are for a system with ω_{n1} = 50 kHz, ω_{n2} = 750 kHz, k_1 = 10 N/m, k_2 = 700 N/m, $A_{setpoint}$ = 70 nm, PS = 0. 5 ns, and SR = 16:1. B) The Theoretical and VETICA results for the glassy stiffness (K_g) of the surface with same system configuration as A).

According to Figure 43A, it can be seen that when the dashpot value c_d approaches approximately 1x10^{-1} kg/s, the VETICA method begins to diverge away from the theoretical value of the creep retardation time τ_c. However, based on the analysis from Figure 42, the current resolution and imaging conditions of the AFM in IC-AFM extend up to an approximate dashpot value of only 1x10^{-3} kg/s, where the VETICA method still maintains accuracy to theory. Figure 43B shows that the initial contact slope method discussed in Chapter 3 accurately extracts the glassy stiffness value across all magnitudes simulated. Therefore, although the characteristic material constant K_g is accurately captured for all ranges of c_d simulated, the retardation time

τ_c is limited to a specific range of c_d. To simplify the future discussion on results, this specific range of c_d will be referred to as the "acceptance regime." The acceptance regime seen in Figure 44 is the range of simulations for which the extracted value of the creep compliance characteristic retardation time (τ_c) is within reasonable error from the theoretical value.

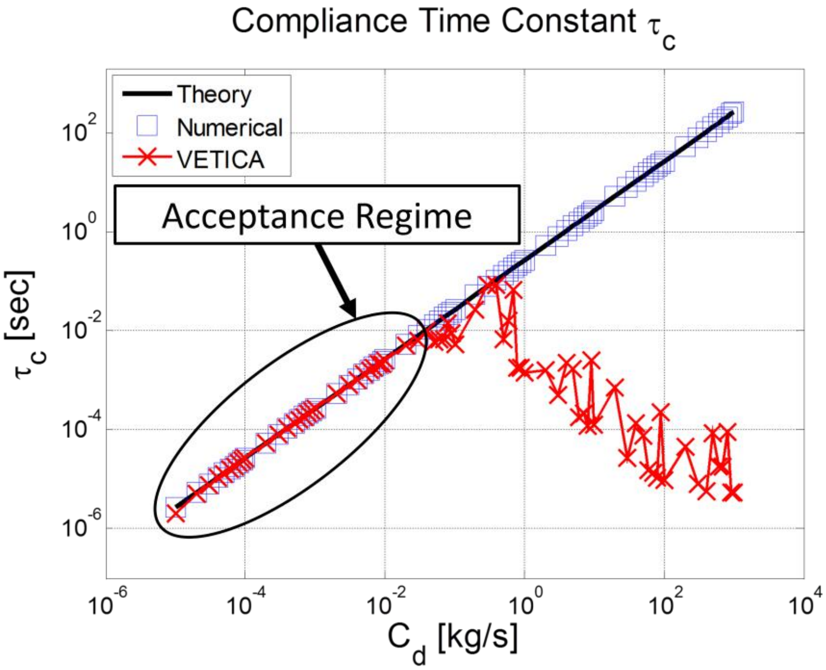

Figure 44. acceptance regime of the extracted data from the VETICA method. The system shown is the same as Figure 43.

In conclusion, the SLS material constant τ_c that is extracted within the acceptance regime is accurate and outside of this regime are erroneous. Despite this limitation, the current resolution capabilities of the AFM are well below where this divergence begins. Additionally, extracting the other material constant K_g is fairly accurate across all values of damping simulated. The next step in understanding the effects of the dashpot is examining the resulting extracted SLS material properties (Stage 2 variables: k_0, k_{inf}, and c_d). Figure 45 give the resulting extracted SLS material properties from the VETICA process as the dashpot is varied.

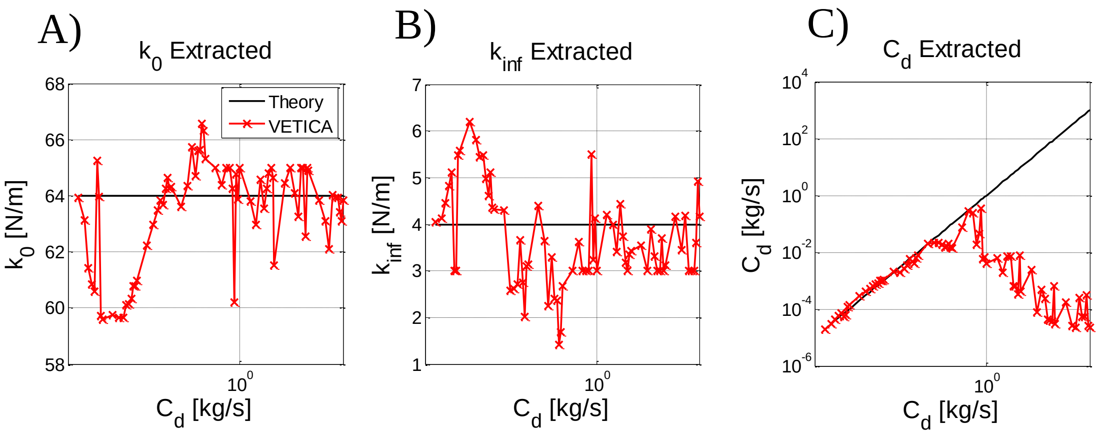

Figure 45. The VETICA method fit for the Stage 2 variables (k_0, k_{inf}, and c_d) while adjusting dashpot value with the same system as Figure 43. Each plot shows the theoretical value (black line) and the extracted value (red x's) from the VETICA method. A) The Maxwell spring (k_0) element which is in series with the dashpot. B) The equilibrium spring (k_{inf}). C) The dashpot element (c_d).

These diagrams show that the stiffness material property k_0 is within ± 4 N/m and k_{inf} is within ± 2 N/m of the actual value across all values of c_d. While this yields a higher computed error for the k_{inf} variable, the value is relative to the magnitude of the stiffness chosen. Therefore, if stiffer values are chosen, the errors would be considerably lower because the precision of the method would not change.

Contrary to the precision of k_0 and k_{inf} across all dashpot values, the extraction of c_d is strongly influenced by the fit result of the retardation time. Therefore, the retardation time and, consequently, the dashpot-extracted value are likely to be the limiting variables in the overall accuracy of the VETICA method. In order to verify this variable dependence quantitatively, Figure 46 displays the errors of both the Stage 1 and Stage 2 variables. Within the acceptance regime, the Stage 1 variables are accurate to less than 10% error although the dashpot and equilibrium stiffness from the Stage 2 variables display errors can approach up to ~55% within the regime. As seen from Figure 45, for values of the dashpot outside of the acceptance regime ($c_d >$

10^{-1} kg/s), the error in the extracted dashpot error increases and is dependent on the retardation time extracted in Figure 44.

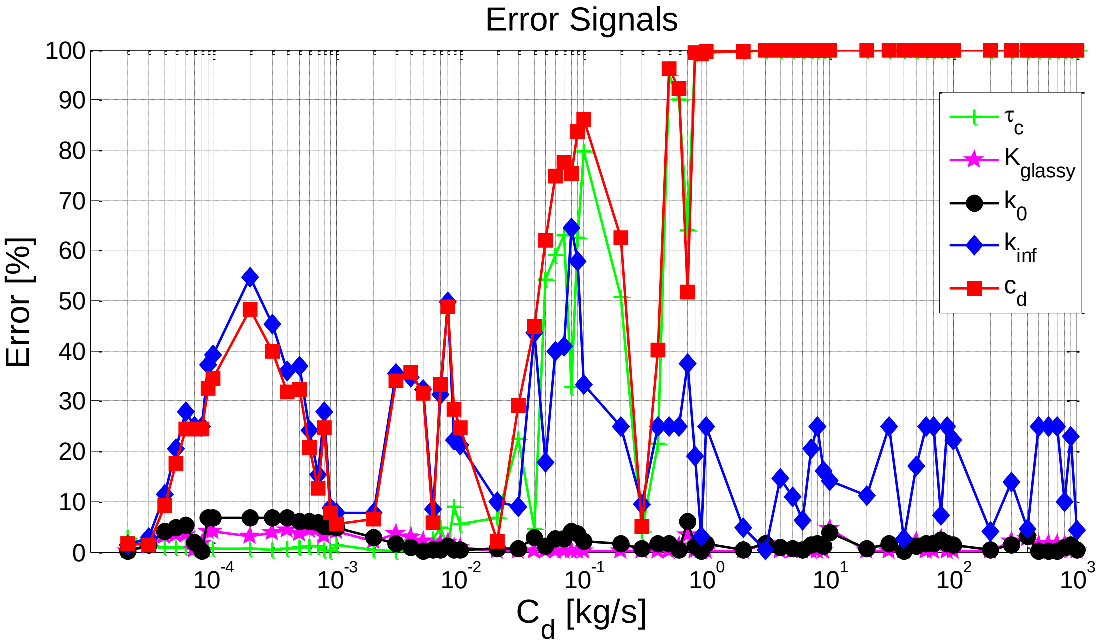

Figure 46. Error Signals for the VETICA method with the same system as Figure 43. The values for the Stage 1 variables (τ_c and K_g) are shown by the green crosses and magenta stars, respectively. The values for the Stage 2 Variables (k_0, k_{inf}, and c_d) are shown by the black circles, blue diamonds, and red squares, respectively.

In conclusion, while the VETICA method shows reasonable accuracy across several orders of magnitude of dashpot values, the critical variable to minimizing the error of the VETICA method is the retardation time constant. Furthermore, the retardation time is limited within an acceptance regime of dashpot values where beyond which, the VETICA method diverges rapidly from theory and material properties are not longer accurately extracted. Although the dashpot has been analyzed and relationships between surface damping and the accuracy of the method have been made, the ratio of the spring stiffness (k_0:k_{inf}) must now be evaluated in order to comprehensively explore the surface characteristics which contribute to hysteresis.

4.4.2 The Effect of Ratio of Spring Stiffness

As previously stated, the dissipation experienced during the oscillation of a tap appears to be dependent on the ratio of the internal SLS spring stiffness. In the ensuing results and discussion, the ratio of the springs has been varied ranging from k_0:k_{inf} = 1:8 to 32:1, or dimensionally as k_0:k_{inf} = 0.5:4 N/m to 128:4 N/m. This range of stiffness and stiffness ratio was chosen because the THC-SLS interaction produces peak repulsive forces, which are typical to experimental forces observed while operating under similar conditions in IC-AFM. Figure 47 displays the average errors of the Stage 1 and Stage 2 variables while in the acceptance regime of dashpot values. The errors calculated in Figure 47 are averages of extracted values in the full data set and could therefore be slightly overestimating the errors due to peaks from computational approximations.

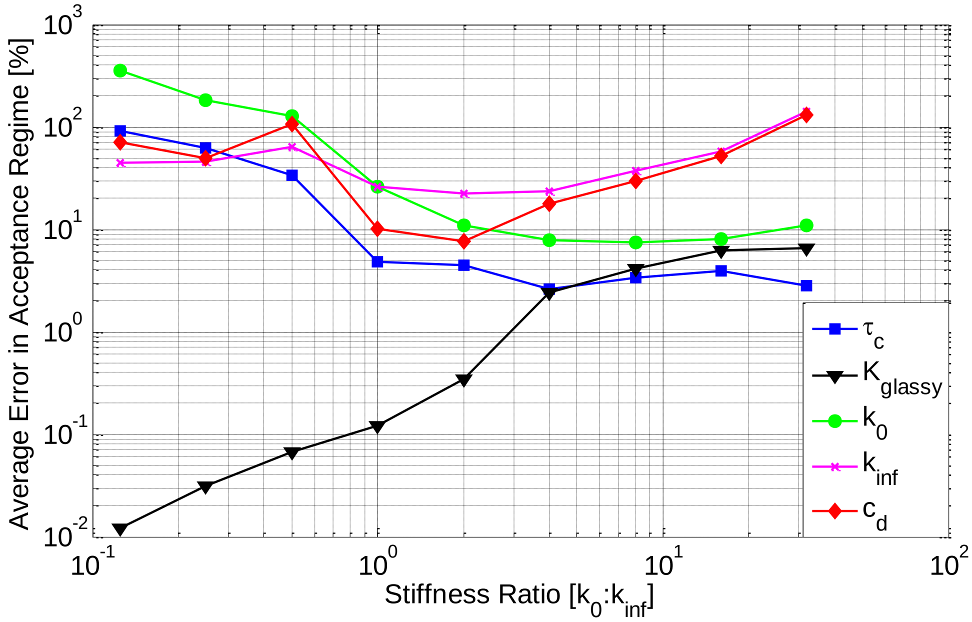

Figure 47. Average error of Stage 1 and Stage 2 variables within the acceptance regime versus Stiffness Ratio. Stage 1 variables (τ_c and K_g) are shown by the blue squares and black triangles, respectively. Stage 2 Variables (k_0, k_{inf}, and c_d) are shown by the green circles, magenta x's, and red diamonds, respectively.

There are several important observations about the response of error in the VETICA method to increasing stiffness ratio. For stiffness ratios less than 1:1 (i.e., k_{inf} is greater than k_0), only the glassy stiffness displays accuracy and all Stage 2 variables are dependent on the error experienced in the retardation time. However, as the spring ratio increases, the error in the retardation time decreases (and consequently the Stage 2 variables) but the error in the glassy modulus begins to increase. When the stiffness ratio is beyond 1:1 (i.e., k_0 is greater than k_{inf}), the effect of increasing glassy stiffness appears to influence the increase of k_{inf} and c_d while the error in k_0 continues to decrease and plateaus with retardation time. Due to the convolution in influence between the Stage 1 and Stage 2 variables, it is difficult to predict which stiffness ratio is best suited for the VETICA method. However, there appears to be a range near k_0:k_{inf} = 1:1 where all of the errors approach global minima (except K_g which constantly increases) and therefore a similar material construct would ideal to measure using the VETICA method. In conclusion, it appears that the retardation time is the largest influencing factor of the accuracy of the VETICA method although the influence of the glassy stiffness is observed for particularly high stiffness ratios.

Additional observations of AFM dynamics result from a change in stiffness ratio. Two selected features presented in this section are the relationship between peak penetration and peak force and the response of paddle amplitude to THC-SLS interactions. These system features are relevant to the discussion of measuring viscoelasticity because they are fundamental measurables in determining if AFM will be able to acquire the necessary signal data used in the VETICA method. The left axis of Figure 48 shows the relationship between the average maximum penetration distance and the stiffness ratio. Displayed on the right vertical axis is the average peak force versus the stiffness ratio.

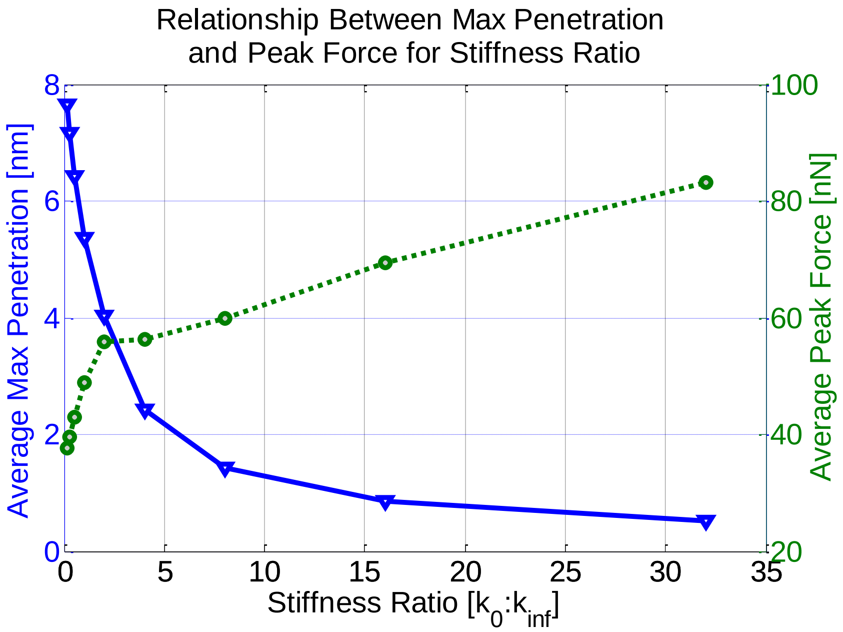

Figure 48. Relationship between Maximum Surface Penetration (left axis blue line with triangles) and Peak Force (right axis green dashed line with circles) as stiffness ratio changes.

Two observations can be made from Figure 48. First, the average maximum penetration that occurs with each tap appears to exponentially decrease and converges to 0 as k_0 becomes much larger than k_{inf}. As k_0 becomes much larger than k_{inf}, the tip penetrates less into the surface as the force in the Maxwell arm increases and the aggregate surface stiffness acts more rigid. This observation is important because it demonstrates that at higher stiffness ratios, the penetration depth cannot be used as a straightforward indication of the composition of the complex material stiffness. The second observation is that after the stiffness ratio has surpassed approximately 2:1, the average force exhibits a linear trend and does not respond exponentially, like maximum penetration depth. This observation seems to counter Hookean theory but can be explained by linear viscoelasticity. As the stiffness in the Maxwell arm increases with k_0, the overall repulsive force of the system increases. However, as the dashpot remains constant, the velocity of the dashpot increases as a result from a higher Maxwell force, causing the relaxation time during contact to decrease (see equations (54)-(56)). After the stiffness ratio has surpassed 2:1, the force relaxes proportionally by the same amount regardless of indentation, which appears to be linear.

The second AFM dynamic that is necessary to analyze is the amplitude of the oscillating THC paddle. Although the amplitude of the torsional paddle can be relatively smaller than that of the flexural cantilever and still provide measureable data (as explained in Chapter 2), an understanding of how small the oscillation amplitude becomes when interacting with the surface is still an important consideration when characterizing the surface. Figure 49 shows the amplitude of the paddle as both the dashpot and stiffness ratio values are changed.

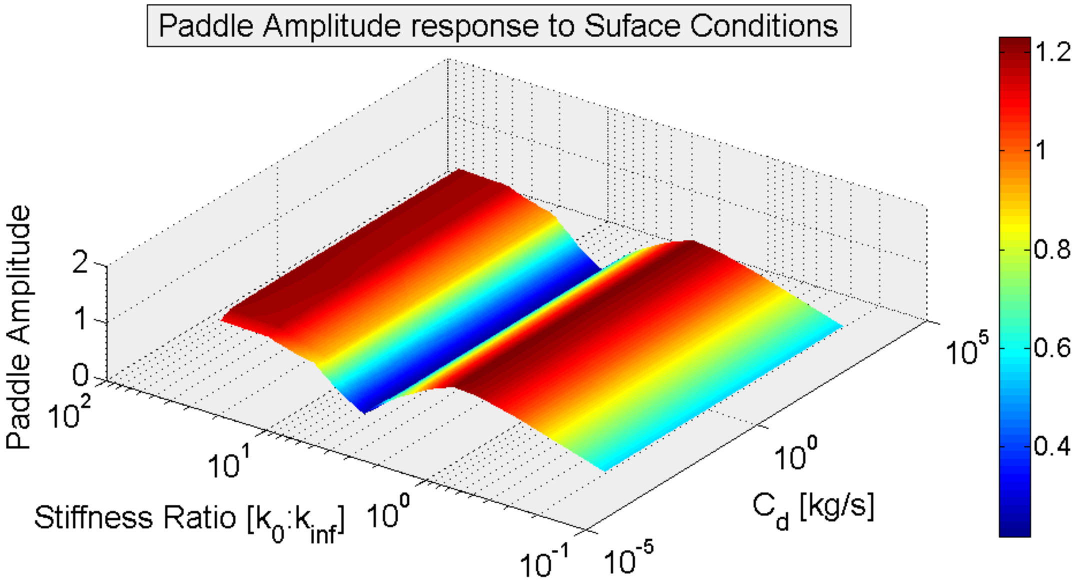

Figure 49. Amplitude of the paddle for various spring stiffness ratios plotted across increasing dashpot values.

Although the dashpot has little effect on the amplitude of the paddle, an observed minima exists as the ratio of stiffness approaches k_0:k_{inf} = 4:1 and two maxima as k_0:k_{inf} = 1:1 and k_0:k_{inf} = 32:1. This maxima ratio is near the minimum in error of the VETICA method from Figure 47. The observed decrease in amplitude could be due to the natural frequency shift of the SLS system as the stiff values increase. If THC-SLS does not impose an F_{ts} on the paddle where the frequency spectrum excites the fundamental frequency of the paddle, smaller oscillation amplitudes should be observed. In the case of this study, the maximum amplitude of the paddle coincides with the minimum error. Therefore, ideally the AFM would be tuned in an experiment to maximize the signal-to-noise (SNR) of paddle and extract precise data to be used in the VETICA method.

In summary, the most influential factor in the total error of the VETICA process is the extraction of the retardation time constant. For this reason, Figure 50 shows the relationship between the amount of energy dissipated and the error in extracting the retardation time. Figure 50 contains the same data as Figure 41 except that the interpolated surface is now color-mapped using the error of the retardation time.

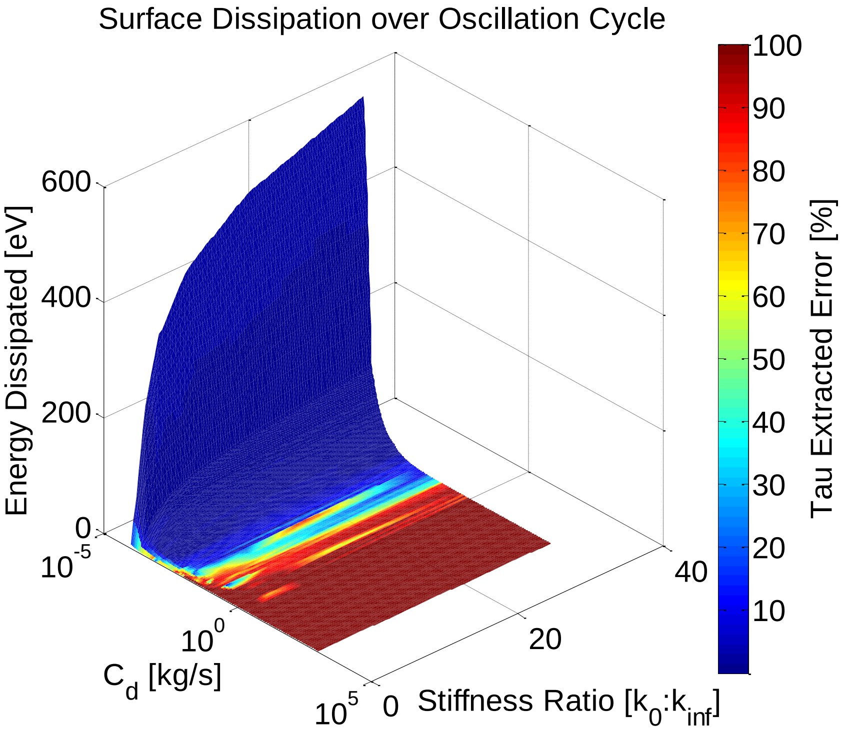

Figure 50. Average dissipated energy over one oscillation cycle color mapped with error in acquired retardation time from extraction technique.

The ability of VETICA to recover the retardation depends heavily on the amount of dissipation that occurs during each tap. When the dissipation loop is larger, the error for τ_c drops to favorable values (<10% error), but as dissipation decreases, the error quickly rises. This observation suggests that the VETICA method will show best results when imaging highly dissipative samples. The true mission of the remaining parametric study now becomes: how can the AFM best be operated in IC-AFM to extend the acceptance regime to include a particular material and minimize error of the VETICA method for extracting linear viscoelastic material properties?

4.5 AFM and THC Properties

Thus far, the VETICA method has been verified for its accuracy in an example and a parametric study has been performed on the surface characteristics that influence the accuracy of the method. The next section will continue the parametric study by analyzing the influences that controllable AFM operating conditions have on the accuracy of the VETICA method. In addition, recommendations will be made to minimize error of the method.

4.5.1 The Effect of Resonant Frequency of the Cantilever

The resonant frequency of the flexural cantilever was chosen for this parametric study because the frequency at which the THC interacts with the sample should affect the length of time between taps. In theory, as the THC oscillates with lower flexural frequencies, the time between taps should increase, and creep of less viscous surfaces that was previously too small to measure in the time between taps could potentially become measurable. Additionally, the time during contact would also increase and materials with longer relaxation times could become more measurable. To quantify this concept, a range of 10 to 100 kHz is chosen for the resonant frequency of the cantilever. The lower end of this range is to ensure that reasonable scan times can occur without the effects of drift or larger perturbations arising. The upper range could be extended, but is not because the anticipated benefits of changing the natural frequency of the cantilever are expected to occur at lower frequencies. This conclusion is made based on the characteristic relaxation times of common polymers which are typically on the order of seconds or minutes, while the tapping oscillation in dynamic AFM are occurring on the order of microseconds.

In order to maintain variable independence between cantilever and paddle resonant frequencies, each change in resonant frequency changes the paddle resonant frequency maintaining a constant ratio between the two natural frequencies. In the ensuing results, the paddle frequency is always 15 times larger than the cantilever and is based on the initial guidelines for the THC design [30]. Although changing the paddle frequency was previously simulated in this chapter to show the effects on the tip-sample interaction, it will not be included in this parametric study because it does not influence the overall time the trajectory spends in the interaction regimes. Figure 51 illustrates the dependence of natural frequency on times in the interaction regimes.

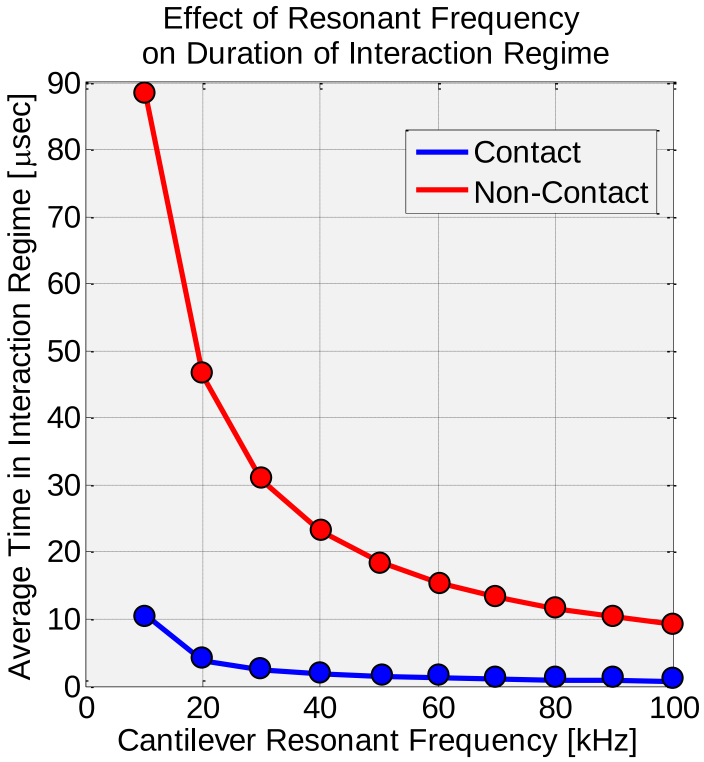

Figure 51. The relationship between cantilever resonant frequency and the time the tip trajectory spends in each interaction regime during an oscillation. The blue line denotes the contact regime and the red line denotes the non-contact regime.

When the natural frequency of the cantilever increases, tapping becomes more frequent and the tip spends less time in each of the two interaction regimes. Not as obvious, the contact and non-contact times of the oscillations decrease exponentially. This feature is advantageous to the experimentalist because for a small change in natural frequency, the range of measurable materials should increase exponentially proportional. The acceptance regime of dashpot value serves as a good indicator for defining the range of measurable materials. Figure 52 displays the shift in the acceptance regime as resonant natural frequency of the cantilever is varied. In order to calculate the acceptance regime, the regime is defined for all retardation time constant error that is less than 30%.

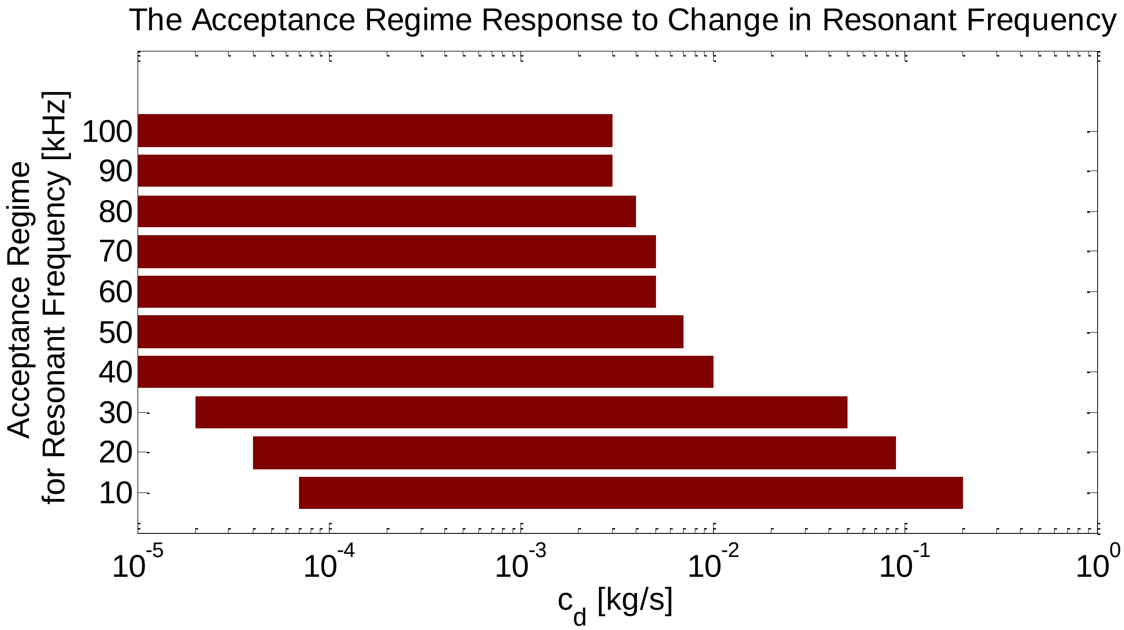

Figure 52. Shift in acceptance regime as cantilever resonant frequency is changed. In this case, the acceptance regime is defined for values which the error of the retardation time constant is less than 30%.

The range of values for which acceptance regime is reasonably accurate (less than 30% error for τ_c) shifts towards less viscous materials as resonant frequency decreases. Although on the upper bound of the range this is fairly intuitive, the shift on the lower end occurs because as the tap oscillation time increases, even materials with high viscosity (small c_d) values can completely creep to zero deformation before the next sequential tap. Therefore, error increases because the next tap is no longer able to measure any creep change from the previous tap based on the time interval. In practice, this means that there is a "sweet spot" for each cantilever which encompasses a range of viscous materials that it can accurately extract material properties. In general, if an experimentalists wishes to measure more materials with longer relaxation times (lower viscosity), a cantilever with a lower natural frequency should be chosen. The opposite recommendation is true for materials with lower relaxation times (higher viscosity).

To give an example of the error shift when changing cantilever resonant frequency, Figure 53 displays the error of the Stage 1 and Stage 2 variables at a point near the upper boundary of the acceptance regime for cantilever resonant frequency ω_{n1} = 30 kHz. The extracted materials properties in this example are taken from a system with the following surface and AFM conditions:

Table 5. Surface and AFM properties for example while changing cantilever natural frequency (ω_{n1}).

Surface Properties	Value	Units
Dashpot Value (c_d)	$8\text{x}10^{-2}$	[kg/s]
Stiffness Ratio (k_0:k_{inf})	16:1	[N/A]
AFM and THC Properties		
Amplitude Set point	70	[% of Free Oscillation Amplitude]
Free Amplitude	100	[nm]
Probe Stiffness (k_1/k_2)	10/700	[N/m]
Resonant Frequency (ω_{n1}/ ω_{n2})	10 - 100/ 150 - 1500	[kHz]
Print Step Resolution (PS)	0.5	[ns]

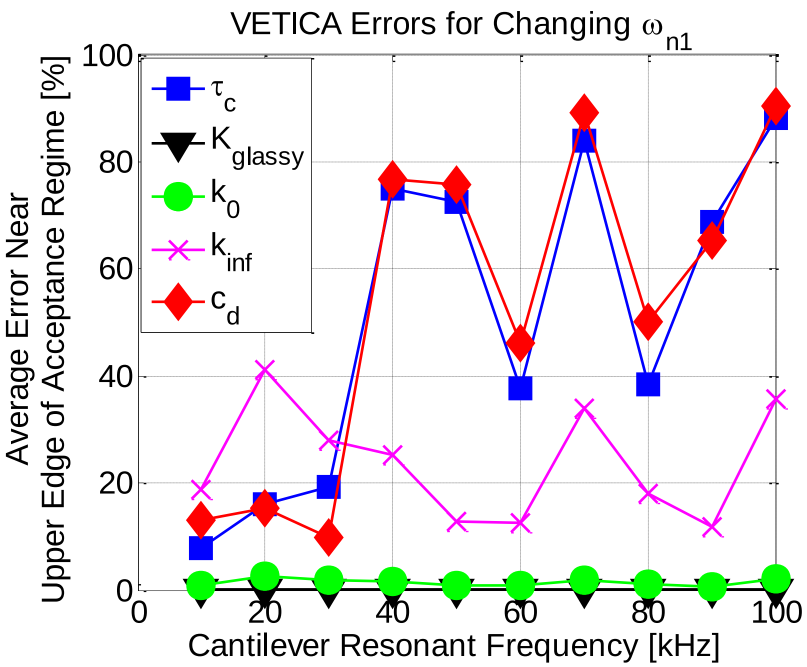

Figure 53. Error of Stage 1 and Stage 2 variables near the upper extreme of the acceptance regime. The range of cantilever resonant frequency and other system parameters can be found in Table 5. Stage 1 variables (τ_c and K_g) are shown by the blue squares and black triangles, respectively. Stage 2 Variables (k_0, k_{inf}, and c_d) are shown by the green circles, magenta exes, and red diamonds, respectively.

According to Figure 53, that as resonant frequency decreases away from 30 kHz the errors of the retardation time constant, and, on average, the others decrease as the acceptance regime shifts and this particular system falls within a more stable portion of the range. After the 30 kHz system, a large shift in error is observed as the systems with resonant frequencies higher than 30 kHz cannot maintain accurate material property extraction as the system being analyzed has shift outside of those acceptance regimes.

In conclusion, the resonant frequency of the flexural cantilever is found to affect the range of the acceptance regime for the retardation time constant. Based on the trend information in Figure 52 and the justification from the example in Figure 53 it is recommended that lower resonant frequency cantilevers be chosen for materials with longer relaxation times, and higher resonant frequency cantilever be chosen for surfaces with shorter relaxation in effort to maximize the accuracy of the VETICA method.

4.5.2 The Effect of Amplitude Set Point

Similar to resonant frequency, the amplitude set point is an AFM system characteristic that can be easily predefined by the user. In this study, the amplitude set point was varied from 25-80% of the free oscillation amplitude, which in this case was 100 nm. These values were chosen because they represent common system conditions that the average AFM user implements in experimentation. The first effect that is examined is the effect of the amplitude set point on the contact times the tip experiences in the contact and non-contact regime during the oscillation. Figure 54 displays the relationship between these two regimes while amplitude set point is varied. As the amplitude set point increases, the non-contact interaction time increases, and because the overall oscillation period is held constant, the contact interaction time is therefore inversely proportional to the increase in amplitude set point. In other words, as the amplitude is controlled to be smaller values of the free oscillation amplitude, the tip is in contact with the surface for a longer time (and therefore larger percentage) of the trajectory. At higher amplitude set points (40% and beyond), the proportionality appears to be linear. This observation suggests that a linear change is expected with contact and non-contact times as amplitude set point is varied until a certain point, after which more exponential changes occur. It should be noted that the overall time change from altering large percentages of the amplitude set point are relatively smaller than the changes in contact and non-contact times experienced when changing the resonant cantilever frequency (see Figure 51).

Therefore, a recommendation is made that a user of the AFM could use the amplitude set point as a "fine tune" the amount of contact and non-contact times and use the cantilever resonant frequency as a "coarse tune" to optimizing the range of materials investigated using the VETICA method.

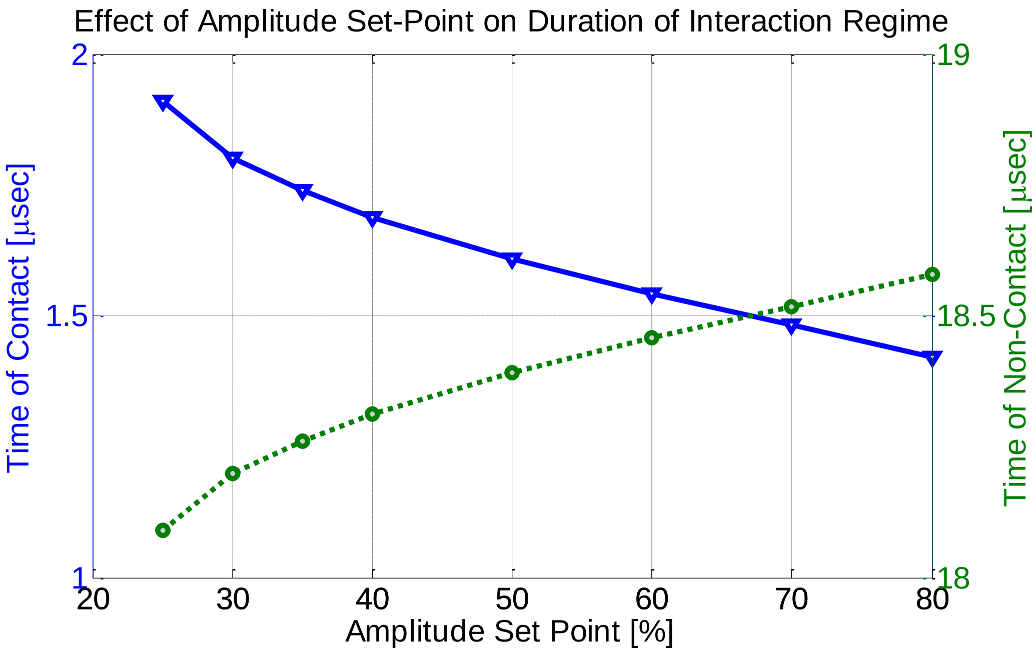

Figure 54. The relationship between amplitude set point and the time the tip trajectory spends in each interaction regime during an oscillation. The contact regime (left axes blue line with triangles) and non-contact regime (right axes green dashed line with circles) are for a single oscillation with a period of 20 μs.

There is not an anticipated significant shift in the range of the acceptance regime with variation of amplitude set point because the changes in contact times are much smaller than the changes observed when the cantilever resonant frequency was used as the changing variable. As a result of the slight change in acceptance regime, the average errors calculated across the majority of the acceptance regime can be used to determine the overall effect of amplitude set point on the accuracy of the VETICA method. Figure 55 displays the average error of the Stage 1 and Stage 2 variables in the acceptance regime as amplitude set point is changed.

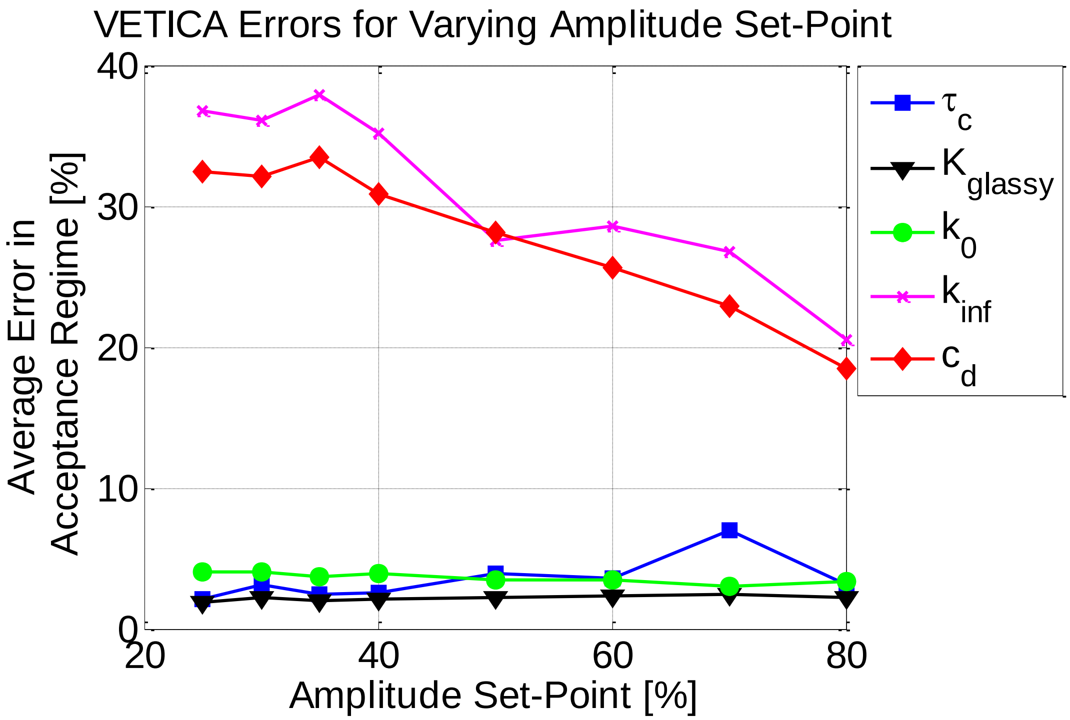

Figure 55. Average error of Stage 1 and Stage 2 variables within the acceptance regime versus Amplitude Set point. Stage 1 variables (τ_c and K_g) are shown by the blue squares and black triangles, respectively. Stage 2 Variables (k_0, k_{inf}, and c_d) are shown by the green circles, magenta exes, and red diamonds, respectively.

In general, error of the Stage 2 variables c_d and k_{inf} decreases as amplitude set point increases. This trend could be attributed to the fact that perturbations of the sinusoidal form of the trajectory are lessened as the amplitude set point approaches the free oscillation amplitude. Higher perturbations of the sinusoidal trajectory would induce errors in the Spectral Inversion Method which relies on an ideal harmonic oscillator transfer function. The cause of higher perturbations would be caused by deeper indentation depths and therefore higher interaction forces as amplitude set point decreased. The effect of indentation depth will be discussed in the following section. In conclusion, although the overall acceptance regime is not affected by the change in amplitude set point, it can still be used to fine tune amount of creep and stress relaxation the tip undergoes during the oscillation. However, it should be cautioned that low values for amplitude set point the error of the extracted material properties k_{inf} and c_d increase.

4.5.3 The Effect of Indentation Depth

As seen in equation (78) the indentation depth of the tip position during the oscillation is a linear operator to computing the interaction force F_{SLS} use to fit to the AFM signal force F_{ts}. Figure 56 shows the relationship between amplitude set point and the average maximum indentation depth and resulting average peak force.

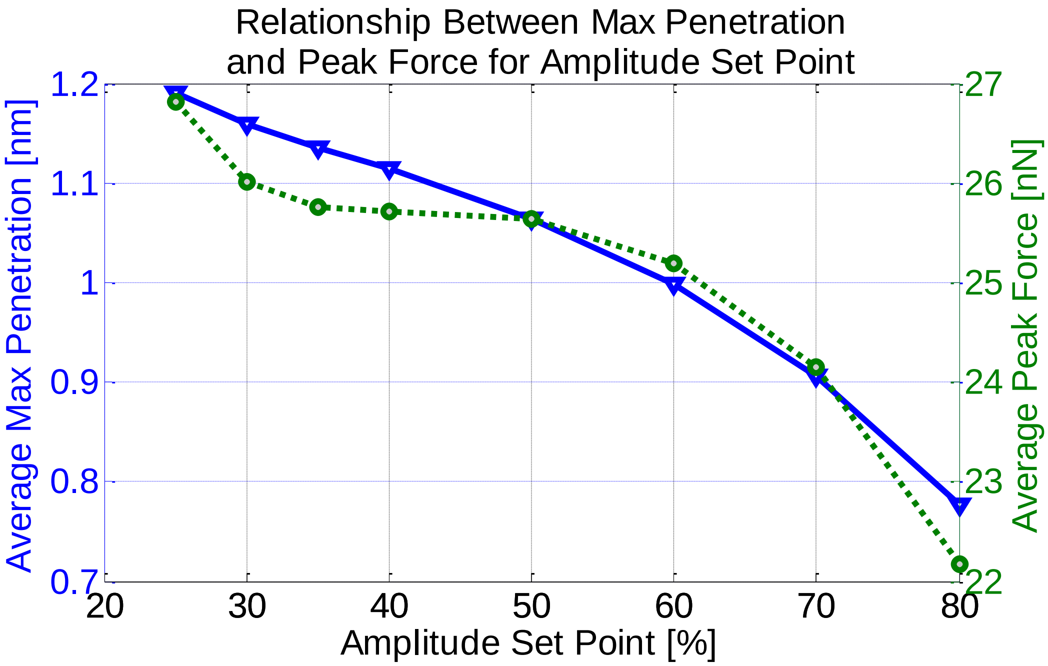

Figure 56. Relationship between Maximum Surface Penetration (left axes blue line with triangles) and Peak Force (right axes green dashed line with circles) as Amplitude Set Point changes.

It is seen that both the indentation depth and peak force decrease in magnitude as the amplitude set point increases. It is observed that the average peak force is non-linear, but appears to be proportional to the non-linear qualitative shaped of the penetration force. As a result, a further examination of the indentation depth should yield information about these observed non-linear effects. As an initial step, the steady state zero reference equilibrium position gives a good indication of how the SLS responds to the THC because it represents the steady state deformation after tapping has commenced. Figure 57 displays the steady state zero reference equilibrium indentation as the dashpot damping coefficient is varied.

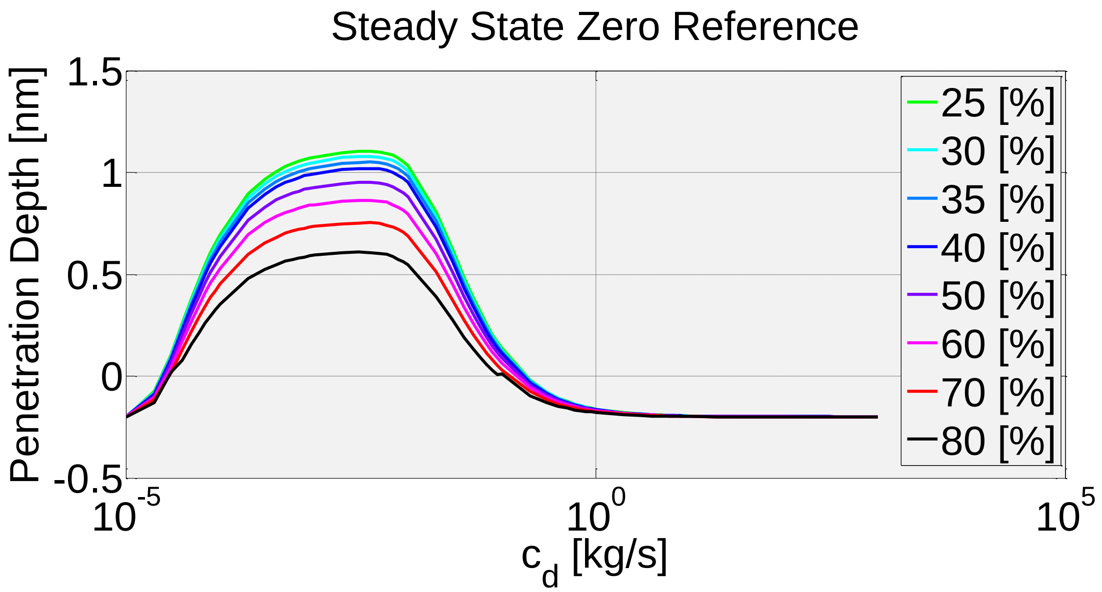

Figure 57. Point of reference for the surface equilibrium zero after intermittent contact had achieved steady state. The different colored lines represent various percentages of Amplitude Set Point and are plotted along dashpot values ranging from 1x10^{-5} - 1x10^{3}.

Similar to the acceptance regime, there is a range (again it will be called the "sweet spot") of dashpot values where the steady state equilibrium decreases and the surface appears "softer." However, there are certain dashpot values, at both ends of the range, where the steady state zero reference equilibrium depth is slight and the sample would appear "stiffer." Within the regime where the depth steady state zero reference equilibrium is more responsive, the variation of depths across amplitude set points becomes clearer. As the amplitude set point is increased, the steady state penetration becomes more and more shallow. To evaluate the effect this steady state indentation depth has on the error, the extracted retardation time constant is colored over the surface plot of penetration depth verse the dashpot c_d and amplitude set point values seen in figure Figure 58. The retardation time is chosen as the variable to plot error because it displays the most amount of divergence across change in surface constants.

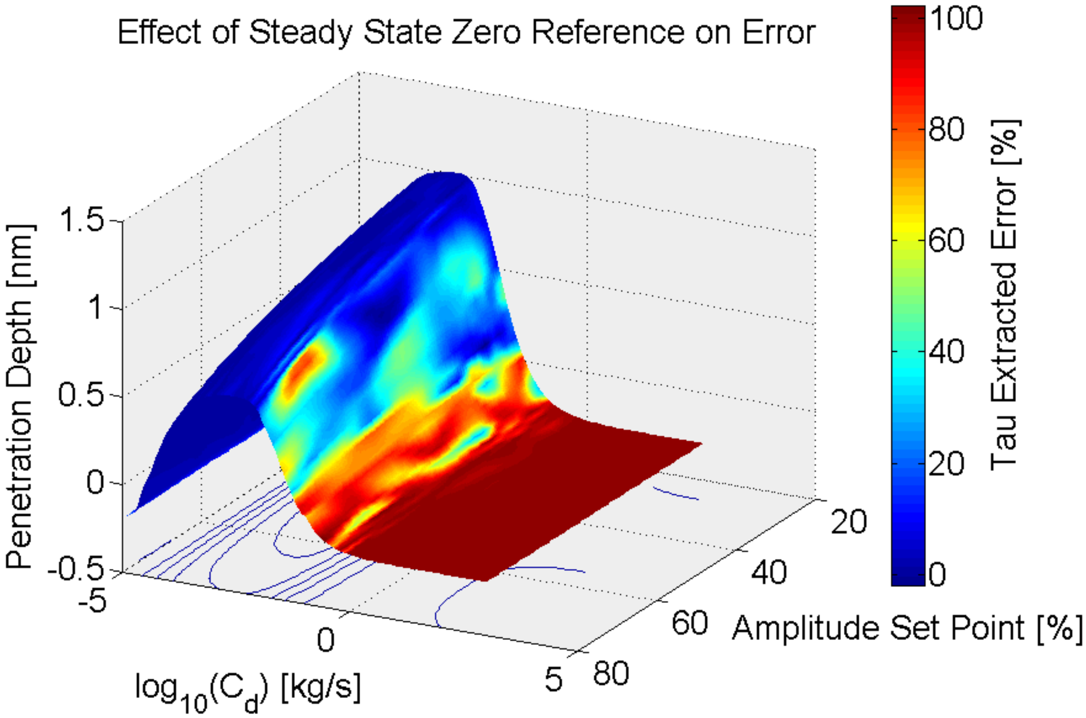

Figure 58. Effect of steady state zero reference on VETICA error for τ_c plotted across amplitude set point.

The error of the retardation time constant increases rapidly as the steady state reference zero equilibrium depth falls outside of the “sweet spot.” The contour lines of the plot show the effect of the steady state zero reference as amplitude set point changes, and the blue color indicates a low error for all values.

4.5.4 The Effect of Instrument Resolution

A critical aspect to any measurement device is the resolution. The AFM itself made such a profound impact in the field of nanoscience because of its high resolution relative to other instruments imaging at the scale size. In fact, this is such a hot topic in the AFM community that recent work by Wright *et. al.* [95] was conducted to validate controversial claims of subangstrom spatial resolution of the instrument in ultrahigh vacuum [34]. Therefore, the effects resolution should be analyzed when proposing a new method such as VETICA because resolution is a fundamental factor at the forefront of advancing imaging capabilities of measurement instruments.

The question then arises, which type of resolution should be analyzed? The AFM recovers signals in both the spatial and temporal domain; or in other words, distance dependent signals from measured tip deflection and time dependent signals contingent on the data acquisition instrumentation. For the purposes of this thesis, the temporal resolution will be analyzed the spatial resolution is proportionally changes in the temporal (time acquisition) resolution. It is also easier to implement a temporal resolution change in code through the print step, than it is to implement a spatial resolution for the tip position where velocity is not constant. In this study, all simulation use the same time step (i.e., time interval between iterations of the numerical integration) and the resolution is altered by changing the print step (i.e., time interval between data prints to the output file). In this way, the overall numerical approximations made between each time iteration do not skew with variation in resolution and the results are comparable.

A comparison of multiple print step resolutions with acquired surface positions is shown in Figure 59. Figure 59A shows the point upon approach where the tip first contacts the surface, and Figure 59B shows the retract. The “Measured Position” seen shows the spatial deviation between the actual surface position and what the AFM “sees” as the surface as a result of the VETICA method. This deviation in position is a downstream effect from the deviation seen in the time at which contact and separation occurs from the minimums of the force as shown in Figure 32.

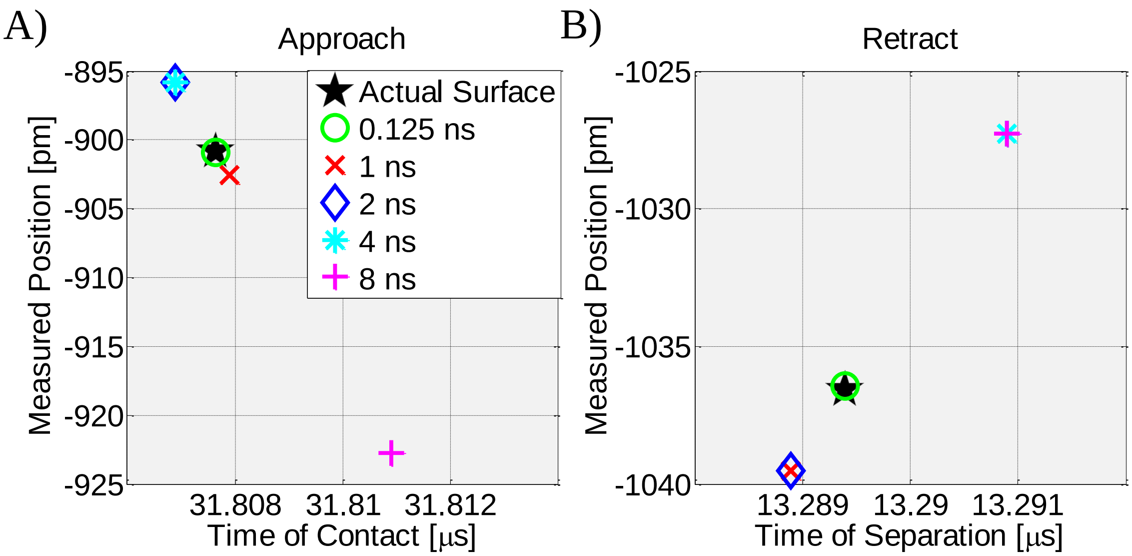

Figure 59. A) Approach and B) Retract data for measured interaction time versus measured position by the AFM. Print step resolution is shown by markers with the exception of the black star, representing the actual known surface location and time of interaction. System conditions are ω_{n1} = 50 kHz, ω_{n2} = 750 kHz, k_1 = 10 N/m, k_2 = 700 N/m, $A_{setpoint}$ = 70 nm, τ_c = 4x10^{-4} kg/s, and SR = 16:1. Note the units of distance here are picometers.

As the resolution increases, the accuracy of the surface position based on the VETICA method increases. To measure the deviation between the VETICA approximation of the surface and the true surface position, Figure 60 displays the measured deviation (in picometers) from print steps of 0 to 15 ns. It should be noted that the data appears to “oscillate” about an average (calculated and plotted in black). This oscillation occurs from because as the resolution (i.e. spacing) between time points of a fixed length time dependent signals are varied, the point does not always fall in the bottom of the well, and hence particularly at lower resolutions (higher print steps) the oscillations in deviation increase.

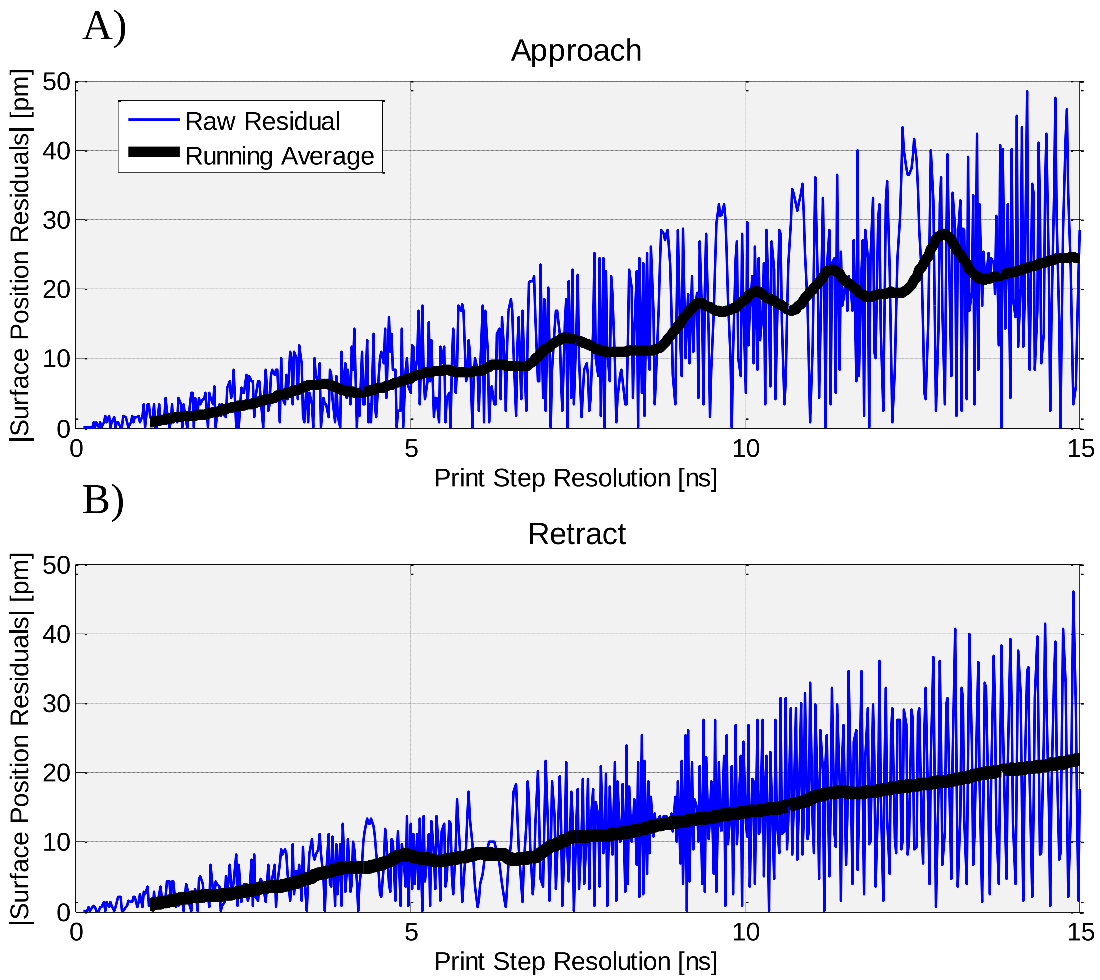

Figure 60. A) Approach and B) Retract data for the absolute value of the variation between actual surface position and measured position by the AFM. The running average lines are displayed to show comparisons in growth between the two plots. The system simulated is the same as seen in Figure 59.

It is seen from the data is that the average residual from actual surface to measure surface form the VEITICA method appears to increase linearly proportional to increase in print step resolution. Therefore, it can be concluded that increasing the resolution (or decreasing the print step) through improved data acquisition methods and equipment. It should be cautioned however, that the consequence of increasing the data acquisition rate (or bandwidth) of any instrument also increases the position signal noise that accompanies the higher temporal resolution. Although it is not explored within this thesis, an advantage of the Spectral Inversion Method force reconstruction procedure is that filters can be applied to the signals to help alleviate the effects of added noise.

To apply these conclusions about instrument resolution, Figure 61 displays the resulting fit of the retardation time constant for several print step resolutions across varying dashpot values.

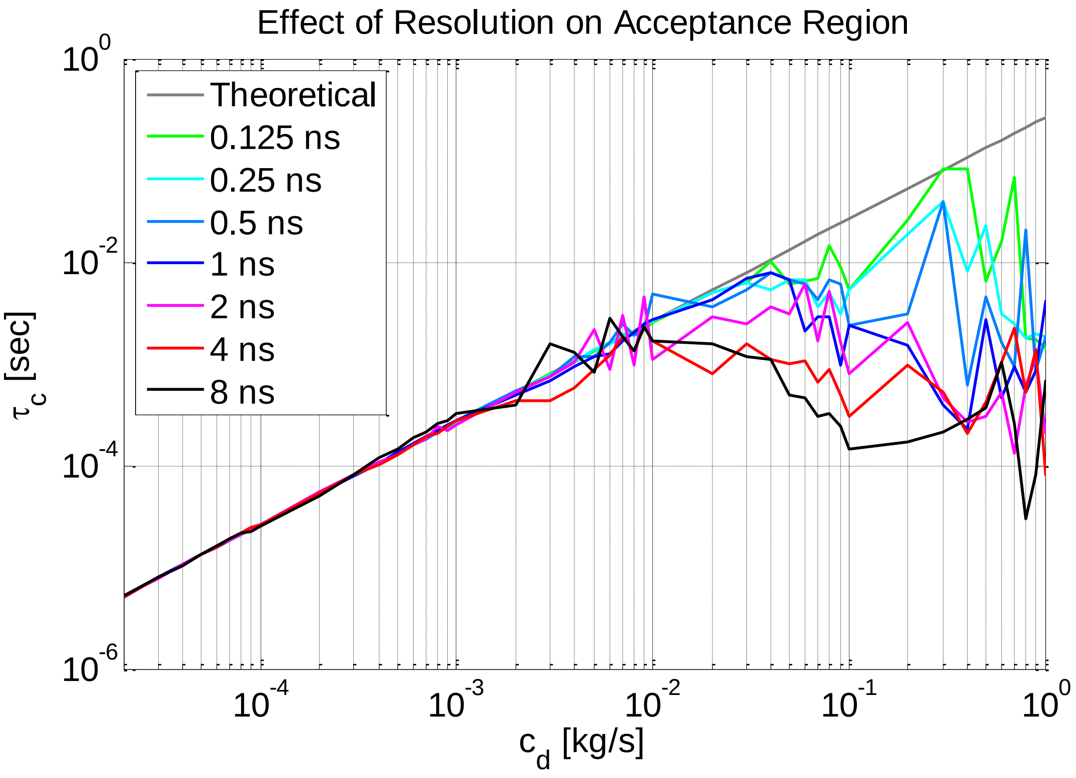

Figure 61. Effect of Print Step Resolution on the range of the Acceptance Region. The colored lines represent different data acquisition rates in ns. The system simulated is same as Figure 43.

The results in Figure 61 confirm the data in Figure 60 that at lower print steps, the higher resolution increases the range of the acceptance regime for a given system. In conclusion, as AFM instrument resolution increases with further advancements of data acquisition instrumentation, it will be possible to increase the range of the acceptance regime, and improve overall accuracy of the VETICA process. Filtering and other signal conditioning can be taken advantage of in the frequency spectrum when the Spectral Inversion Method is implemented to help alleviate the increase in noise that results from higher resolution.

4.6 Experimental Considerations

The VETICA method has now been proven to be effective through a comprehensive example problem, and a parametric study on various surface and AFM operating conditions has been performed to evaluate the extent of the method and recommendations on improving the accuracy. The final section of this chapter begins by approximating expected time for scans using the VETICA method and concludes by relating the extensive material properties explored in the parametric studies to measured intensive material properties of real viscoelastic materials such as modulus and dynamic viscosity.

4.6.1 Scan Time for a Full Image

The real time imaging of viscoelastic material properties is at the core of the work presented in this thesis. Therefore, such a study would not be complete without analyzing the implications the proposed VETICA method has on imaging times. The first calculation of the method depends on the time necessary to implement the VETICA method. While nearly all of the mathematics needed to implement the method are instantaneous, some of the fitting procedures can become time consuming. In particular, the time to perform the nonlinear optimization can vary as much as ± four seconds. On average, the method takes approximately 20 seconds per force curve using MATLAB on a computer with dual core processor each at 2.3 GHz and at 3.74 GB of RAM and would be potentially faster if performed in a more efficient language or on a more powerful computer. Fortunately, the post processing of the VETICA method can be performed simultaneously for all pixels post or concurrent with imaging because each force curve for a pixel is recorded through the Spectral Inversion Method independently of the previous position. Therefore, the material extraction could be performed simultaneously within imaging and would not add any time to the imaging process.

The next consideration for imaging time is the time it takes to reach steady state tapping when the force curve data is recorded. The time to steady state tapping depends on AFM system properties like the quality factor and the resonant frequency of the cantilever as well as the PID controller gain. As an estimate, the settling time for the majority of the simulations is near the time periods seen the transient to steady state settling of Figure 18. Using this estimate, the IC-AFM interaction has reached steady state in 15 ms. If it is assumed that a single pixel of a 256x256 image can be captured in that amount of time, then a each line could be scanned at a the fastest rate of approximately 3.84 seconds and an entire 256x256 pixel image would take approximately 16.4 minutes. In practice, this scanning estimate is significantly faster than the current force recovery methods for other real-time force acquisition methods and although the estimates for imaging times could increase or decrease for various system and controller settings, these estimates are typical conditions under which a user would be imaging in ambient air IC-AFM with the AFM.

In addition to understanding the imaging time, an additional issue of the VETICA method is the limitations of the surface spatial resolution due to deformation contamination of one pixel to an adjacent pixel. In other words, because the VETICA method requires deforming the surface, local adjacent planer pixels to the measured pixel will experience some contaminating deformation which could result in a limiting minimum distance between pixels, thereby limiting the mapping resolution of the VETICA method.

4.6.2 Connection to Real Samples

The VETICA method has been proven to be capable of extracting linear viscoelastic material properties in terms of elastic springs and viscous dashpots of a surface modeled as a Standard Linear Solid in the Zener configuration. However, the context of these material properties have not been contextualized in terms of the intensive properties they represent of viscoelastic materials measured in experiment. Therefore, the DMT relationship from equation (4) will be used to approximate the geometric and boundary conditions of the materials used and convert the values to moduli of elasticity and dynamic viscosity. These values are then compared across previously measured variables to understand which viscoelastic materials could utilize the VETICA process and future experiments could be performed to experimentally validate the methodology.

In order to make an approximation on how the simulated SLS material properties compare to modulus and viscosity, the stiffness of the springs are first converted. In order to approximate the modulus, the peak forces (and coinciding peak penetration depths) are used to calculate the DMT equivalent modulus E$_{\text{sample}}$ through the following taken from previous (equation (4)):

$$F_{SLS} = F_{DMT} = \frac{4E^*\sqrt{R_{tip}}}{3}(a_0 - d)^{3/2} \quad \text{for} \quad d \leq a_0 \tag{90}$$

Rearranging: $$E^* = F_{SLS} \frac{3}{4\sqrt{R_{tip}}(a_0 - d)^{3/2}} \quad \text{for} \quad d \leq a_0 \tag{91}$$

And with: $$\frac{1 - \nu^2{}_{sample}}{E_{sample}} = \frac{1}{E^*} - \frac{1 - \nu^2{}_{tip}}{E_{tip}} \tag{92}$$

where Table 6 gives the assumed material and conditions of the THC and surface. The tip is assumed to be made from silicon.

Table 6. The material properties and assumed conditions for the SLS to DMT conversion process from extensive to intensive material properties.

Variable	Value	Unit
R_{tip}	10	nm
ν_{tip}/ν_{sample}	0.3	N/A
a_0	0.2	nm
E_{tip} (Si)	130	GPa

Using this approximation, the values for E_{sample} can be estimated as ranging from 32 MPa to 9 GPa before relaxation occur. This range of moduli includes most viscoelastic polymers studied with nano indentation [96-98] as well as many viscoelastic biological tissues measured with AFM [99]. Therefore the VETICA method has been explored and validated for materials which posses internal stiffness

To calculate viscosity, the characteristic relaxation times can be used along with the approximations for modulus to calculate respective dynamic viscosity ranges. The characteristic relaxation times need no approximation because they are the ratio of the two SLS parameters and given in units (seconds) which are independent of surface properties. From the characteristic relaxation times and the estimated values for the modulus, the viscosities explored in this thesis are estimated to be between 700 Pa·s and 70 Gpa·s. While is range seems expansive, it should again be emphasized that the results of the VETICA method held true for an acceptance regime of viscosities which translate approximately to a dynamic viscosities ranging from 700 Pa·s to 70 MPa·s for the majority of simulations. Although the upper range of this includes some very soft polymers, the majority of viscoelastic materials relax on the order of seconds to tens of seconds. Therefore, although the VETICA method is feasible to implement on viscoelastic materials, the acceptance regime discussed in this thesis must be expanded further using the recommendations presented in order to include less viscous viscoelastic materials.

Chapter 5: Conclusion and Future Outlook

5.1 Summary of Results

In this thesis, a method (titled the Viscoelastic Extraction Technique for Intermittent Contact Atomic Force Microscopy or "VETICA") has been developed to extract linear viscoelastic materials in IC-AFM. The VETICA method consists of a two-stage process where in Stage 1 characteristic constants of the viscoelastic material (retardation time and glassy stiffness) are calculated from AFM signal data, and the material properties of the linear viscoelastic material are solved for in Stage 2 using a non-linear least squares fitting technique.

In order to implement the VETICA method, a technique called the Spectral Inversion Method is used to acquire the tip-sample force in real time and the accuracy of the method is enhanced through the simulation of a specialized probe design called the Torsional Harmonic Cantilever (THC). The sample is modeled as a linear viscoelastic material using the Standard Linear Solid (SLS) configuration comprised of two elastic springs and a viscous dashpot.

The THC and SLS are successfully implemented in computational simulations and results are presented on the interaction between tip and sample. The surface dissipation experienced during the contact regime of a tap is influenced by the number of multi-peaks in repulsive force arising from the high frequency oscillations of the paddle. Additionally, the number and intensity of these multi-peaks are influenced by the physical vibration characteristics of the paddle. The inclusion of van der Waals force acting on the surface has negligible effects on the VETICA method.

The accuracy of the VETICA method is then explored and validated through a detailed example problem where Stage 1 and Stage 2 variables are extracted with high accuracy. Conclusions are made on optimization and curve fitting procedures and the method is found to be capable of extracting the viscoelastic material properties with less than two percent error.

A parametric study is then performed on the material constants of the SLS surface and AFM conditions. The surface constants of dashpot value and stiffness ratio of the elastic springs are explored because they show a dependence on the energy dissipated per oscillation cycle, thereby affecting the viscoelastic dissipation caused by force hysteresis. When the dashpot is examined, there is a range of values for which the VETICA method is accurate and is titled the “acceptance regime.” The extraction of the Stage 1 variable retardation time constant has the largest influence on the accurate extraction of the material properties c_d, k_{inf}, k_0, and therefore is the most sensitive variable of the extraction method.

The second half of the parametric study investigates the variables that the AFM user can control to improve the accuracy of the method. Decreasing the natural frequency of the flexural cantilever shifts the acceptance regime to include less viscous materials. While this controllable feature of the AFM acts as a "coarse tune" to altering the range of materials for which the method is accurate, when the amplitude set point is adjusted, it is found that the contact and non-contact percentages of the total oscillation period can be adjusted and used as a "fine tune". However, adjusting the amplitude set point does not insure equal error of extracted values and it is found that error decreases and amplitude set point approaches the free oscillation amplitude. The indentation depth is then analyzed and there is a range of viscosities where the steady state zero reference equilibrium penetration depth increases and consequently, the error of the retardation time constant drastically drops. This so-called "sweet spot" is concluded to be ideal in locating when scanning in order to maximize the results of the VETICA method. The final AFM feature explored in the parametric study is the instrument's time resolution. It is found that as the print step resolution of the time dependent signals increases, the accuracy of the VETICA approximation of the surface increases. It is also known that noise increases with higher resolution data acquisition, however the Spectral Inversion Method allows for signal filtering in the frequency domain which could alleviate this noise increase.

The final results of the thesis explore the application of the VETICA method under real experimental conditions. First, the imaging time associated with implementing the method is investigated. The method would take an estimated 16 minutes to acquire a 256x256 pixel standard size image. This is assuming that the VETICA method (which takes on the order of 20 seconds to implement) can occur post imaging and that the force curves for each pixel can be processed simultaneously. The other experimental consideration made is the translation of the extensive material properties simulated in the thesis to the intensive material properties found in experiment. The simulations where the VETICA method is relatively accurate cover material stiffness in the range of approximately 32 MPa to 9 GPa which includes a majority of the viscoelastic polymers and biological tissues studied in literature [19, 100-102]. The dynamic viscosities are calculated from 1.25 Pa·s to 3.6 GPa·s for the accurate extractions from the VETICA method and can be applied to such materials by changing the aforementioned AFM conditions from the parametric study.

In conclusion, the VETICA method is a first step towards defining a means of rapidly acquiring viscoelastic materials through IC-AFM on the microscopic scale and the following section will discuss the implications this work has on the science community and the anticipated benefits of applications.

5.2 Intellectual Contributions and Anticipated Benefits

This thesis offers several contributions to enhance the surface characterization of viscoelastic materials in IC-AFM. The five most important are as follows:

(1) Computational simulation of the Torsional Harmonic Cantilever (THC) and the Standard Linear Solid (SLS) in IC-AFM to understand the dynamics of the technique when interacting with a linear viscoelastic sample.

(2) Theoretical development of the VETICA method by which experimentalists can accurately extract *quantitative values* for material properties like the Young's modulus and dynamic viscosity of a viscoelastic material (under the assumption that it behaves linearly).

(3) An investigation into the dissipative contributions of surface viscoelasticity towards the aggregate dissipated energy per cycle experienced by the AFM cantilever.

(4) Recommendations to adjust experimentally tunable variables in order to improve the accuracy of the VETICA method as applied to various magnitude ranges of surface stiffness and viscosity.

(5) Analysis of the connection to real samples and imaging times in order to quantify the improvement of the VETICA method over conventional approaches to characterize viscoelastic surfaces.

The development of a new method to acquire quantitative viscoelastic material properties in IC-AFM is a significant step towards true nanoscale surface characterization with the AFM. This advancement could result in the material classification of polymeric and biological substances (among other soft materials) in ambient air and liquid environments at a previously unattainable size scale and acquisition rate. The acquisition of material constants at this scale can be used to compare measured macroscopic properties to unknown local stiffness and dynamic viscosity without any prior knowledge about the surface and without the need to use a reference material as is the case with current AFM methods [45, 50, 103]. The ability to acquire viscoelastic material properties at the nanoscale is useful when designing complex polymers with non-homogeneous surfaces where the knowledge of macroscopic material properties is not sufficient and where there is a need to resolve and measure sub-continuum features.

Additionally, the application of the VETICA method from this thesis contributes to the mapping and characterization of viscoelastic biological substances of interest to medical fields. Local material properties of cells and tissues provide information about biological conditions and facilitate the identification and origination of diseases such as cancer – where the change of local stiffness has recently been used as a detection mechanism using the AFM [104, 105]. The implementation of the method provided herein could decrease the scan time, increase image size, and potentially increase characterization rate of these viscoelastic substances.

Through the VETICA method, it will be possible to extract viscoelastic material properties using only the experimentally measured signals of the AFM. More precisely, the extraction of material properties will be carried out directly from the AFM time, force, and position signal data and the constitutive equations of viscoelasticity, bypassing the need to use the phase and amplitude of the cantilever response, which can be complicated by dissipation forces other than surface viscoelasticity. The accuracy of the method only depends on the resolution of the time signals of the instrument and the governing equations of the surface model, which if enhanced, would improve the future accuracy of the method and expand the application of the proposed technique to a larger set of viscoelastic materials.

5.3 Future Outlook

In progressing forward, there are two suggested directions on the future research of method development of characterizing viscoelastic materials. The first that will be addressed with preliminary results is the measurement of "4-Dimensional" force curves where the velocity of the tip is related to the traditional force versus distance curve. The second suggested direction is the expansion of the models used to describe a viscoelastic surface beyond the SLS.

5.3.1 4-Dimensional Force Curves and Preliminary Results

As previously defined, viscoelastic materials have a dependence on the rate of deformation. In terms of the AFM dynamics, this rate of deformation is the velocity of the tip during contact. Extraction of the tip velocity comes particularly easily when applying the Spectral Inversion Method. The first derivative of a signal z(t) in the time domain can be calculated using the following rule of Fourier mathematics [106]:

$$\dot{Z}(t) = 2\pi i\omega\hat{Z}(\omega) \tag{93}$$

where:

$$\hat{Z}(\omega) = \mathcal{F}\{Z(t)\} \tag{94}$$

The notation $\mathcal{F}$ represents the Fourier transform of a signal. Using this relationship, now the Spectral Inversion Method can be expanded to compute the force as a function of time, position, and velocity along the x-y scanning plane of the surface. The addition of velocity allows for the force curve to be expressed with an additional axis, and produce a "4-Dimensional" force curve seen in Figure 62. The force is now plotted along the following four dimensions:

1) The lateral x-axis that forms part of the surface plane of the image

2) The lateral y-axis that forms part of the surface plane of the image

3) The vertical tip-sample distance (*d*).

4) The vertical velocity of the tip

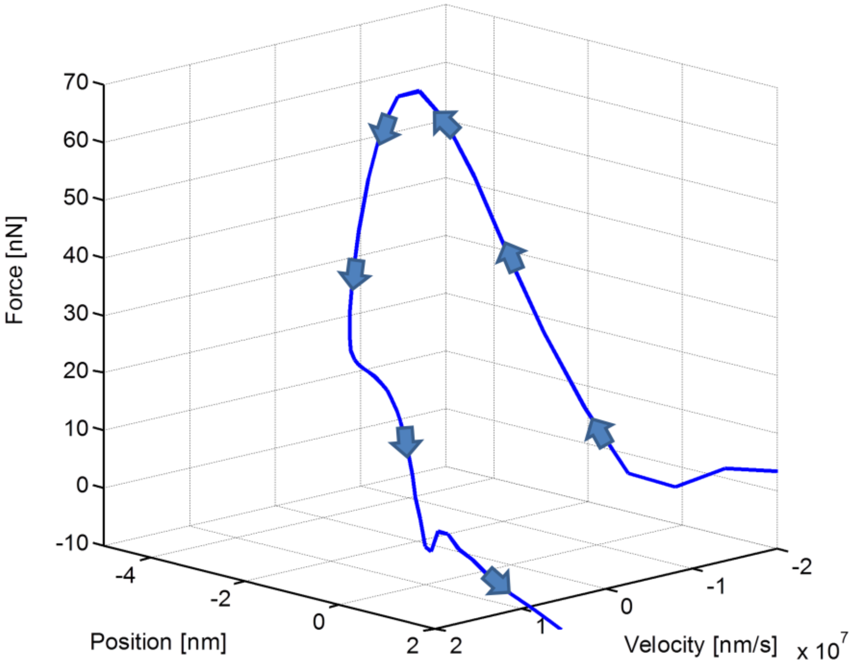

Figure 62. The 4-Dimensional force curve with the force versus distance graph plotted against an additional velocity axis extracted through the Spectral Inversion Method. The arrows are indicative of the tip trajectory as time increases.

The new visualization of the force versus distance versus velocity is a new concept that has not been used in AFM for analysis of tip-sample interaction. Although this work has not yet found a quantitative relationship between these plots and the viscoelasticity of the surface, qualitative trends can be seen such as examples shown in Figure 63 and Figure 64 where the response of the interaction force can be seen with changes in position and velocity as a system parameter is varied. When hysteresis loops are present in the force curves, the velocity dimension allows the loop features to be analyzed. For example, in the case of the multi-peaks of force experienced in the data of Figure 63 and Figure 64 resulting from the THC, we can see that the multi-taps form loops, the area of which would give dissipated power per multi-tap.

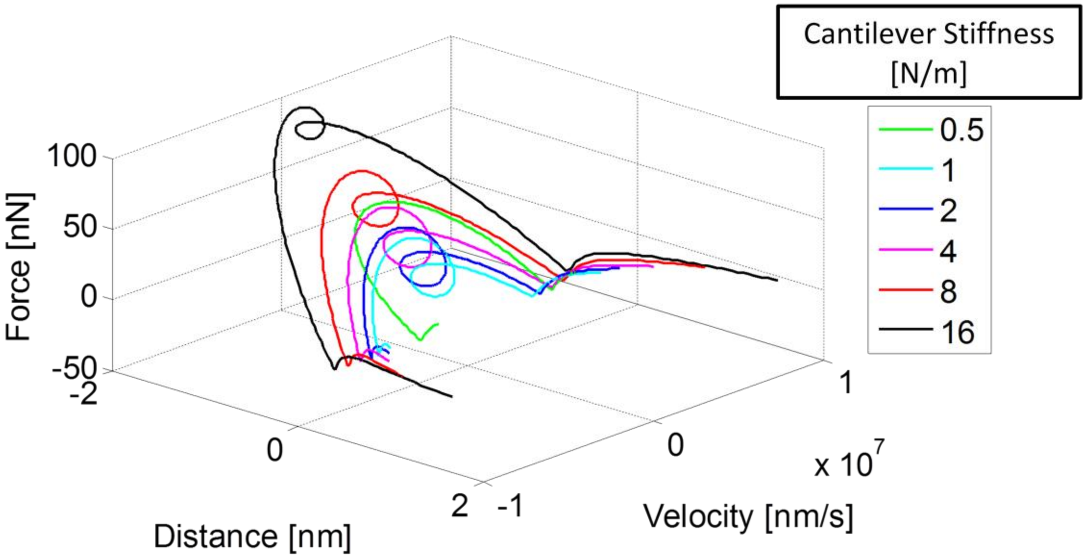

Figure 63. 4-D force curves plotted while cantilever stiffness [N/m] is varied. The different colored lines indicated different stiffness values.

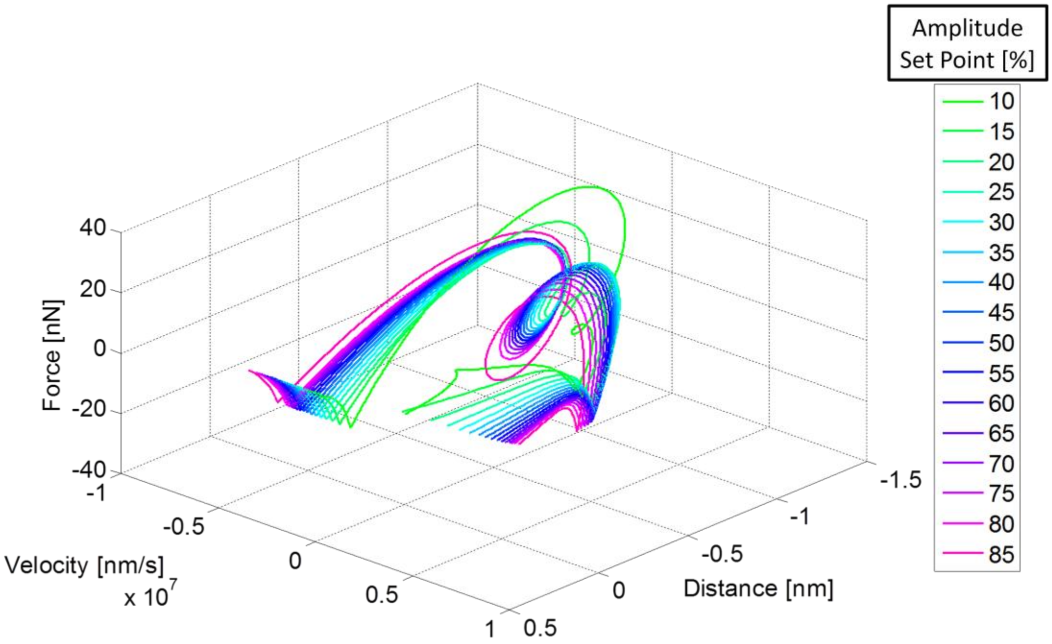

Figure 64. 4-D force curves plotted while amplitude set point [%] is varied. The different colored lines indicated different set point values.

5.3.2 Future Viscoelastic Models

A second suggested future direction of the work present in this thesis is the expansion of the rheological model used to represent the surface. The SLS can be expanded with additional Maxwell arms in what is known as the Wiechert Model [80]. With the addition of more Maxwell models, multiple discrete relaxation/retardation times will be used to represent the surface and move towards a more realistic model. In order to modify the VETICA method to incorporate these additional relaxation times, more information about the surface will need to be known beyond the three surface positions currently needed to compute the VETICA method using only one characteristic time constant.

Additionally, the use of “partial memory spring-pot” non-linear elements which use partial fraction to determine their response to applied loads/strains have been recently applied to indentation for conical and spherical tips [107]. The use of these non-linear elements could present continuous solutions characterization of viscoelastic surface in IC-AFM without the use of discrete time elements. The true challenge of material characterization then becomes balancing the resources consumed to make the extraction more physically realistic while reducing imaging times.

Appendices

A) Standard Linear Solid Configurations

The Standard Linear Solid can be represented in two configurations (Appendix Figure 1) of the three discrete mechanical elements, two springs and one dashpot. The configuration used in this thesis and displays as Appendix Figure 1A is called the Zener model. There is a mechanically equivalent model frequently referred to as the Poynting-Thomson model which contains a Voigt model in series with an elastic spring (Appendix Figure 1B).

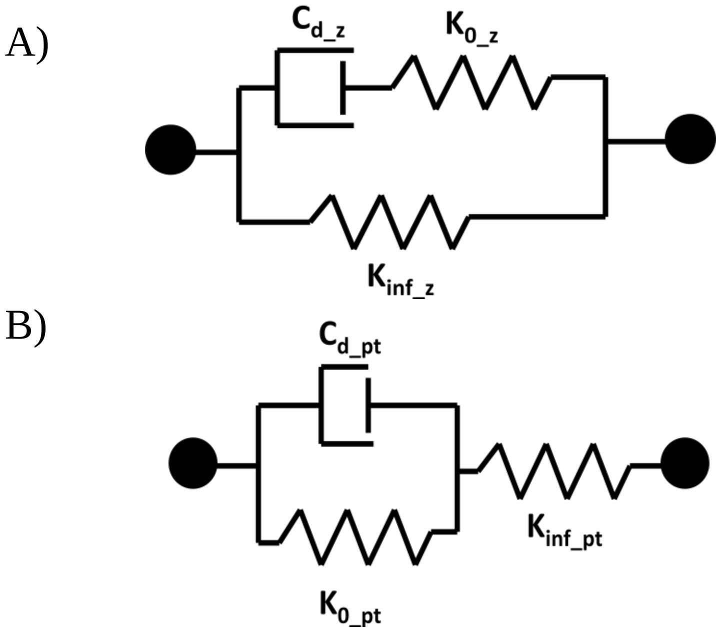

Appendix Figure 1. A) The Standard Linear Solid (SLS) configuration, sometimes referred to as the Zener model, with a Maxwell element in parallel with an elastic spring. B) The SLS configuration, sometimes referred to as the Poynting-Thomson model, with a Voigt element in series with an elastic spring. The subscripts z and pt refer to Zener and Poynting-Thomson respectively.

The following derivation details the relationship between the coefficients of the configurations. First, the constitutive equations for stress and strain (σ and ϵ) are defined for the Maxwell element and Kelvin-Voigt elements as follows:

Maxwell: $$\dot{\epsilon} = \frac{\dot{\sigma}}{k_{\text{inf}}} + \frac{\sigma}{\eta} \tag{A.1}$$

Kelvin-Voigt: $$\sigma = k_{\text{inf}}\,\epsilon + \eta\dot{\epsilon} \tag{A.2}$$

Next, the constitutive equations are defined for the Zener and Poynting-Thomson (PT) models respectively:

Zener: $$\sigma_z + \dot{\sigma}_z \frac{\eta_z}{k_{0\_\text{z}}} = k_{\text{inf\_z}}\,\epsilon_z + \dot{\epsilon}_z \eta_z \left(\frac{k_{\text{inf\_z}} + k_{0\_\text{z}}}{k_{0\_\text{z}}}\right) \tag{A.3}$$

PT: $$\sigma_{pt} + \dot{\sigma}_{pt} \frac{\eta_{pt}}{k_{\text{inf\_pt}} + k_{0\_\text{pt}}} = \frac{k_{\text{inf\_pt}}\,k_{0\_\text{pt}}}{k_{\text{inf\_pt}} + k_{0\_\text{pt}}}\epsilon_{pt} + \dot{\epsilon}_{pt}\eta_{pt}\left(\frac{k_{\text{inf\_pt}}}{k_{\text{inf\_pt}} + k_{0\_\text{pt}}}\right) \tag{A.4}$$

Next, the coefficients of the stress, stress rate, strain and strain rate are related to get the conversion equations to relate the coefficients in the two configurations:

Coefficients of σ: $$1 = 1 \tag{A.5}$$

Coefficients of $\dot{\sigma}$: $$\frac{\eta_{pt}}{k_{\text{inf\_pt}} + k_{0\_\text{pt}}} = \frac{\eta_z}{k_{0\_\text{z}}} \tag{A.6}$$

$$\eta_{pt} = \eta_z \frac{k_{\text{inf\_pt}} + k_{0\_\text{pt}}}{k_{0\_\text{z}}} \tag{A.7}$$

Coefficients of ϵ: $$\frac{k_{\text{inf\_pt}}\,k_{0\_\text{pt}}}{k_{\text{inf\_pt}} + k_{0\_\text{pt}}} = k_{\text{inf\_z}} \tag{A.8}$$

$$\boldsymbol{k_{\text{inf\_pt}}\,k_{0\_\text{pt}} = k_{\text{inf\_z}}\left(k_{\text{inf\_pt}} + k_{0\_\text{pt}}\right)} \tag{A.9}$$

Coefficients of $\dot{\epsilon}$: $$\eta_z\left(\frac{k_{\text{inf\_z}} + k_{0\_\text{z}}}{k_{0\_\text{z}}}\right) = \eta_{pt}\left(\frac{k_{\text{inf\_pt}}}{k_{\text{inf\_pt}} + k_{0\_\text{pt}}}\right) \tag{A.10}$$

Subbing in A.7: $$\eta_z\left(\frac{k_{\text{inf\_z}} + k_{0\_\text{z}}}{k_{0\_\text{z}}}\right) = \eta_z\left(\frac{k_{\text{inf\_pt}} + k_{0\_\text{pt}}}{k_{0\_\text{z}}}\right)\left(\frac{k_{\text{inf\_pt}}}{k_{\text{inf\_pt}} + k_{0\_\text{pt}}}\right) \tag{A.11}$$

Simplifying:

$$\boldsymbol{k}_{\mathbf{inf\_z}} + \boldsymbol{k}_{\mathbf{0\_z}} = \boldsymbol{k}_{\mathbf{inf\_pt}} \qquad \text{A.12}$$

$$\eta_{pt} = \eta_z \frac{k_{\mathrm{inf\_pt}}\, k_{\mathrm{0\_pt}}}{k_{\mathrm{inf\_z}}\, k_{\mathrm{0\_z}}} \qquad \text{A.13}$$

Final Relationship from A.12 and A.7:

$$\boldsymbol{\eta}_{\boldsymbol{pt}}\left(\boldsymbol{k}_{\mathbf{inf\_z}}\, \boldsymbol{k}_{\mathbf{0\_z}}\right) = \boldsymbol{\eta}_{\boldsymbol{z}}\left(\boldsymbol{k}_{\mathbf{inf\_pt}}\, \boldsymbol{k}_{\mathbf{0\_pt}}\right) \qquad \text{A.14}$$

As there are three unknown variables, $k_{inf,}$ k_0, and c_d, and three conversion equations, A.9 A.12 and A.14, the mechanical element of the two configurations can be calculated.

B) Verlet Algorithm

The Verlet algorithm [90] is used to integrate Newton's equations of motion for the paddle/tip and cantilever trajectories. The presented equations outline the basics of the algorithm and how acceleration, velocity, and positions of the point-mass system are calculated. In order to being each iteration, the acceleration of each mass is calculated by dividing the total interaction force of the system (including the tip-sample interaction force F_{ts}) by the mass:

$$\ddot{z}(t) = \frac{F[z(t), \dot{z}(t)]}{m} \qquad \text{B.1}$$

where the position of the mass (m) is denoted by z and the over dots refer to differentiation with respect to time t. The force F is a function of the position and velocity.

Next, the position and velocity for the future iteration are calculated as follows:

$$z(t + \Delta t) = 2z(t) - z(t - \Delta t) + \ddot{z}(t)\Delta t^2 \qquad \text{B.2}$$

$$\dot{z}(t + \Delta t) = \frac{z(t + \Delta t) - z(t - \Delta t)}{2\Delta t} \qquad \text{B.3}$$

where Δt is the time step of between iterations of the integration. The main benefit of the Verlet algorithm is the improved stability over the simple Euler method with little added computation costs.

C) Force Balance of SLS

The Standard Linear Solid (SLS) in the Zener configuration experiences a force balance between the right and left “arms” of the mechanical model when creep is occurring during the non-contact phase of IC-AFM. Figure 24 in Chapter three displays the configuration and internal forces of the model during creep.

The following derivation is the method by which equation (64) is formed. The surface position (*X*) is updated by a change in surface position (*ΔX*) after a time step (*Δt*) while creep is occurring.

Force Balance equation:

$$k_{inf}X = -k_0(X - X_d) \tag{C.1}$$

Next replace *X* and X_d with:

$$X = X_{pr} + \mathit{\Delta}X \tag{C.2}$$

$$X_d = X_{d\,pr} + \dot{X}_d\Delta t \tag{C.3}$$

where pr denotes the previous time step value of the coordinate from the SLS. Subbing C.2 and C.3 into C.1 yields:

$$k_{inf}\left(X_{pr} + \mathit{\Delta}X\right) = -k_0\left(X_{pr} + \mathit{\Delta}X - X_{d\,pr} - \dot{X}_d\Delta t\right) \tag{C.4}$$

Rearranging and getting $\mathit{\Delta}X$ to the left side:

$$k_{inf}X_{pr} + k_{inf}\mathit{\Delta}X = -k_0X_{pr} - k_0\mathit{\Delta}X + k_0X_{d\,pr} + k_0\dot{X}_d\Delta t \tag{C.5}$$

$$\Delta X(k_{inf} + k_0) = -X_{pr}(k_{inf} + k_0) + k_0X_{d\,pr} + k_0\,\dot{X}_d * \Delta t \tag{C.6}$$

$$\Delta X = -X_{pr} + \frac{k_0}{\left(k_{inf} + k_0\right)}(X_{d\,pr} + \dot{X}_d * \Delta t) \tag{C.7}$$

Now using C.7 and the definition of X from C.2 the updated X position used in equation (64) can be expressed as:

$$X = X_{pr} + \Delta X$$

$$= X_{pr} - X_{pr} + \frac{k_0}{\left(k_{inf} + k_0\right)} \left(X_{d\,pr} + \dot{X}_d * \Delta t\right) \qquad \text{C.8}$$

$$\boldsymbol{X} = \frac{\boldsymbol{k_0}}{\left(\boldsymbol{k_{inf}} + \boldsymbol{k_0}\right)} \left(\boldsymbol{X_{d\,pr}} + \dot{\boldsymbol{X}}_{\boldsymbol{d}} * \Delta \boldsymbol{t}\right) \qquad \text{C.9}$$

Bibliography

[1] Binnig, G., Quate, C., and Gerber, C., 1986, "Atomic Force Microscope," Physical Review Letters, 56(9), pp. 930-933.

[2] Martin, Y., Williams, C. C., and Wickramasinghe, H. K., 1987, "Atomic force microscope-force mapping and profiling on a sub 100-A scale," *Journal of Applied Physics*, pp. 4723-4729.

[3] Zhong, Q., Innis, D., Kjoller, K., and Elings, V. B., 1993, "Fractured polymer silica fiber studied by tapping mode atomic-force microscopy," Surface Science(290), pp. L688 - L692.

[4] Maivald, P., Butt, H. J., Gould, S. A. C., Prater, C. B., Drake, B., Gurley, J. A., Elings, V. B., and Hansma, P. K., 1991, "Using force modulation to image surfave elasticites with the atomic force microscope," (2), pp. 103-106.

[5] Albrecht, T. R., Grutter, P., Horne, H. K., and Rugar, D., 1990, "Frequency modulation detection using high-Q cantilevers for enhanced force microscope sensitivity," Journal of Applied Physics, 69, pp. 668-673.

[6] Pletikapic, G., Berquand, A., Radic, T. M., and Svetlicic, V., 2012, "Quantitative Nanomechanical Mapping Of Marine Diatom In Seawater Using Peak Force Tapping Atomic Force Microscopy," Journal of Phycology, 48(1), pp. 174-185.

[7] Young, T. J., Monclus, M. a., Burnett, T. L., Broughton, W. R., Ogin, S. L., and Smith, P. a., 2011, "The use of the PeakForce TM quantitative nanomechanical mapping AFM-based method for high-resolution Young's modulus measurement of polymers," Measurement Science and Technology, 22(12), pp. 125703-125703.

[8] Tamayo, J., and Garcı, R., 1996, "Deformation , Contact Time , and Phase Contrast in Tapping Mode Scanning Force Microscopy," 7463(13), pp. 4430-4435.

[9] Cleveland, J. P., Anczykowski, B., Schmid, a. E., and Elings, V. B., 1998, "Energy dissipation in tapping-mode atomic force microscopy," Applied Physics Letters, 72(20), pp. 2613-2613.

[10] Putman, C. A. J., Vanderwerf, K. O., Degrooth, B. G., Vanhulst, N. F., and Greve, J., 1994, "Tapping Mode Atomic-Force Microscopy In Liquid," Applied Physics Letters, 64(18), pp. 2454-2456.

[11] Putman, C. A. J., Vanderwerf, K. O., Degrooth, B. G., Vanhulst, N. F., and Greve, J., 1994, "Viscoelasticity Of Living Cells Allows High-Resolution Imaging By Tapping Mode Atomic-Force Microscopy," Biophysical Journal, 67(4), pp. 1749-1753.

[12] Scott, W. W., and Bhushan, B., 2003, "Use of phase imaging in atomic force microscopy for measurement of viscoelastic contrast in polymer nanocomposites and molecularly thick lubricant films," Ultramicroscopy, 97(1-4), pp. 151-169.

[13] Wang, D., Fujinami, S., Nakajima, K., and Nishi, T., 2010, "True Surface Topography and Nanomechanical Mapping Measurements on Block Copolymers with Atomic Force Microscopy," Macromolecules, 43(7), pp. 3169-3172.

[14] Sauer, B. B., McLean, R. S., and Thomas, R. R., 1998, "Tapping Mode AFM Studies of Nano-Phases on Fluorine-Containing Polyester Coatings and Octadecyltrichlorosilane Monolayers," Langmuir, 14(11), pp. 3045-3051.

[15] Krzeminski, M., Molinari, M., Troyon, M., and Coqueret, X., 2010, "Characterization by Atomic Force Microscopy of the Nanoheterogeneities Produced by the Radiation-Induced Cross-Linking Polymerization of Aromatic Diacrylates," Macromolecules, 43(19), pp. 8121-8127.

[16] Tamayo, J., and García, R., 1997, "Effects of elastic and inelastic interactions on phase contrast images in tapping-mode scanning force microscopy," Applied Physics Letters, 71(16), pp. 2394-2394.

[17] Lin, S. M., 2007, "Energy dissipation and dynamic response of an amplitude-modulation atomic-force microscopy subjected to a tip-sample viscous force," Ultramicroscopy, 107(2-3), pp. 245-253.
[18] Lin, S. M., 2006, "Energy dissipation and frequency shift of a damped dynamic force microscopy," Ultramicroscopy, 106(6), pp. 516-524.
[19] Xu, W., Woodadams, P., and Robertson, C., 2006, "Measuring local viscoelastic properties of complex materials with tapping mode atomic force microscopy," Polymer, 47(13), pp. 4798-4810.
[20] García, R., 2002, "Dynamic atomic force microscopy methods," Surface Science Reports, 47(6-8), pp. 197-301.
[21] Sheiko, S. S., 2000, "Imaging of polymers using scanning force microscopy: From superstructures to individual molecules," New Developments in Polymer Analytics Ii, 151, pp. 61-174.
[22] Raghavan, D., VanLandingham, M., Gu, X., and Nguyen, T., 2000, "Characterization of heterogeneous regions in polymer systems using tapping mode and force mode atomic force microscopy," Langmuir, 16(24), pp. 9448-9459.
[23] Attard, P., 2007, "Measurement and interpretation of elastic and viscoelastic properties with the atomic force microscope," 473201.
[24] Friedenberg, M. C., and Mate, C. M., 1996, "Dynamic viscoelastic properties of liquid polymer films studied by atomic force microscopy," Langmuir, 12(25), pp. 6138-6142.
[25] Stark, R. W., Schitter, G., and Stemmer, A., 2003, "Tuning the interaction forces in tapping mode atomic force microscopy," Physical Review B, 68(8).
[26] Braithwaite, G. J. C., and Luckham, P. F., 1999, "The simultaneous determination of the forces and viscoelastic properties of adsorbed polymer layers," Journal of Colloid and Interface Science, 218(1), pp. 97-111.
[27] Braithwaite, G. J. C., Luckham, P. F., and Howe, A. M., 1999, "Study of a solvated adsorbed gelatin layer using a modified force microscope," Journal of Colloid and Interface Science, 213(2), pp. 525-545.
[28] San Paulo, Á., and García, R., 2001, "Tip-surface forces, amplitude, and energy dissipation in amplitude-modulation (tapping mode) force microscopy," Physical Review B, 64(19), pp. 1-4.
[29] San Paulo, Á., and García, R., 2002, "Unifying theory of tapping-mode atomic-force microscopy," Physical Review B, 66(4), pp. 2-5.
[30] Sahin, O., Magonov, S., Su, C., Quate, C. F., and Solgaard, O., 2007, "An atomic force microscope tip designed to measure time-varying nanomechanical forces," Nature nanotechnology, 2(8), pp. 507-514.
[31] Stark, M., Stark, R. W., Heckl, W. M., Guckenberger, R., Hecklt, W. M., and Guckenberger, R., "Inverting Dynamic Force Microscopy: From Signals to Time-Resolved Interaction Forces," Proc. Proceedings of the National Academy of Sciences of the United States of America, pp. 8473-8478.
[32] Giessibl, F. J., 1995, "Atomic-Resolution Of The Silicon (111)-(7x7) Surface By Atomic-Force Microscopy," Science, 267(5194), pp. 68-71.
[33] Sahin, O., and Erina, N., 2008, "High-resolution and large dynamic range nanomechanical mapping in tapping-mode atomic force microscopy," Nanotechnology, 19(44), pp. 445717-445717.
[34] Hembacher, S., Giessibl, F. J., and Mannhart, J., 2004, "Force microscopy with light-atom probes," Science, 305(5682), pp. 380-383.
[35] Giessibl, F. J., 2003, "Advances in atomic force microscopy," Reviews of Modern Physics, 75(3), pp. 949-983.

[36] Derjaguin, B. V., Muller, V. M., and Toporov, Y. P., 1975, "Effect Of Contact Deformations On Adhesion Of Particles," Journal of Colloid and Interface Science, 53(2), pp. 314-326.

[37] Johnson, K. T., Kendall, K., and Roberts, A. D., "Surface Energy and the Contact of Elastic Solids," Proc. Proceedings of the Royal Society of London Series A, Mathematical and Physical Sciences, pp. 301-313.

[38] Unertl, W. N., 1999, "Implications of contact mechanics models for mechanical properties measurements using scanning force microscopy," Journal of Vacuum Science & Technology A, 17(4), pp. 1779-1786.

[39] Attard, P., and Parker, J., 1992, "Deformation and adhesion of elastic bodies in contact," Physical review. A, 46(12), pp. 7959-7971.

[40] Cleveland, J. P., Anczykowski, B., Schmid, A. E., and and Elings, V. B., 1998, "Energy dissipation in tapping-mode atomic force microscopy," 72(20), pp. 2613 - 2615.

[41] Zwörner, O., Hölscher, H., Schwarz, U. D., and Wiesendanger, R., 1998, "The velocity dependence of frictional forces in point-contact friction," Applied Physics A: Materials Science & Processing, 66(7), pp. S263-S267.

[42] Mate, C., McClelland, G., Erlandsson, R., and Chiang, S., 1987, "Atomic-Scale Friction of a Tungsten Tip on a Graphite Surface," Physical Review Letters, 59(17), pp. 1942-1945.

[43] Radmacher, M., 1993, "Imaging viscoelasticity by force modulation with the atomic force microscope," Biophysical Journal, 64(3), pp. 735-742.

[44] Rosa-Zeiser, A., Weilandt, E., Hild, S., and Marti, O., "The simultaneous measurement of elastic, electrostatic and adhesive properties by scanning force microscopy: pulsed-force mode operation," Measurement Science and Technology(8), pp. 1333-1338.

[45] Pittenger, B., Erina, N., and Su, C., 2010, "Quantitative Mechanical Property Mapping at the Nanoscale with PeakForce QNM," pp. 1-12.

[46] Hurley, D., Shen, K., Jennett, N., and Turner, J., 2003, "Atomic force acoustic microscopy methods to determine thin-film elastic properties," Journal of Applied Physics, 94(4), pp. 2347-2354.

[47] Rabe, U., Amelio, S., Kopycinska, M., Hirsekorn, S., Kempf, M., Goken, M., and Arnold, W., 2002, "Imaging and measurement of local mechanical material properties by atomic force acoustic microscopy," Surface and Interface Analysis, 33(2), pp. 65-70.

[48] Yuya, P. A., Hurley, D. C., and Turner, J. A., 2008, "Contact-resonance atomic force microscopy for viscoelasticity," (104), p. 074916.

[49] Yuya, P., Hurley, D., and Turner, J., 2011, "Relationship between Q-factor and sample damping for contact resonance atomic force microscope measurement of viscoelastic properties," 109(11), p. 113528.

[50] Yuya, P. a., Hurley, D. C., and Turner, J. a., 2008, "Contact-resonance atomic force microscopy for viscoelasticity," Journal of Applied Physics, 104(7), pp. 074916-074916.

[51] J.S., F., Lai, J. S., and Onaran, K., 1976, Creep and Relaxation of Nonlinear Viscoelastic Materials—with an Introduction to Linear Viscoelasticity, North-Holland Publishing Company, Amsterdam.

[52] Jalili, N., and Laxminarayana, K., 2004, "A review of atomic force microscopy imaging systems: application to molecular metrology and biological sciences," Mechatronics, 14(8), pp. 907-945.

[53] Schirmeisen, A., Hölscher, H., Anczykowski, B., Weiner, D., Schäfer, M. M., and Fuchs, H., 2005, "Dynamic force spectroscopy using the constant-excitation and constant-amplitude modes," Nanotechnology, 16(3), pp. S13-S17.

[54] Gotsmann, B., and Fuchs, H., 2002, "Dynamic AFM using the FM technique with constant excitation amplitude," Applied Surface Science, 188(3-4), pp. 355-362.

[55] Giessibl, F. J., 1997, "Forces and frequency shifts in atomic-resolution dynamic-force microscopy," Physical Review B, 56(24), pp. 16010-16015.

[56] Durig, U., 2000, "Interaction sensing in dynamic force microscopy," New Journal of Physics, 2, pp. 51-512.
[57] Durig, U., 1999, "Relations between interaction force and frequency shift in large-amplitude dynamic force microscopy," Applied Physics Letters, 75(3), pp. 433-435.
[58] Holscher, H., Langkat, S. M., Schwarz, A., and Wiesendanger, R., 2002, "Measurement of three-dimensional force fields with atomic resolution using dynamic force spectroscopy," Applied Physics Letters, 81(23), pp. 4428-4430.
[59] Albers, B. J., Schwendemann, T. C., Baykara, M. Z., Pilet, N., Liebmann, M., Altman, E. I., and Schwarz, U. D., 2009, "Three-dimensional imaging of short-range chemical forces with picometre resolution," Nature Nanotechnology, 4(5), pp. 307-310.
[60] Sader, J. E., and Jarvis, S. P., 2004, "Accurate formulas for interaction force and energy in frequency modulation force spectroscopy," Applied Physics Letters, 84(10), pp. 1801-1803.
[61] Sader, J. E., and Jarvis, S. P., 2004, "Interpretation of frequency modulation atomic force microscopy in terms of fractional calculus," Physical Review B, 70(1), p. 3.
[62] Sader, J. E., Uchihashi, T., Higgins, M. J., Farrell, A., Nakayama, Y., and Jarvis, S. P., 2005, "Quantitative force measurements using frequency modulation atomic force microscopy - theoretical foundations," Nanotechnology, 16(3), pp. S94-S101.
[63] Sader, J. E., and Jarvis, S. P., 2006, "Coupling of conservative and dissipative forces in frequency-modulation atomic force microscopy," Physical Review B, 74(19).
[64] O'Shea, S. J., and Welland, M. E., 1998, "Atomic force microscopy at solid-liquid interfaces," Langmuir, 14(15), pp. 4186-4197.
[65] Holscher, H., 2006, "Quantitative measurement of tip-sample interactions in amplitude modulation atomic force microscopy," Applied Physics Letters, 89(12).
[66] Lee, M. H., and Jhe, W. H., 2006, "General theory of amplitude-modulation atomic force microscopy," Physical Review Letters, 97(3).
[67] Hu, S., and Raman, A., 2008, "Inverting amplitude and phase to reconstruct tip-sample interaction forces in tapping mode atomic force microscopy," Nanotechnology, 19(37).
[68] Katan, A. J., van Es, M. H., and Oosterkamp, T. H., 2009, "Quantitative force versus distance measurements in amplitude modulation AFM: a novel force inversion technique," Nanotechnology, 20(16), p. 9.
[69] Stark, R., Schitter, G., Stark, M., Guckenberger, R., and Stemmer, A., 2004, "State-space model of freely vibrating and surface-coupled cantilever dynamics in atomic force microscopy," Physical Review B, 69(8), pp. 1-9.
[70] Yagasaki, K., 2004, "Nonlinear dynamics of vibrating microcantilevers in tapping-mode atomic force microscopy," Physical Review B, 70(24).
[71] Anczykowski, B., Kruger, D., and Fuchs, H., 1996, "Cantilever dynamics in quasinoncontact force microscopy: Spectroscopic aspects," Physical Review B, 53(23), pp. 15485-15488.
[72] Hölscher, H., Gotsmann, B., Allers, W., Schwarz, U., Fuchs, H., and Wiesendanger, R., 2001, "Measurement of conservative and dissipative tip-sample interaction forces with a dynamic force microscope using the frequency modulation technique," Physical Review B, 64(7), pp. 1-6.
[73] Rodriguez, T., and Garcia, R., 2002, "Tip motion in amplitude modulation (tapping-mode) atomic-force microscopy: Comparison between continuous and point-mass models," Applied Physics Letters, 80(9), pp. 1646-1648.
[74] Sahin, O., 2007, "Harnessing bifurcations in tapping-mode atomic force microscopy to calibrate time-varying tip-sample force measurements," The Review of scientific instruments, 78(10), pp. 103707-103707.

[75] Solares, S. D., and Hölscher, H., 2010, "Numerical analysis of dynamic force spectroscopy using a dual-oscillator sensor," Journal of Vacuum Science & Technology B: Microelectronics and Nanometer Structures, 28(3), pp. C4E1-C4E1.

[76] Solares, S. D., and Hölscher, H., 2010, "Numerical analysis of dynamic force spectroscopy using the torsional harmonic cantilever," Nanotechnology, 21(7), pp. 75702-75702.

[77] Solares, S. D., and Chawla, G., 2008, "Dual frequency modulation with two cantilevers in series: a possible means to rapidly acquire tip-sample interaction force curves with dynamic AFM," Measurement Science & Technology, 19(5).

[78] Bajak, A., 2009, "New DNA hybridization detection technology removes reliance on fluorescence," BioTechniques.

[79] Aklonis, J. J., W.J., M., and Shen, M., 1972, Introduction to Polymer Viscoelasticity, Wiley-Interscience, New York.

[80] Roylance, D., 2001, "Engineering Viscoelasticity," pp. 1-37.

[81] Killgore, J. P., Yablon, D. G., Tsou, A. H., Gannepalli, A., Yuya, P. A., Turner, J. A., Proksch, R., and Hurley, D. C., 2011, "Viscoelastic Property Mapping with Contact Resonance Force Microscopy," Langmuir, 27(23), pp. 13983-13987.

[82] Ferry, J. D., 1980, Viscoelastic Properties of Polymers, Wiley & Sons, New York.

[83] Lee, E. H., and Radok, J. R. M., 1960, "The contact problem for viscoelastic bodies," ASME, 30, pp. 438-444.

[84] Ting, T. C. T., 1966, "The contact stresses between a rigid indenter and a viscoelastic half-space," Journal of Applied Mechanics, 33, pp. 845-854.

[85] Cheng, L., Xia, X., Yu, W., Scriven, L. E., and Gerberich, W. W., 2000, "Flat-Punch Indentation of Viscoelastic Material," Polymer, 38(August 1999), pp. 10-22.

[86] Cheng, L., 2005, "Spherical-tip indentation of viscoelastic material," Mechanics of Materials, 37(1), pp. 213-226.

[87] Attard, P., 2000, "Interaction and Deformation of Elastic Bodies: Origin of Adhesion Hysteresis," Society, pp. 10635-10641.

[88] Attard, P., 2001, "Interaction and Deformation of Viscoelastic Particles . 2 . Adhesive Particles," English(20), pp. 4322-4328.

[89] Attard, P., 2001, "Interaction and deformation of viscoelastic particles: Nonadhesive particles," Physical Review E, 63(6), pp. 1-9.

[90] Verlet, L., 1967, "Computer Experiments On Classical Fluids .I. Thermodynamical Properties Of Lennard-Jones Molecules," Physical Review, 159(1), pp. 98-&.

[91] Nise, N., 2009, Control Systems Engineering, John Wiley & Sons.

[92] Balachandran, B., and Magrab, E. B., 2008, Vibrations, CL Engineering.

[93] Coleman, T. F., and Li, Y. Y., 1996, "An interior trust region approach for nonlinear minimization subject to bounds," Siam Journal on Optimization, 6(2), pp. 418-445.

[94] Thomas, F. C., and Li, Y. Y., 1994, "On The Convergence Of Interior-Reflective Newton Methods For Nonlinear Minimization Subject To Bounds," Mathematical Programming, 67(2), pp. 189-224.

[95] Wright, C. A., and Solares, S. D., 2011, "On Mapping Subangstrom Electron Clouds with Force Microscopy," Nano Letters, 11(11), pp. 5026-5033.

[96] Vanlandingham, M. R., Villarrubia, J. S., Guthrie, W. F., Meyers, G. F., Dow, T., Company, C., Chemical, A., National, S., and Gmbh, W.-v. V., "Nanoindentation Of Polymers : An Overview by Nanoindentation of Polymers : An Overview," Technology(August 2000), pp. 15-43.

[97] VanLandingham, M. R., Chang, N. K., Drzal, P. L., White, C. C., and Chang, S. H., 2005, "Viscoelastic characterization of polymers using instrumented indentation. I. Quasi-static testing," Journal of Polymer Science Part B: Polymer Physics, 43(14), pp. 1794-1811.

[98] Monclus, M. A., and Jennett, N. M., 2011, "In search of validated measurements of the properties of viscoelastic materials by indentation with sharp indenters," Philosophical Magazine, 91(7-9), pp. 1308-1328.

[99] Jandt, K., 2001, "Atomic force microscopy of biomaterials surfaces and interfaces," Surface Science, 491(3), pp. 303-332.

[100] VanLandingham, M. R., Chang, N. K., Drzal, P. L., White, C. C., and Chang, S. H., 2005, "Viscoelastic characterization of polymers using instrumented indentation. I. Quasi-static testing," Journal of Polymer Science Part B-Polymer Physics, 43(14), pp. 1794-1811.

[101] Mahaffy, R. E., Park, S., Gerde, E., Käs, J., and Shih, C. K., 2004, "Quantitative analysis of the viscoelastic properties of thin regions of fibroblasts using atomic force microscopy," Biophysical journal, 86(3), pp. 1777-1793.

[102] Haga, H., Nagayama, M., Kawabata, K., Ito, E., Ushiki, T., and Sambongi, T., 2000, "Time-lapse viscoelastic imaging of living fibroblasts using force modulation mode in AFM," Journal of electron microscopy, 49(3), pp. 473-481.

[103] Proksch, R., and Kalinin, S. V., 2010, "Energy dissipation measurements in frequency-modulated scanning probe microscopy," Nanotechnology, 21(45), pp. 455705-455705.

[104] Lekka, M., Gil, D., Pogoda, K., Dulinska-Litewka, J., Jach, R., Gostek, J., Klymenko, O., Prauzner-Bechcicki, S., Stachura, Z., Wiltowska-Zuber, J., Okon, K., and Laidler, P., 2012, "Cancer cell detection in tissue sections using AFM," Archives of Biochemistry and Biophysics, 518(2), pp. 151-156.

[105] Watanabe, T., Kuramochi, H., Takahashi, A., Imai, K., Katsuta, N., Nakayama, T., Fujiki, H., and Suganuma, M., 2012, "Higher cell stiffness indicating lower metastatic potential in B16 melanoma cell variants and in (-)-epigallocatechin gallate-treated cells," Journal of Cancer Research and Clinical Oncology, 138(5), pp. 859-866.

[106] Kammler, D. W., 2008, A First Course in Fourier Analysis, Cambridge University Press.

[107] Shahsavari, R., and Ulm, F.-j., 2009, "Mechanics of Materials and Structures Indentation Analysis Of Fractional Viscoelastic," Materials and Structures, 4(March).